Spin squeezing and entanglement with room temperature atoms for quantum sensing and communication

Heng Shen

Niels Bohr Institute, University of Copenhagen

Academic supervisor:
Prof. Eugene S. Polzik

This dissertation is submitted for the degree of

Doctor of Philosophy

December 2014

Summary

In this thesis, different experiments on spin squeezing and entanglement involving room temperature ensembles of Cesium atoms are described. The key method is the off-resonant Faraday interaction of spin-polarized atomic ensemble with a light field.

Quantum backaction evading measurement of one quadrature of collective spin components by stroboscopically modulating the intensity of probe beam at twice Larmor frequency is used to generate the spin-squeezed state. A spin-squeezed state conditioned on the light-polarization measurement with 2.2 ± 0.3dB noise reduction below the spin projection noise limit for the measured quadrature has been observed.

In the radio-frequency atomic magnetometry, a transverse rf magnetic field resonant with the atomic Larmor frequency causes the polarized spin ensemble to precess and the angle of precession is proportional to the rf magnetic field, which is measured with a weak off-resonant linearly polarized probe beam. A projection noise limited optical magnetometer at room temperature with an rf magnetic-field sensitivity of $158 \pm 1\text{fT}/\sqrt{\text{Hz}}$ and 2D spatial resolution of 300μm is reported. Furthermore, using spin-squeezing of atomic ensemble, the sensitivity of magnetometer is improved.

Deterministic continuous variable teleportation between two distant atomic ensembles is demonstrated, where the light-atom entanglement establishes the non-local channel to teleport the spin information from one ensemble to the other. The fidelity of teleportating dynamically changing sequence of spin states surpasses a classical benchmark, demonstrating the true quantum teleportation.

Resumé

Denne afhandling beskriver adskillige eksperimenter med spin-sammenpresning ("squeezing") og sammenfiltring, som benytter ensembler af cæsiumatomer ved stuetemperatur. Afgørende til forsøgene er den Faraday vekselvirkning mellem spin-polariseret atomer og lys. Hovedrollen bliver spillet af mikrofremstillet glasbeholdere af atomer på gasform, koblet til en optisk kavitet.

For at skabe et spin-sammenpresset tilstand måles der en kvadratur af den kollektive spin-komponent $\hat{J}_z$ på sådan et måde, at den såkaldte kvante "back-action" omgås. Teknikken er at modulere probe-lysets intensitet stroboskopisk, på en frekvens to gang så større som Larmor-frekvensen. Støjen af det spin-sammenpresset tilstand ligger 2.2 ± 0.3dB under grænsen for spin-projektionsstøjen.

I radiofrekvens atom-optisk magnetometri, et tværsgående rf magnetisk felt påresonans med atomernes Larmor-frekvens gøre den polariseret spin-ensembel til at præcessere. Præcessionsvinklen er proportional med magnetfeltet, der bliver målt med brug af svag lineært-polariseret probe-lys. Der presenteres en projektionsstøjsbegrænset optisk magnetometer ved stuetemperatur med sensitivitet $158 \pm 1\text{fT}/\sqrt{\text{Hz}}$ og rumlig resolution 300μm. Sensitiviteten forbedres endnu mere med hjælp af spin-sammenpresningen.

Der vises også deterministisk kontinuerlig-variabel teleportation mellem to atomare ensembler på stor afstand. I denne sammenhæng sammenfiltring mellem lys og atomer etablerer en ikke-lokal kanal til at teleportere spin-information fra den ene ensembel til den anden. Fideliteten af at teleportere spin-tilstande, som ændrer sig på en dynamisk måde, overgår det klassiske benchmark. Derfor er der tale om den ægte kvante-teleportation.

Abstract

In this thesis, different experiments on spin squeezing and entanglement involving room temperature ensembles of Cesium atoms are described. The key method is the off-resonant Faraday interaction of spin-polarized atomic ensemble with a light field. And the key component is the micro-fabricated vapor cell coupled into an optical cavity. Quantum backaction evading measurement of one quadrature of collective spin components by stroboscopically modulating the intensity of probe beam at twice Larmor frequency is used to generate the spin-squeezed state. A projection noise limited optical magnetometer at room temperature is reported. Furthermore, using spin-squeezing of atomic ensemble, the sensitivity of magnetometer is improved. Deterministic continuous variable teleportation between two distant atomic ensembles is demonstrated. The fidelity of teleportating dynamically changing sequence of spin states surpasses a classical benchmark, demonstrating the true quantum teleportation.

Preface

The work presented in this dissertation is a summary of research carried out between Sep 2011 and Jan 2015 as a PhD candidate in the Danish National Research Foundation Center for Quantum Optics (QUANTOP group) led by professor Eugene Polzik at the Niels Bohr Institute, University of Copenhagen. In the beginning of my PhD study, I had the pleasure of working on the project of quantum teleportation between two atomic ensembles in the marcocells with Hanna Krauter, Daniel Salart and Jonas Meyer Petersen when I learnt the daily routines in the lab from them. In the following three years, the focus has shifted from the experimental research on the macrocell to the fundamental investigation towards application on the micro-fabricated vapor cells, and Eugene gave me this good opportunity to be the first PhD student working on this project, which is the main part of this thesis.

I am grateful to Prof. Eugene Polzik for giving me the opportunity to work in QUANTOP on this completely new project. Although time flies fast, I still remember the first time I had a skype conversation with him through the unstable Internet, and several times fruitful discussion with him during my first visit in Denmark. He really taught me a lot not only in physics but also in the attitude to the life, which helped me smoothly transit from an optical experimentalist to a beginner on the atomic physics, and from the Chinese eduction mode to the European one. Without Eugene's enthusiasm and physical intuition, I would have no chance to present the results here.

I thank Giorgos Vasilakis very much for closely working with me more than two years. We had countless interesting conversations, both about physics and philosophical topics. He is not only a very good colleague in the lab but also a nice friend in the daily life. I enjoyed the good time with his big family, especially with Penelope.

I would like to thank Hanna Krauter and Jonas Meyer Petersen who gave me lots of help to start my study in the lab and the life abroad. Although the overlapping with Hanna was very short, she was trying her best to give me supports. I thank Daniel Salart for his support on the experiment, and we have had a very good collaboration for three years. I also want to thank Misha Balabas for the good times when developing the microcells together. The visiting PhD student Bing Chen is a good collaborator who made an enthusiastic con-

tribution to the experiment, and is also one of my close friends keeping talking with me in Chinese. During my time at QUANTOP I have also had the opportunity to work with other "Cellmates" including Kasper Jensen, Anne Fabricant, Michael Zugenmaier, and Rodrigo Thomas. I would also like to acknowledge the members of QUANTOP group for a friendly atmosphere during the years.

I also thank my big Chinese group including Pengfei, Haoran, Junjie, Yang, Guannan, Hairun, Haiyan, Tian, Qian, Ming and others for your warm company and support.

Last but not least I would like to thank my current and future family members. My dead grandfather, Doctor Shen, gave me a nice education on the art and sociology which deeply impressed me. My parents, Doctor Shen and Doctor Guo, took care of me so long time and gave me the opportunity to reach different taste of food and cultures.

List of Publications

1. H. Krauter, D. Salart, C. A. Muschik, J. M. Petersen, Heng Shen, T. Fernholz, and E. S. Polzik, Deterministic quantum teleportation between distant atomic objects, *Nature Physics* 9, 400 (2013).

2. G. Vasilakis, H. Shen[1], K. Jensen, M. Balabas, D. Salart, B. Chen, E. S. Polzik, Generation of a squeezed state of an oscillator by stroboscopic back-action-evading measurement, arXiv:1411.6289, 2014(submitted to Nature Physics).

3. H. Shen, G. Vasilakis, K. Jensen, M. Balabas, D. Salart, A. Fabricant, B. Chen, E. S. Polzik, Quantum noise limited cavity-enhanced radio-frequency atomic magnetometer, to be submitted.

[1] G. Vasilakis, H. Shen contribute equally to this work.

Table of contents

Chapter 1

Introduation

1.1 Quantum information processing

Since quantum teleportation was proposed by Bennett *et. al.* in 1993[1], theoretical and experimental researches on quantum information have developed rapidly. As one application of quantum entanglement in the communication, quantum dense coding, which is a way to transmit two bits of information through the manipulation of only one of two entangled quantum systems[2], has been experimentally demonstrated in both discrete and continuous quantum variable regimes[3, 4]. Furthermore, absolutely secure transmission of secret messages and the faithful transfer of unknown quantum states is promised by quantum communication. However, due to losses and decoherence in the channel, the communication fidelity decreases exponentially with the channel length which makes the long-distance quantum communication difficult to be built realistically. In order to solve this problem, theorists suggested to use atomic ensembles and linear optics components as quantum repeaters to improve the communication fidelity[5].

As another important application of quantum technology, quantum computer (QC) admitting quantum superposition and entanglement attracts more and more attention and is treated as a milestone of modern science due to its promise of high-speed and powerful computation capacities over the classical computer. So far, many exciting theoretical and experimental tasks have been accomplished in both the discrete variable (DV) and continuous variable (CV)[6, 7, 8], such as Shor's quantum factoring algorithm[9], which reduces running time from exponential to polynomial time with respect to the classical factorization algorithm. Besides quantum logic gates, quantum memory is also indispensable to a genuine quantum computer due to its synchronization function that ensures operations could be timed appropriately. In the CV regime, storing photonic information in the atomic ensembles, especially for the nonclassical CV of light, primarily relies on two different methods:

one based on electromagnetically induced transparency (EIT)[10] and the other utilizing the off-resonant Faraday interaction between light and atoms [11].

1.2 Quantum Metrology

Quantum metrology is the use of quantum techniques such as entanglement to make high-resolution and highly sensitive measurements of physical parameters, and to yield higher statistical precision than purely classical approaches. Recently, squeezed vacuum states of light has been used to improve the sensitivity of a gravitational-wave observatory in GEO200 project[12]. It has been suggested that spin-squeezed states of atomic ensembles can be prepared for the improvement of sensitivity in atomic spectroscopy, interferometry and atomic clocks[13, 14, 15, 16]. Several schemes have been proposed to generate the spin-squeezed states, including the direct interaction of spins[17], electron-nucleus entanglement[18], mapping of squeezed light onto atoms[19], multiple passes of light through atoms[20] and a projective Faraday interaction based on quantum non-demolition measurement (QND)[21, 22]. Entangled states of atoms can also be used in metrology such as in atomic clocks where the projection noise of atoms limits the accuracy of the clock. Such an entanglement-assisted atomic clock was demonstrated recently in our group[22]. In addition, quantum teleportation allows for performing quantum sensing at a remote location, spatially separated from the location of the object.

1.3 Integrated quantum devices

Many quantum physical experiments have performed with bulk optics. However, complex quantum optical schemes, realized in bulk optics, suffer from severe drawbacks, as far as stability, and physical size are concerned. Therefore, people start to seek for a much more compact and stable system which is promising in the real application, such as computer CPU and other integrated functional chips. For quantum photonics, the channel can be built in the form of optical waveguide devices by using the ultrafast laser writing and other nano fabrication technologies. Shor's algorithm has been realized on an integrated waveguide silica-on-silicon chip[23]. On the other hand, the single photon source can also be integrated in the semiconductor chip, for example, solid-state QED where the quantum dot is strongly coupled in the high Q optical cavity created by the photonic crystal with a defect[24]. Additionally, in order to form the all-optical quantum communication and linear-optics quantum computing, not only single-photon sources and passive optical circuits, but also photon detectors are required. At present, researchers are trying to build photon detectors on the

chip using nano-fabrication technology based on III-V semiconductors[25]. Atomic ensembles as a good candidate for many quantum protocols such as quantum repeater and quantum memory, are also suitable to be integrated on the chip as active elements based on light-matter interaction. This type of quantum device can be made very compact in the application. For example an integrated sensor package incorporating a VCSEL laser, an alkali-vapour cell, optics, and a detector has been constructed[26]. And Bose-Einstein Condensation on an atom chip where cold atoms are magnetically trapped and guided using the magnetic field produced by conductors on the surface is another topic with lots of application such as atom interferometer and magnetometry on a chip[27].

1.4 Outline

This thesis is divided in three parts: the theoretical background containing Chapters 2, the experimental methods with Chapters 3 and finally the description of the experiments on generation and application of spin squeezed state and entanglement in Chapters 4, 5 and 6.

To be specific, Chapter 2 gives a the details of a previously established theoretical approach of light atom interface including the canonical description of atoms and light, interaction hamiltonian between light and atoms, especially the off-resonant Faraday interaction, input-output relations and the concept of thermal motion averaging and establishment of entanglement between light and atoms, whose understanding is essential for the discussed experiments.

In Chapter 3 the details of the experimental system are explained, including characteristic measures of atoms and light. Most importantly, the microcell as the key element of this thesis is firstly shown in our work, including the fabrication and characterization. Optical cavity and the quantum noise properties of the atomic and light system are then discussed.

Chapter 4 presents the experiment on the generation of spin-squeezed state by stroboscopic backaction evading measurement based on the micro-fabricated vapor cell coupled into an optical cavity. In Chapter 5 as an application of the established method of conditional spin squeezing, atomic magnetometer beyond the quantum noise limit is demonstrated. Chapter 6 details the experiment on teleportation between two atomic ensembles and the theory behind the experiment.

The thesis is concluded in Chapter 7 where I summarize the main results in this thesis and give an outlook about the coming experiments based on the same setup.

Chapter 2

Quantum interface between light and atoms

In this section we describe the off-resonant dipole atom-light interaction utilizing the ground state $6S_{1/2}$ to the excited state $6P_{3/2}$ transition in cesium where collective spin operators for atoms and Stokes operators for light are described in canonical operators in the language of continuous variables. The interface between light and atoms provides the basis for the experiments discussed in the thesis. Since most of the work presented in this thesis is in the QND picture where the tensor interaction is negligible by using a larger blue detuning of the probe light, we focus on the equation of motion and the input-output relation that are often used in the following chapter. However, we give some description of the tensor interaction and entanglement that will be used to discuss the quantum teleportation between two atomic ensembles. At the end of this chapter, the concept of motion averaging for the thermal atoms is discussed which is very important in the collective effect, and relates to the single photon generation in DLCZ scheme.

2.1 Canonical variables

2.1.1 Light

To describe the interaction between light and atom involved in all the experiments of this thesis, the quantum state of light is characterized by the Stokes operators $\hat{S}_x$,$\hat{S}_y$ and $\hat{S}_z$, which are given by the differences of the number operators $\hat{n}_{polarization}$ of the photons polarized in

different orthogonal bases. For the light propagating in z-direction we have

$$\begin{aligned}\hat{S}_x &= \frac{1}{2}(\hat{n}_x - \hat{n}_y)\\ \hat{S}_y &= \frac{1}{2}(\hat{n}_{+45^\circ} - \hat{n}_{-45^\circ})\\ \hat{S}_z &= \frac{1}{2}(\hat{n}_{\sigma_+} - \hat{n}_{\sigma_-}),\end{aligned} \tag{2.1}$$

where the indices x,y of $\hat{n}_{polarization}$ represent the photons polarized in x- or y-direction and $\pm 45^\circ$ label the photons polarized in $\pm 45^\circ$-direction, while $\sigma_\pm$ show the photons circularly polarized in the left or right hand direction. The Stokes vector satisfies the commutation of angular momentum

$$[\hat{S}_y, \hat{S}_z] = i\hat{S}_x, \tag{2.2}$$

which shows the Heisenberg uncertainty principle as

$$Var(\hat{S}_y) \cdot Var(\hat{S}_z) \geq \frac{\langle S_x \rangle^2}{4}. \tag{2.3}$$

In the experiment, we always use x- or y- linearly polarized coherent light pulse to interact with the atomic ensembles, which means S_x can be treated as a large classical value proportional to the flux of photons $\Phi = P/(\hbar\omega)$ while P represents the optical power and $\hbar\omega$ is the energy of single photon. The quantum variables $\hat{S}_y$ and $\hat{S}_z$ are the physical variables we are interested in, and usually they have zero mean value since a collection of x-polarized photons holds the equal probability for the polarization of $\pm 45^\circ$ or $\sigma_\pm$. The canonical operators of light can be defined as

$$\hat{x}_L = \frac{\hat{S}_y}{\sqrt{|S_x|}}, \quad \hat{p}_L = {}^{\sigma_{S_X}}\frac{\hat{S}_z}{\sqrt{|S_x|}}, \rightarrow [\hat{x}_L, \hat{p}_L] \approx i, \tag{2.4}$$

where $\sigma_{S_x} = \pm 1$depends on the sign of S_x. In the setting of the experiments involved in this thesis a y-polarized coherent light pulse usually serves as the drive light as well as a phase reference for the x-polarized signal part which carries the interesting quantum fluctuation (that is the reason we use the polarization homodyne detection instead of typical homodyne system with an addition strong local beam), and the canonical operators can be represented by the creation and annihilation operators $\hat{a}_x$ and $\hat{a}_x^\dagger$ of light in x-polarization,

$$\hat{x}_L = \tfrac{1}{\sqrt{2}}(\hat{a}_x + \hat{a}_x^\dagger), \quad \hat{p}_L = \tfrac{1}{\sqrt{2}i}(\hat{a}_x - \hat{a}_x^\dagger), \tag{2.5}$$

If $Var(\hat{S}_y) = Var(\hat{S}_y) = \langle S_x \rangle/2$ (i.e.$Var(\hat{x}_L) = Var(\hat{p}_L) = 1/2$) we say that the noise of $\hat{S}_y$ or $\hat{S}_z$ is at the shot noise limit. Usually, one defines the creation and annihilation operators in time domain with the commutation relation $[\hat{a}_x(t,z), \hat{a}_x^\dagger(t',z)] = \delta(k-k')$. In the position space it will follow $[\hat{a}_x(z,t), \hat{a}_x^\dagger(z',t)] = c\delta(z-z')$.

2.1.2 Atoms

We will describe the atomic states of an ensemble in terms of its collective spin in the different directions, which is given by the sum of the total angular momenta of the individual atoms $\hat{j}_i^k$:

$$\hat{J}_i = \sum_k^{N_a} \hat{j}_i^k \tag{2.6}$$

with $i = x,y,z$. Since the ensemble contains such a vast amount of atoms those spin variables are quasi continuous. The collective spin follows, as do the individual spins, the commutation relation of angular momentum,

$$[\hat{J}_y, \hat{J}_z] = i\hat{J}_x, \tag{2.7}$$

so the Heisenberg uncertainty principle reads

$$Var(\hat{J}_y) \cdot Var(\hat{J}_z) \geq \frac{\langle J_x \rangle^2}{4}. \tag{2.8}$$

In the experiments we discuss here, typically the atomic spins are all oriented along the x-direction. This is achieved by pumping the atoms into $F = 4, m_F = 4$ of the $6S_{1/2}$ ground state , which will be discussed later. The maximal value of the spin component in x-direction is $J = 4 \cdot N_a$, where N_a is the number of atoms. And in the case of the fully oriented atomic state, the longitudinal component of the collective spin $\hat{J}_x$ can be considered to be a classical quantity and can be accordingly replaced by its mean value $\langle J_x \rangle \approx \langle J \rangle$. The spins $\hat{J}_y, \hat{J}_z$ of the fully oriented state in the perpendicular directions follow Gaussian probability distributions with a mean value of 0 and the variances $Var(\hat{J}_y) = Var(\hat{J}_z) = \frac{J}{2}$. This is easily understood, if one considers all atoms in $F = 4, m_F = 4$. Since there are many independent atoms, we can assume $\langle J_x^2 \rangle \approx F^2 \cdot N_a$ and therefore

$$\begin{aligned} Var(\hat{J}_y) &= \langle \hat{J}_y^2 \rangle = \sum_k \hat{j}_y^{k2} = \langle \hat{J}_z^2 \rangle = \frac{F \cdot (F+1) N_a - \langle J_x^2 \rangle}{2} \\ &= \frac{F}{2} \cdot N_a = \frac{J}{2}. \end{aligned} \tag{2.9}$$

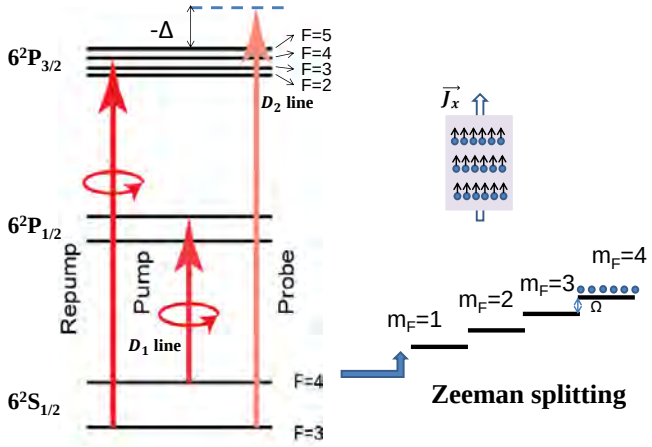

Fig. 2.1 The figure on the left shows the level scheme of the D1 and D2 line of Cesium. All the atoms are pumped into the $F = 4, m_F = 4$ state, so that they are oriented along x. The magnetic field leads to a splitting of the magnetic sublevels by the Larmor frequency Ω.

This state is called a coherent spin state(CSS) and is the starting point of all our experiments. For highly oriented many atom systems we can use the Holstein-Primakoff approximation [28]. We identify the fully oriented state as the ground state of an harmonic oscillator. The Holstein-Primakoff transformation maps spin operators to bosonic creation and annihilation operators $\hat{b}^\dagger$ and $\hat{b}$ with $[\hat{b}, \hat{b}^\dagger] = 1$. The collective ladder operators $\hat{J}_\pm = \hat{J}_y \pm i\hat{J}_z$ are expressed in terms of $\hat{b}^\dagger$ and $\hat{b}$ by

$$\hat{J}_+ = \sqrt{N_a}\sqrt{1 - \frac{\hat{b}^\dagger\hat{b}}{N_a}}\hat{b}, \quad \hat{J}_- = \sqrt{N_a}\sqrt{1 - \frac{\hat{b}^\dagger\hat{b}}{N_a}}\hat{b}^\dagger. \tag{2.10}$$

In the right of Figure 2.1 one can see a schematic drawing of the atomic level structure of the hyperfine ground state we use (F=4). All the atoms start in the $m_F = 4$ ground state and an excitation in the described language leads to one atom in the $m_F = 3$ state. The transformation for $\hat{J}_x$ can be obtained using the identity $\hat{J}_x^2 = J(J+1) - \hat{J}_y^2 - \hat{J}_z^2 = J(J+1) - \frac{1}{2}(\hat{J}_+\hat{J}_- + \hat{J}_-\hat{J}_+) = (J - \hat{b}^\dagger\hat{b})^2$.

By identifying $\hat{J}_x = J - \hat{b}^\dagger\hat{b}$, the fully polarized initial state $|\Psi_{CSS}\rangle = |J,J\rangle$ can be mapped to the ground state of an harmonic oscillator $|J,J\rangle = |0\rangle_A$,such that the expression $\hat{J}_x|J,J\rangle = J|J,J\rangle$ corresponds to $(J - \hat{b}^\dagger\hat{b})|0\rangle_A = J|0\rangle_A$. This transformation is exact. If the atomic state is close to the CSS, $\frac{\langle\hat{b}^\dagger\hat{b}\rangle}{\langle J\rangle} \ll 1$ can be assumed. In this case, Equation 2.10 can be expended in a series to first order and approximated by $\hat{J}_+ \approx \sqrt{N_a}\hat{b}$ and $\hat{J}_- \approx \sqrt{N_a}\hat{b}^\dagger$. Within this approximation, the transverse components of the collective spin are given by $\hat{J}_y = (\hat{J}_+ +$

$\hat{J}_-)/2 \approx \sqrt{|J|}(\hat{b}+\hat{b}^\dagger)/\sqrt{2}$ and $\hat{J}_z = -i(\hat{J}_+ - \hat{J}_-)/2 \approx \sqrt{|J|}(\hat{b}-\hat{b}^\dagger)/(\sqrt{2}i)$, and can be identified with the atomic quadratures

$$\hat{x}_A = \frac{\hat{J}_y}{\sqrt{J}} \approx \frac{1}{\sqrt{2}}(\hat{b}+\hat{b}^\dagger), \quad \hat{p}_A = \frac{\hat{J}_z}{\sqrt{J}} \approx \frac{-i}{\sqrt{2}}(\hat{b}-\hat{b}^\dagger), \tag{2.11}$$

which follow the commutation relation $[\hat{x}_A, \hat{p}_A] \approx i$.

2.2 Interaction between light and atoms

2.2.1 Hamiltonian

In the standard electric dipole interaction description, the Hamiltonian for single atom situation can be written as $\hat{H} = -\mathbf{d}\cdot\mathbf{E}$, where $\mathbf{d} = -e\mathbf{r}$ is the dipole operator of a single atom with the vector $\mathbf{r}$.

By adiabatically eliminating the excited states with the consideration of interaction with far off-resonant light, the effective Hamiltonian can be written as

$$\hat{H}_{int}^{eff} = \mathbf{E}^{(-)}\alpha\mathbf{E}^{(+)}, \tag{2.12}$$

with $\alpha = -\sum_{F'} \frac{P_g \mathbf{d} P_{F'} \mathbf{d} P_g}{\Delta_{F'}}$, where$P_F = \sum_m |F,m\rangle \langle F,m|$, $P_g = \sum_F P_F$ and $P_{F'} = \sum_{m'} |F',m'\rangle \langle F',m'|$. And Here $\Delta_{F'}$ is the detuning of the light from the $S_{1/2}F \to P_{3/2}F'$ transition. Consider the transition between $F \to F$, the corresponding polarizability operator $\alpha_{FF} = P_F \alpha P_F$ can be decomposed into[29][30]

$$\alpha_{FF} = -\frac{d_0^2}{\Delta}(a_0 + ia_1\mathbf{j}\times + a_2\mathbf{Q}), \tag{2.13}$$

where $d_0^2 = (2J'+1)\left|\langle J' \| d \| J\rangle\right|^2$ is the dipole matrix element with the electronic angular momenta of the ground and excited states of J and J', respectively. Additionally, a_0, a_1 and a_2 are the dimensionless scalar, vector and tensor polarizabilities which are the function of the detuning Δ. And the corresponding formula for Cs atomic D1 and D2 transition can be found at the end of this section. As shown in Equation 2.13, there are three terms totally involved into the interaction between light and atoms representing the scalar, vector and

tensor interaction, respectively. In the vector component,

$$\mathbf{j}\times = \begin{pmatrix} 0 & j_z & j_y \\ j_z & 0 & -j_x \\ -j_y & j_x & 0 \end{pmatrix} \tag{2.14}$$

and the corresponding Hamiltonian $\hat{H}^1_{FF} = \mathbf{E}^{(-)}\alpha_{FF}\mathbf{E}^{(+)}$ can be calculated by using the transformation of $\mathbf{E}^{(-)} \cdot [\mathbf{j} \times \mathbf{E}^{(+)}] = \mathbf{j} \cdot [\mathbf{E}^{(-)} \times \mathbf{E}^{(+)}]$ and the fact of light propagating in z-direction only with x- and y-polarization parts. Finally, one can get the form of $\hat{H}^1_{FF} \propto j_z S_z$ with the defined Stokes operator $S_z = \frac{1}{2i}(\hat{a}^\dagger_x \hat{a}_y - \hat{a}_x \hat{a}^\dagger_y)$. The second rank tensor term $\mathbf{Q}$ is given as follow,

$$Q_{ij} = -(j_i j_j + j_j j_i) + \delta_{ij}\frac{2}{3}\mathbf{j}^2. \tag{2.15}$$

Consider the experimental setting where the light is interacting with a cloud of N_a atoms evenly filled in a container with the length of L and cross section area of A, one can finally obtain the complete Hamiltonian[31]

$$\begin{aligned} \hat{H}_{int} = -\frac{\hbar c\Gamma}{8A\Delta}\frac{\lambda^2}{2\pi}\int_0^L \{ & a_0\hat{\Phi}(z,t) + a_1\hat{S}_z(z,t)\hat{j}_z(z,t) \\ & + a_2[\hat{\Phi}(z,t)\hat{j}^2_z(z,t) - \hat{S}_-(z,t)\hat{j}^2_+(z,t) \\ & - \hat{S}_+(z,t)\hat{j}^2_-(z,t)]\}\rho A dz, \end{aligned} \tag{2.16}$$

where $\lambda = 852nm$ and $\Gamma = 2\pi \cdot 5.21$MHz are the wavelength of the probe light and the full width at half maximum (FWHM) linewidth of the excited state, respectively, while ρ is the atomic density. The first scalar term can be treated as a DC Stark shift, which equally shifts all atomic energy levels and proportional to the photon flux or light intensity. The second vector term gives us the desired Faraday rotation operation where the atomic spin $\mathbf{J}$ is rotated around the z-axis proportional to $\hat{S}_z$. Likewise, the Stokes vector $\mathbf{S}$ is rotated around the z-axis by an amount proportional to $\hat{J}_z$. The last tensor term gives rise to a complicated dynamical Stark shift which is useful in some quantum protocol[32, 33] and will vanish for large detunings with respect to hyperfine splitting of excited state as the coefficient a_2 goes to zero which is shown in Figure 2.3. For D2 transition starting from the

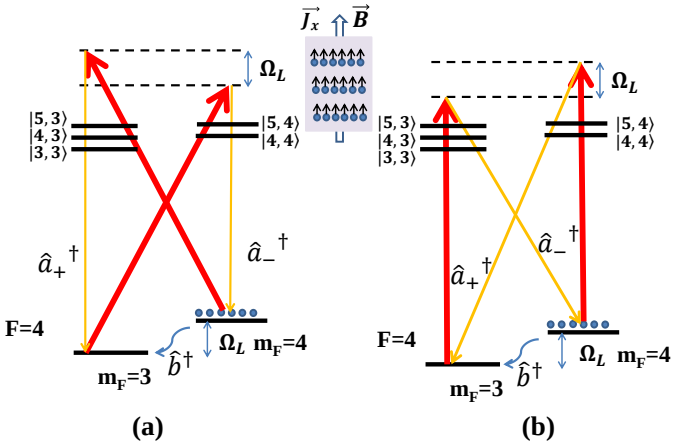

Fig. 2.2 The level scheme and relavant transitions when the bias magnetic field direction coincides with the spin orientation direction. The red thick lines and the orange lines represent the classical drive fields and quantum fields, respectively, where $\hat{a}_+^\dagger$ and $\hat{a}_-^\dagger$ are the creation operators of upper and lower band quantum fields with the frequency difference of $2\Omega_L$ while $\hat{b}^\dagger$ describes the creation of the atomic excitation, i.e. shuffling one atom away from the fully oriented state. (a) and (b) give the interaction pictures when y- and x- polarized drive light are used, respectively.

hyperfine ground state $F = 4$, the coefficients a_0, a_1, and a_2 are given by[31]

$$\begin{aligned} a_0 &= \frac{1}{4}\left(\frac{1}{1-\Delta_{35}/\Delta} + \frac{7}{1-\Delta_{45}/\Delta} + 8\right), \\ a_1 &= \frac{1}{120}\left(-\frac{35}{1-\Delta_{35}/\Delta} - \frac{21}{1-\Delta_{45}/\Delta} + 176\right), \\ a_2 &= \frac{1}{240}\left(\frac{5}{1-\Delta_{35}/\Delta} - \frac{21}{1-\Delta_{45}/\Delta} + 16\right), \end{aligned} \tag{2.17}$$

where $\Delta_{35} = 2\pi \cdot 452.24\text{MHz}$ and $\Delta_{45} = 2\pi \cdot 251.00\text{MHz}$ are the hyperfine splitting in the Cs excited state $6P_{3/2}$, respectively, while Δ is the laser detuning with respect to $6P_{3/2}F' = 5$.

2.2.2 Propagation equations

In the Heisenberg equation of motion,

$$\frac{\partial}{\partial t}\hat{j}_i(z,t) = \frac{1}{i\hbar}[\hat{j}_i(z,t), \hat{H}], \quad \left(\frac{\partial}{\partial t} + c\frac{\partial}{\partial z}\right)\hat{S}_i(z,t) = \frac{1}{i\hbar}[\hat{S}_i(z,t), \hat{H}], (i = x,y,z) \tag{2.18}$$

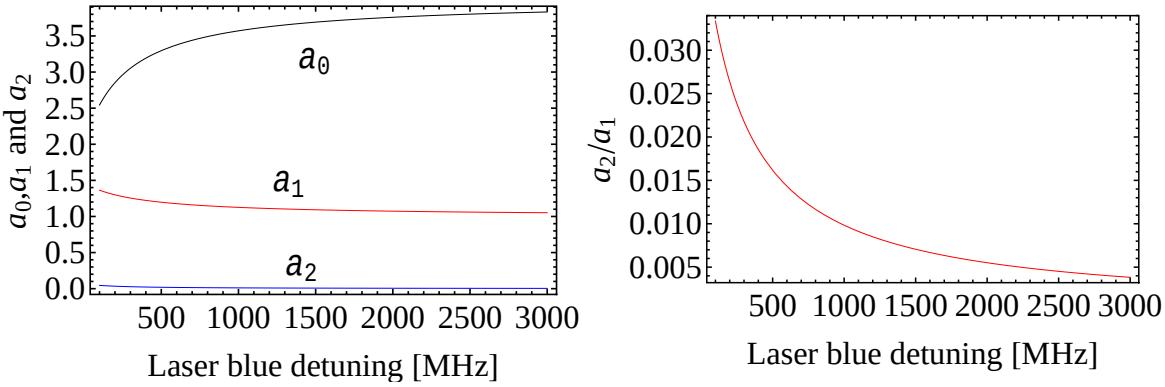

(a) a coefficients VS blue detuning

(b) a2/a1 ratio VS blue detuning

Fig. 2.3 a coefficients vs. Laser detuning($\Delta < 0$)

In the derivation of the right equation, the electric field is describe in k-space as $E(z,t) = \int dk \sqrt{\frac{\hbar\omega}{2\pi 2\varepsilon_0 A}}[\hat{a}(k,t)e^{ikz} + \hat{a}^\dagger(k,t)e^{-ikz}]$ with the commutation $[\hat{a}(k,t),\hat{a}^\dagger(k',t)] = \delta(k-k')$, which in turn gives the Fourier transformation $\hat{a}(z,t) = \frac{1}{\sqrt{2\pi}}\int_{-\infty}^{\infty}\hat{a}(k,t)e^{ikz}dk$.

$$\begin{aligned}
\frac{\partial}{\partial t}\hat{j}_x(z,t) &= \frac{c\Gamma\lambda^2}{8A\Delta 2\pi}\left\{a_1\hat{S}_z\hat{j}_y + a_2(2\hat{S}_y[\hat{j}_x\hat{j}_z + \hat{j}_z\hat{j}_x] - (2\hat{S}_x - \hat{\phi})[\hat{j}_z\hat{j}_y + \hat{j}_y\hat{j}_z])\right\},\\
\frac{\partial}{\partial t}\hat{j}_y(z,t) &= \frac{c\Gamma\lambda^2}{8A\Delta 2\pi}\left\{-a_1\hat{S}_z\hat{j}_x + a_2(-2\hat{S}_y[\hat{j}_z\hat{j}_y + \hat{j}_y\hat{j}_z] - (2\hat{S}_x + \hat{\phi})[\hat{j}_x\hat{j}_z + \hat{j}_z\hat{j}_x])\right\},\\
\frac{\partial}{\partial t}\hat{j}_z(z,t) &= \frac{c\Gamma\lambda^2}{8A\Delta 2\pi}a_2(-4\hat{S}_y[\hat{j}_x^2 - \hat{j}_y^2] + 4\hat{S}_x[\hat{j}_x\hat{j}_y + \hat{j}_y\hat{j}_x]),
\end{aligned} \tag{2.19}$$

$$\begin{aligned}
\frac{\partial}{\partial z}\hat{S}_x(z,t) &= \frac{\rho\Gamma\lambda^2}{8A\Delta 2\pi}\left\{a_1\hat{S}_y\hat{j}_z + a_2 2\hat{S}_z[\hat{j}_x\hat{j}_y + \hat{j}_y\hat{j}_x]\right\},\\
\frac{\partial}{\partial z}\hat{S}_y(z,t) &= \frac{\rho\Gamma\lambda^2}{8A\Delta 2\pi}\left\{-a_1\hat{S}_x\hat{j}_z - a_2 2\hat{S}_z[\hat{j}_x^2 - \hat{j}_y^2]\right\},\\
\frac{\partial}{\partial z}\hat{S}_z(z,t) &= \frac{\rho\Gamma\lambda^2}{8A\Delta 2\pi}a_2[2\hat{S}_y[\hat{j}_x^2 - \hat{j}_y^2] - 2\hat{S}_x[\hat{j}_x\hat{j}_y + \hat{j}_y\hat{j}_x]],
\end{aligned} \tag{2.20}$$

In Equation 2.20, the $\frac{\partial}{\partial t}$ term has been removed by neglecting the retardation effect with the assumption of infinite speed of light c.

2.2.3 Input output relations in Quantum Non-demolition interaction picture

For large blue detuning of probe light with respect to hyperfine splitting of excited state, the term proportional to a_2 can be neglected, then the remaining part can be written as

$$\frac{\partial}{\partial t}\hat{j}_y(z,t) = -\frac{c\gamma\lambda^2}{8A\Delta 2\pi}a_1\hat{S}_z\hat{j}_x, \tag{2.21a}$$

$$\frac{\partial}{\partial t}\hat{j}_z(z,t) = 0, \tag{2.21b}$$

$$\frac{\partial}{\partial z}\hat{S}_y(z,t) = -\frac{\rho\gamma\lambda^2}{8\Delta 2\pi}a_1\hat{S}_x\hat{j}_z, \tag{2.21c}$$

$$\frac{\partial}{\partial z}\hat{S}_z(z,t) = 0, \tag{2.21d}$$

For thermal atoms as discussed in Chapter 2, the atoms move cross the light beam many times during the interaction time and the vapor cell is coupled into an optical cavity in our setup where the mean field is a good approximation. So the Stokes vectors and the spin operators can be replaced by their average value over the cell length with the definition $\left\langle \hat{j}_z(z,t)\right\rangle = \frac{1}{L}\int_0^L \hat{j}_z(z,t)dz$ and $\left\langle \hat{S}_z(z,t)\right\rangle = \frac{1}{L}\int_0^L \hat{S}_z(z,t)dz$. In the continuous notation of the collective spin components we have $\hat{J}_i(t) = \int_0^L \hat{j}_i(t)\rho A dz$, and we also know $\left\langle \hat{j}_i(z,t)\right\rangle = \frac{\hat{J}_i(t)}{L\rho A}$. Therefore, Equation 2.21 can be rewritten as

$$\frac{\partial}{\partial t}\hat{J}_y(t) = -c\cdot a\left\langle \hat{S}_z(z,t)\right\rangle \hat{J}_x(t), \tag{2.22a}$$

$$\frac{\partial}{\partial t}\hat{J}_z(t) = 0, \tag{2.22b}$$

$$\frac{\partial}{\partial z}\hat{S}_y(z,t) = -\frac{a}{L}\hat{S}_x(z,t)\hat{J}_z, \tag{2.22c}$$

$$\frac{\partial}{\partial z}\hat{S}_z(z,t) = 0, \tag{2.22d}$$

We define $\hat{S}_i^{in}(t) = c\cdot\hat{S}_i(z=0,t)$ and $\hat{S}_i^{out}(t) = c\cdot\hat{S}_i(z=L,t)$ which normalizes the Stokes vectors to photon per unit time. By integrating Equations 2.22 in space from $z=0$ to $z=L$ with an assumption of small rotation angles and large classical values of S_x and J_x, we can

get the following equations,

$$\hat{S}_y^{out}(t) = \hat{S}_y^{in}(t) + aS_x\hat{J}_z(t), \tag{2.23a}$$
$$\hat{S}_z^{out}(t) = \hat{S}_z^{in}(t), \tag{2.23b}$$
$$\frac{\mathrm{d}}{\mathrm{d}t}\hat{J}_y(t) = aJ_x\hat{S}_z^{in}(t), \tag{2.23c}$$
$$\frac{\mathrm{d}}{\mathrm{d}t}\hat{J}_z(t) = 0, \tag{2.23d}$$

where $a = -\frac{\Gamma\lambda^2}{8A\Delta 2\pi}a_1$.

In the experiment we use a homogeneous DC bias magnetic field in the spin orientation direction, which is x-direction in this thesis, corresponding to an additional term $\hat{H} = \Omega_L\hat{J}_x$ added in the Hamiltonian with $\Omega_L = g_F\mu_B B/\hbar$, where $g_F(F=4) \approx 0.2504$ and $g_F(F=3) \approx -0.2512$ are the hyperfine Landé g-factors for the ground state of cesium, while μ_B and B are the Bohr Magneton and the magnitude of the applied magnetic field. Typically, we encode the quantum states of atoms and light at this Larmor frequency $\Omega_L \approx 400$kHz since the technical noise is much lower than that at lower frequencies, which promises us to achieve projection noise level for the atoms and shot noise level for the light. To solve the equation of motion for atoms precessing at Larmor frequency Ω_L we introduce the rotating frame coordinates

$$\begin{pmatrix} \hat{J'}_y \\ \hat{J'}_z \end{pmatrix} = \begin{pmatrix} \cos(\Omega_L t) & \sin(\Omega_L t) \\ -\sin(\Omega_L t) & \cos(\Omega_L t) \end{pmatrix} \begin{pmatrix} \hat{J}_y \\ \hat{J}_z \end{pmatrix} \tag{2.24}$$

and then the Equation2.23 is transformed into,

$$\hat{S}_y^{out}(t) = \hat{S}_y^{in}(t) + aS_x(\hat{J'}_y(t)\sin(\Omega_L t) + \hat{J'}_z(t)\cos(\Omega_L t)), \tag{2.25a}$$
$$\hat{S}_z^{out}(t) = \hat{S}_z^{in}(t), \tag{2.25b}$$
$$\frac{\mathrm{d}}{\mathrm{d}t}\hat{J'}_y(t) = aJ_x\hat{S}_z^{in}(t)\cos(\Omega_L t), \tag{2.25c}$$
$$\frac{\mathrm{d}}{\mathrm{d}t}\hat{J'}_z(t) = -aJ_x\hat{S}_z^{in}(t)\sin(\Omega_L t), \tag{2.25d}$$

By looking at the first line of Equation 2.25, it is found that both $\hat{J'}_y$ and $\hat{J'}_z$ with the phase difference of $\pi/2$ contribute to the light component $\hat{S}_y$ after the interaction. However, it is not allowed to do the measurement with high precision on both of them simultaneously since they are non-commuting. Due to the fact of the unchanged $\hat{S}_z$ during the interaction,

we can get the dynamics of $\hat{J'}_y$ and $\hat{J'}_z$ as follow,

$$\begin{aligned}\hat{J'}_y(t) &= \hat{J'}_y(0) + \int_0^t aJ_x\hat{S}_z^{in}(t')\cos(\Omega_L t')dt',\\ \hat{J'}_z(t) &= \hat{J'}_z(0) - \int_0^t aJ_x\hat{S}_z^{in}(t')\sin(\Omega_L t')dt',\end{aligned} \tag{2.26}$$

As shown in Equation 2.26, the light component $\hat{S}_z^{in}$ is evolved into the dynamics of both spin components, while at the same time the spin state is fed back onto the light, which means the earlier $\hat{S}_z^{in}$ is thus imprinted onto $\hat{S}_y^{out}$. This source is the so-called backaction noise of the light, which will be discussed in detail later.

The remaining part of this section is devoted to input-output relations for the QND-type interaction by using the definition of canonical variables for light and atoms. We can rewrite Equation 2.25 as follow by inserting Equation 2.4 and 2.11,

$$\hat{x}_L^{out}(t) = \hat{x}_L^{in}(t) + a(\hat{x}_A(t)\sin(\Omega_L t) + \hat{p}_A(t)\cos(\Omega_L t)), \tag{2.27a}$$

$$\hat{p}_L^{out}(t) = \hat{p}_L^{in}(t), \tag{2.27b}$$

$$\frac{\mathrm{d}}{\mathrm{d}t}\hat{x}_A(t) = a\hat{p}_L(t)\cos(\Omega_L t), \tag{2.27c}$$

$$\frac{\mathrm{d}}{\mathrm{d}t}\hat{p}_A(t) = -a\hat{p}_L(t)\sin(\Omega_L t), \tag{2.27d}$$

where $\hat{x}_L^{in}(\hat{p}_L^{in})(t) = \hat{x}_L(\hat{p}_L)(z=0,t)$ and $\hat{x}_L^{out}(\hat{p}_L^{out})(t) = \hat{x}_L(\hat{p}_L)(z=L,t)$, while $\hat{x}_A \propto \hat{J'}_y$ and $\hat{p}_A \propto \hat{J'}_z$. Equation 2.26 can be rewritten as

$$\begin{aligned}\hat{x}_A(t) &= \hat{x}_A(0) + a\int_0^t \hat{p}_L(t')\cos(\Omega_L t')dt',\\ \hat{p}_A(t) &= \hat{p}_A(0) - a\int_0^t \hat{p}_L(t')\sin(\Omega_L t')dt'.\end{aligned} \tag{2.28}$$

These are then inserted into Equation 2.27 to calculate the cosine and sine mode of $\hat{x}_L^{out}$ and $\hat{p}_L^{out}$ integrated over the interaction duration T, which are the measured variables in the experiment by utilizing the Lock-in Amplifier

$$\begin{aligned}\hat{x}_c^{out} &= \sqrt{\frac{2}{T}}\int_0^T dt\cos(\Omega_L t)\hat{x}_L^{out}(t)\\ &= \hat{x}_c^{in} + \frac{\kappa}{\sqrt{2}}\hat{p}_A^{in} - \kappa^2\sqrt{\frac{2}{T^3}}\int_0^T dt\cos^2(\Omega_L t)\int_0^t dt'\hat{p}_L(t')\sin(\Omega_L t')\\ &\approx \hat{x}_c^{in} + \frac{\kappa}{\sqrt{2}}\hat{p}_A^{in} - \kappa^2\sqrt{\frac{2}{T^3}}\int_0^T dt(\frac{T-t}{2})\hat{p}_L(t)\sin(\Omega_L t),\end{aligned} \tag{2.29}$$

where the coefficient $\sqrt{\frac{2}{T}}$ comes from the normalization of quadratures while $\kappa = a\sqrt{T}$. We assume here the interaction duration T is much larger than $1/\Omega_L$ and the evolution is much slower than $1/\Omega_L$, thus the term $\hat{x}_L(t)$ proportional to $\cos(\Omega_L t)\sin(\Omega_L t)$ is neglected. We define a new variable to describe the backaction term mentioned above as

$$\hat{p}_{s,1} = \sqrt{\frac{24}{T^3}} \int_0^T dt(\frac{T}{2} - t)\hat{p}_L(t)\sin(\Omega_L t), \tag{2.30}$$

and $\hat{p}_{c,1}$ and $\hat{x}_{c/s,1}$ similarly which satisfy the commutation relations $[\hat{p}_{c/s,1}, \hat{p}_{c/s}] = [\hat{p}_{c/s,1}, \hat{x}_{c/s}] = 0$. Finally, we can obtain the input-output relations for the single cell,

$$\begin{aligned}
\begin{pmatrix} \hat{x}_A^{out} \\ \hat{p}_A^{out} \end{pmatrix} &= \begin{pmatrix} \hat{x}_A^{in} \\ \hat{p}_A^{in} \end{pmatrix} + \frac{\kappa}{\sqrt{2}} \begin{pmatrix} \hat{p}_c^{in} \\ \hat{p}_s^{in} \end{pmatrix}, \\
\begin{pmatrix} \hat{x}_c^{out} \\ \hat{x}_s^{out} \end{pmatrix} &= \begin{pmatrix} \hat{x}_c^{in} \\ \hat{x}_s^{in} \end{pmatrix} + \frac{\kappa}{\sqrt{2}} \begin{pmatrix} \hat{p}_A^{in} \\ -\hat{x}_A^{in} \end{pmatrix} + \frac{\kappa^2}{4} \begin{pmatrix} \hat{p}_s^{in} \\ -\hat{p}_c^{in} \end{pmatrix}, \\
&\quad + \frac{\kappa^2}{4\sqrt{3}} \begin{pmatrix} \hat{p}_{s,1}^{in} \\ -\hat{p}_{c,1}^{in,} \end{pmatrix},
\end{aligned} \tag{2.31}$$

and $\hat{p}_L$ is conserved in terms of

$$\hat{p}_{c/s}^{out} = \hat{p}_{c/s}^{in} \tag{2.32}$$

2.2.4 Tensor interaction

As mentioned before, the higher order parts in the Hamiltonian 2.16 make the description of the interaction between light and atoms quite complicated. However, they are of importance in some quantum protocols such as quantum teleportation between two remote atomic ensembles (discussed in Chapter 6) and so on. In this section, I am trying to explain the effects resulting from them in the experimental setting, which means the highly orientated atomic ensembles and x or y linearly polarized light. By using the density operator $\hat{\sigma}_{jk} = |j\rangle\langle k|$, the spin components of ensemble with quantization in x-direction can be written as

$$\begin{aligned}
\hat{j}_x &= \sum_m m\hat{\sigma}_{mm}, \\
\hat{j}_y &= \frac{1}{2}\sum_m m\sqrt{F(F+1) - m(m+1)}(\hat{\sigma}_{m+1,m} + \hat{\sigma}_{m,m+1}), \\
\hat{j}_z &= \frac{1}{2i}\sum_m m\sqrt{F(F+1) - m(m+1)}(\hat{\sigma}_{m+1,m} - \hat{\sigma}_{m,m+1}),
\end{aligned} \tag{2.33}$$

where m is the magnetic quantum number. Intuitively, in the presence of a magnetic field, the diagonal elements of the density matrix will be constant contributing DC components int the spectrum, the first off-diagonal elements will rotate with Larmor frequency Ω_L, the second off-diagonal elements at $2\Omega_L$, and so on. Since the atomic spins are highly oriented in x-direction, we can safely only consider the terms related to $m_F = 3$ and $m_F = 4$.

$$\begin{aligned}
\hat{j}_y\hat{j}_z + \hat{j}_z\hat{j}_y &= \frac{1}{2i}\sum_m m\sqrt{(F-m)(F+m)(F+1+m)(F+1-m)} \\
&\quad \times (\hat{\sigma}_{m+1,m-m} + \hat{\sigma}_{m-1,m+1}) \approx 0, \\
\hat{j}_x\hat{j}_y + \hat{j}_y\hat{j}_x &= \frac{1}{2}\sum_m m\sqrt{F(F+1)-m(m+1)}(2m+1) \\
&\quad \times (\hat{\sigma}_{m+1,m} + \hat{\sigma}_{m,m+1}) \approx \sigma^{j_x}(2F-1)\hat{j}_y, \\
\hat{j}_x\hat{j}_z + \hat{j}_z\hat{j}_x &= \frac{1}{2i}\sum_m m\sqrt{F(F+1)-m(m+1)}(2m+1) \\
&\quad \times (\hat{\sigma}_{m+1,m} - \hat{\sigma}_{m,m+1}) \approx \sigma^{j_x}(2F-1)\hat{j}_z,
\end{aligned} \tag{2.34}$$

$$\hat{j}_x^2 \approx F^2, \hat{j}_y^2 \approx \hat{j}_z^2 \approx F/2, \hat{j}_x^2 - \hat{j}_y^2 \approx F(F-1/2). \tag{2.35}$$

With the approximation in Equation 2.34 and 2.35, the Hamiltonian in Equation 2.16 can be reduced to

$$\begin{aligned}
\hat{H} = \frac{-\hbar\Gamma\lambda^2}{8A\Delta 2\pi}\int_0^L dz[&a_1\hat{S}_z\hat{j}_z - a_2\cdot 14\hat{j}_y\hat{S}_y \\
&+ a_2(-21\hat{j}_x + 56)\hat{S}_x + (a_0 + a_2(-7/2\hat{j}_x - 16))\hat{\Phi}].
\end{aligned} \tag{2.36}$$

Besides the Faraday interaction term $\hat{S}_z\hat{j}_z$, only the term $\hat{S}_y\hat{j}_y$ is of importance among all the terms shown in Equation 2.36. First, the part proportional to $\hat{\Phi}$ but without spin operator can be neglected since it induces a shift for all the levels. Secondly, the terms containing $\hat{S}_x\hat{j}_x$ and $\hat{\Phi}\hat{j}_x$ cause atoms to experience the rotation in the $\hat{j}_y - \hat{j}_z$ plane from the linear Stark shift due to the fact of the highly orientated atoms and light field. In the experiment, this effect behaves as the Larmor frequency shift when shining the probe light on the atom ensembles which can be compensated by tuning the demodulation frequency of the lock-in Amplifier or giving a DC magnetic pulse during the probing process. The term left is that proportional to $\hat{S}_x$ but without spin operator, which leads to a small rotation angle in the $\hat{S}_y - \hat{S}_z$ plane, and is negligible. In order to look at the interaction more intuitively, we can

rewrite the Hamiltonian 2.36 by introducing the canonical variables,

$$\begin{aligned}\hat{H} &= \frac{-\hbar\Gamma\lambda^2}{8A\Delta 2\pi}\int_0^L dz[a_1\hat{S}_z\hat{j}_z - a_2\cdot 14\hat{j}_y\hat{S}_y] \\ &= \hbar a[\hat{p}_A\hat{p}_L + \zeta^2\hat{x}_A\hat{x}_L] \\ &= \frac{\hbar a}{2}[(\zeta^2+1)(\hat{a}_L\hat{b}_A^\dagger + \hat{a}_L^\dagger\hat{b}_A) - (1-\zeta^2)(\hat{a}_L^\dagger\hat{b}_A^\dagger + \hat{a}_L\hat{b}_A)].\end{aligned} \tag{2.37}$$

It is found that this Hamiltonian is a combination of beamsplitter operator and two-mode squeezing operator with different weight, i.e. $\hat{H}_{int} \propto [(\zeta^2+1)\hat{H}_{BS} - (1-\zeta^2)\hat{H}_{TMS}]$. And the weight coefficients are related to the ratio between vector and tensor coupling strength $\zeta^2 = 14\frac{a_2}{a_1}$. In other words, the relative strengths of two different interaction can be changed by detuning the laser frequency or choosing x- or y-polarization of probe beam. The latter method can be explain by Figure 2.2, where if a strong y-polarized laser beam is used to drive the interaction, the manifolds of $|3,3\rangle$, $|4,3\rangle$ and $|5,3\rangle$ in the excited state $6P_{3/2}$ are involved into the two-mode squeezing type interaction with the creation of upper sideband blue photon, while the beamsplitter type interaction involves $|4,4\rangle$, $|5,4\rangle$ with the creation of lower sideband red photon. Similarly, the case of strong x-polarized probe light can be analyzed, but the manifolds-picture is different. As we know, different manifolds interference will determine the final ratio of interaction strengths from $\hat{H}_{BS}$ and $\hat{H}_{TMS}$ related to the combination of Clebsch-Gordan coefficients. Therefore, by choosing the linear polarization direction of probe light one can manipulate the relative weights of beamsplitter interaction and two-mode squeezing interaction. In the following I will give the general Equation 2.38 for the output light operators where the higher order interaction and atomic decoherence are

included[34], and then show a example of how to derive one of them.

$$\begin{aligned}
\begin{pmatrix} \hat{x}^{out}_{c,-} \\ \hat{x}^{out}_{s,-} \\ \hat{p}^{out}_{c,-} \\ \hat{p}^{out}_{s,-} \end{pmatrix} &= \begin{pmatrix} \hat{x}^{in}_{c,-} \\ \hat{x}^{in}_{s,-} \\ \hat{p}^{in}_{c,-} \\ \hat{p}^{in}_{s,-} \end{pmatrix} - \frac{1-\varepsilon^2}{2} \begin{pmatrix} 1 & 0 & 0 & \frac{1}{\zeta^2} \\ 0 & 1 & -\frac{1}{\zeta^2} & 0 \\ 0 & -\zeta^2 & 1 & 0 \\ \zeta^2 & 0 & 0 & 1 \end{pmatrix} \begin{pmatrix} \hat{x}^{in}_{c,-} - \sqrt{1-\kappa^2\zeta^2}\hat{x}^{in}_{c,+} \\ \hat{x}^{in}_{s,-} - \sqrt{1-\kappa^2\zeta^2}\hat{x}^{in}_{s,+} \\ \hat{p}^{in}_{c,-} - \sqrt{1-\kappa^2\zeta^2}\hat{p}^{in}_{c,+} \\ \hat{p}^{in}_{s,-} - \sqrt{1-\kappa^2\zeta^2}\hat{p}^{in}_{s,+} \end{pmatrix} \\
&+ \frac{\kappa\sqrt{1-\varepsilon^2}}{\sqrt{2}} \begin{pmatrix} 0 & 1 \\ 1 & 0 \\ -\zeta^2 & 0 \\ 0 & \zeta^2 \end{pmatrix} \begin{pmatrix} \hat{x}_A(0) \\ \hat{p}_A(0) \end{pmatrix} \\
&+ \frac{\varepsilon\sqrt{1-\varepsilon^2}}{\sqrt{2}\varepsilon} \begin{pmatrix} 0 & 1 \\ 1 & 0 \\ -\zeta^2 & 0 \\ 0 & \zeta^2 \end{pmatrix} \begin{pmatrix} F_{x,-} - \sqrt{1-\kappa^2\zeta^2}F_{x,+} \\ F_{p,-} - \sqrt{1-\kappa^2\zeta^2}F_{p,+} \end{pmatrix}
\end{aligned} \tag{2.38}$$

where the light operators are defined with an exponentially rising or falling mode function as

$$\begin{aligned}
\hat{x}_{c,-} &= \frac{1}{N_-}\int_0^T dt \cos(\Omega_L t) e^{-\gamma t}\hat{x}(t), \quad \hat{x}_{c,+} = \frac{1}{N_+}\int_0^T dt \cos(\Omega_L t) e^{-\gamma(T-t)}\hat{x}(t), \\
\hat{x}_{s,-} &= \frac{1}{N_-}\int_0^T dt \sin(\Omega_L t) e^{-\gamma t}\hat{x}(t), \quad \hat{x}_{s,+} = \frac{1}{N_+}\int_0^T dt \sin(\Omega_L t) e^{-\gamma(T-t)}\hat{x}(t),
\end{aligned} \tag{2.39}$$

where $N_- = N_+ = \sqrt{\frac{1-e^{-2\gamma T}}{4\gamma}}$, and $\hat{p}_{c(s),-(+)}$ have the similar definition, while the decay rate $\gamma = \gamma_{swap} + \gamma_{bad}$ with $\gamma_{swap} = \frac{a^2\zeta^2}{2}$ and $\varepsilon^2 = \frac{\gamma_{bad}}{\gamma}$. And the rate γ_{bad} is the rate of the decoherence processes which leads to a decay of $\hat{x}_A$ and $\hat{p}_A$.

In order to derive Equation 2.38 where both the decoherence and higher order term of the Hamiltonian are included, let us firstly rewrite the Heisenberg-Langevin equations of the canonical variables of atomic spins as

$$\begin{aligned}
\dot{\hat{x}}_A &= a\hat{p}_L(t) - \frac{a^2\zeta^2}{2}\hat{x}_A - \Omega_L\hat{p}_A - \gamma_{bad}\hat{x}_A + \sqrt{2\gamma_{bad}}\hat{f}_x, \\
\dot{\hat{p}}_A &= -a\zeta^2\hat{x}_L(t) - \frac{a^2\zeta^2}{2}\hat{p}_A - \Omega_L\hat{x}_A - \gamma_{bad}\hat{p}_A + \sqrt{2\gamma_{bad}}\hat{f}_p,
\end{aligned} \tag{2.40}$$

where $\hat{f}_{x,p}$ are the noise operators due to the decoherence decay γ_{bad}. For more detail,

see[29]. The equations above can solved[35],

$$\begin{aligned}
\hat{x}_A(t) &= e^{-\gamma t}\hat{x}_A^{in} + a\int_0^t dt' e^{-\gamma(t-t')}\hat{p}_L(0,t')\cos(\Omega_L t') - a\zeta^2\int_0^t dt' e^{-\gamma(t-t')}\hat{x}_L(0,t')\sin(\Omega_L t') \\
&\quad + \sqrt{2\gamma_{bad}}\int_0^t dt' e^{-\gamma(t-t')}\hat{F}_x, \\
\hat{p}_A(t) &= e^{-\gamma t}\hat{p}_A^{in} - a\int_0^t dt' e^{-\gamma(t-t')}\hat{p}_L(0,t')\sin(\Omega_L t') - a\zeta^2\int_0^t dt' e^{-\gamma(t-t')}\hat{x}_L(0,t')\cos(\Omega_L t') \\
&\quad + \sqrt{2\gamma_{bad}}\int_0^t dt' e^{-\gamma(t-t')}\hat{F}_p.
\end{aligned} \tag{2.41}$$

Then by inserting $\hat{x}_A(t)$ and $\hat{p}_A(t)$ into Equation 2.27 we can calculate $\hat{x}_{c,-}^{out}$ as follow where the term proportional to $\cos(\Omega_L t)\sin(\Omega_L t)$ is neglected because of $T \ll 1/\Omega_L$,

$$\begin{aligned}
\hat{x}_{c,-}^{out} &= \frac{1}{N_-}\int_0^T dt\cos(\Omega_L t)e^{-\gamma t}\hat{x}^{out}(t) \\
&= \frac{1}{N_-}\int_0^T dt\cos(\Omega_L t)e^{-\gamma t}[\hat{x}(0,t) + a\hat{p}_A(t)\cos(\Omega_L t)] \\
&= \hat{x}_{c,-}^{in} + \frac{a}{N_-}\int_0^T dt\cos^2(\Omega_L t)e^{-\gamma t}[e^{-\gamma t}\hat{p}_A^{in} - a\int_0^t dt' e^{-\gamma(t-t')}\hat{p}_L(0,t')\sin(\Omega_L t') \\
&- a\zeta^2\int_0^t dt' e^{-\gamma(t-t')}\hat{x}_L(0,t')\cos(\Omega_L t') + \sqrt{2\gamma_{bad}}\int_0^t dt' e^{-\gamma(t-t')}\hat{F}_p]
\end{aligned} \tag{2.42}$$

By using the transformation

$$\begin{aligned}
\int_0^T dt\cos^2(\Omega_L t)e^{-2\gamma t}\int_0^t dt' f(t') &= \int_0^T dt f(t')\int_t^T dt'\cos^2(\Omega_L t)e^{-2\gamma t} \\
&= \int_0^T dt f(t)\frac{e^{-2\gamma t} - e^{-2\gamma T}}{4\gamma}
\end{aligned} \tag{2.43}$$

we get

$$\begin{aligned}
\hat{x}_{c,-}^{out} &= \hat{x}_{c,-}^{in} + aN_- \hat{p}_A^{in} \\
&- \frac{a^2}{N_-}\int_0^T dt\cos^2(\Omega_L t)e^{-2\gamma t}\int_0^t dt'\hat{p}_L(0,t')\sin(\Omega_L t')e^{\gamma t'} \\
&+ \frac{a^2\zeta^2}{N_-}\int_0^T dt\cos^2(\Omega_L t)e^{-2\gamma t}\int_0^t dt'\hat{x}_L(0,t')\cos(\Omega_L t')e^{\gamma t'} \\
&+ \frac{a\sqrt{2\gamma_{bad}}}{N_-}\int_0^T dt\cos^2(\Omega_L t)e^{-2\gamma t}\int_0^t dt'\hat{F}_p e^{\gamma t'} \\
&= \hat{x}_{c,-}^{in} + \sqrt{1-\varepsilon^2}\frac{\kappa}{\sqrt{2}}\hat{p}_A^{in} - \frac{1-\varepsilon^2}{2\zeta^2}(\hat{p}_{s,-}^{in} - \sqrt{1-\kappa^2\zeta^2}\hat{p}_{s,+}^{in}) \\
&- \frac{1-\varepsilon^2}{2}(\hat{x}_{c,-}^{in} - \sqrt{1-\kappa^2\zeta^2}\hat{x}_{c,+}^{in}) + \frac{\varepsilon\sqrt{1-\varepsilon^2}}{\sqrt{2}\varepsilon}(F_{p,-} - \sqrt{1-\kappa^2\zeta^2}F_{p,+})
\end{aligned} \tag{2.44}$$

where we define the coupling constant in the interaction picture with higher order term as $\kappa = \frac{\sqrt{1-e^{-2\gamma T}}}{\zeta}$.

2.3 Entanglement between light and atoms

2.3.1 Introduction to quantum entanglement

Entanglement between quantum systems, a pure quantum phenomenon, is related to the superposition principle of quantum mechanics. This nonlocal correlation more critical than classical one is one of the essential ingredients of quantum information processing. The concept of quantum entanglement firstly appeared in the article of ***Can Quantum-Mechanical Description of Physical Reality Be Considered Complete?*** written by A. Einstein, B. Podolsky and N. Rosen [36], and then was discussed by Schrödinger, Bohr and von Neumann.[37, 38, 39] Generally speaking, the quantum state of a two-party system is separable if and only if its total density operator ρ is a convex sum of product states

$$\rho = \sum_{i=1,2} p_i \rho_{i,1} \bigotimes \rho_{i,2}, \tag{2.45}$$

where $\rho_{i,1}$, and $\rho_{i,2}$ are assumed to be normalized states of mode 1 and 2 respectively, with $\sum_i p_i = 1$[42]. Otherwise, it is inseparable.Due to its nonlocality, the measurement on one of the remote subsystem affects the other subsystem deterministically. With the rapid development of experimental technology, the entangled states based on different mediums were not only generated in the lab[33, 40], but the long distance violation of Bell inequalitities

was also demonstrated[41]. According to whether or not the quantum states can be described in a finite Hilbert space, there are two different types of entanglement, DV and CV quantum entanglement. For instance, the entangled states of photon polarization and single spin direction are DV ones, while the entangled states based on the amplitude and phase quadratures of light field and the position and momentum of particle belong to the group of CV one. In this thesis, only the CV case is discussed since the ensemble contains such a vast amount of atoms those spin variables are quasi continuous. Although DV qubit states conceptually represent the simplest manifestation of the quantum mechanical superposition principle, and are most appropriate for quantum computation purposes being the natural extension of classical bits to the quantum realm, the probabilistic nature of the entangled states resource and the two-qubit Bell-sate measurement make it a difficult task. Instead of the DV resource, the deterministic CV entangled states can be relative easily generated, and described by the complete Bell-state measurement by means of homodyne detection.

Standing in front of quantum entangled resource, the critical task for us is to find the inseparability criteria for CV systems. In the beginning, theorists tried to translate the developed inseparability criteria for DV systems to the language for CV case by considering it as a infinite dimension DV system. For example, Simon proved that for the general case of arbitrary continuous-variable states, it is correct that a possible infinite-dimensional, continuous-variable version of the partial transpose criterion yields at best a sufficient and not a necessary condition, as it does for higher-dimensional discrete systems[43]. He also demonstrated that for Gaussian states, the partial transpose criterion represents not only a sufficient, but also a necessary inseparability condition[43]. Duan with his colleagues at the same time also proposed another inseparability criterion which is based on the calculation of the total variance of a pair of Einstein-Podolsky-Rosen (EPR) type operators, and is much closer to the experimental observation[42]. In the Theorem 2 presented in the paper, they gave the necessary and sufficient inseparability criterion for Gaussian states as follow: a Gaussian state ρ_G is separable if and only if the total variance inequality 2.46 is satisfied when expressed in its standard form II[42],

$$\left\langle (\Delta\hat{u})^2 \right\rangle_\rho + \left\langle (\Delta\hat{v})^2 \right\rangle_\rho \geqslant a_0^2 + \frac{1}{a_0^2}, \tag{2.46}$$

with the two EPR type operators

$$\hat{u} = a_0\hat{x}_1 - \frac{c_1}{|c_1|}\frac{1}{a_0}\hat{x}_2, \tag{2.47a}$$

$$\hat{v} = a_0\hat{p}_1 - \frac{c_2}{|c_2|}\frac{1}{a_0}\hat{p}_2, \quad [\hat{x}_i, \hat{p}_j] = i\delta_{i,j} \tag{2.47b}$$

where $a_0^2 = \sqrt{\frac{m_1-1}{n_1-1}} = \sqrt{\frac{m_2-1}{n_2-1}}$, c_1 and c_2 can be found in the correlation matrix of the Gaussian state defined in the standard form II[42]. Without the assumption of Gaussian states and without the need of any standard form for the correlation matrix, an alternative approach leads to an inequality similar to Equation 2.46, representing a necessary condition for separability (a sufficient condition for inseparability through its violation) for arbitrary states,

$$\left\langle (\Delta\hat{u})^2 \right\rangle_\rho + \left\langle (\Delta\hat{v})^2 \right\rangle_\rho \geqslant \bar{a}^2 + \frac{1}{\bar{a}^2}, \tag{2.48}$$

with the two EPR type operators

$$\hat{u} = |\bar{a}|\,\hat{x}_1 - \frac{1}{|\bar{a}|}\hat{x}_2, \tag{2.49a}$$

$$\hat{v} = |\bar{a}|\,\hat{p}_1 + \frac{1}{|\bar{a}|}\hat{p}_2. \tag{2.49b}$$

Here, $\bar{a}$ is an arbitrary nonzero real parameter. One can use Equation 2.48, satisfied by any separable state, in order to reveal that Inequality 2.46 is a necessary separability condition for the special case of Gaussian states. However, only for this special case does Inequality 2.46 also represent a sufficient separability condition. Let us also mention at this point that a similar (but weaker) inseparability criterion was derived by Tan[44], namely the necessary condition for any separable state

$$\left\langle (\Delta\hat{u})^2 \right\rangle_\rho \cdot \left\langle (\Delta\hat{v})^2 \right\rangle_\rho \geqslant 1, \tag{2.50}$$

with $\bar{a} = 1$ in Equation 2.48. It is simply the product version of the sum condition in 2.48 (with $\bar{a} = 1$). In the following, I will encounter inseparable states that do not violate the condition equation 2.50 (with $\bar{a} = 1$), but do violate the condition Equation 2.48, thereby revealing their inseparability. Finally, we emphasize that the sufficient inseparability criteria of Equation 2.48 (with $\bar{a} = 1$) and Equation 2.50 are useful for witnessing entanglement not only theoretically, but also experimentally.

2.3.2 Generation of the entanglement between light and atoms

As shown in Figure 2.2 and Equation 2.37, the Hamiltonian is a combination of beamsplitter operator and two-mode squeezing operator, $\hat{H}_{BS}$ and $\hat{H}_{TMS}$. In the setting of highly orientated atomic ensembles initially populated in $F = 4, m_F = 4$, $\hat{H}_{TMS}$ can be used to create the entanglement between atoms and upper sideband light mode. Here I will take the QND picture as example to explain the mechanism where $\hat{H}_{BS}$ and $\hat{H}_{TMS}$ share the same weight factor, and the weight factors can be changed by tuning the laser frequency or choosing x-

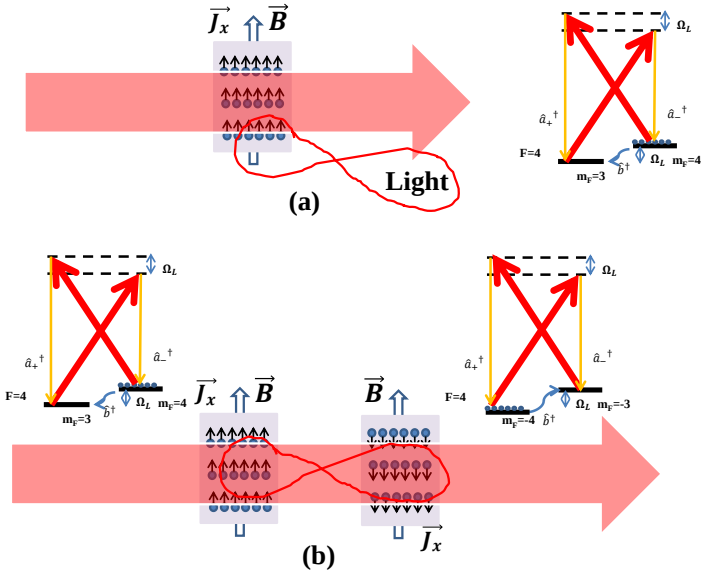

Fig. 2.4 Scheme of quantum entanglement generation. (a) shows the entanglement between light and atoms and (b) presents the establishment of entanglement between two atomic ensembles.

or y-polarization of probe beam as mentioned before. Firstly, the canonical variances of the upper sideband light mode can be constructed by using the definition formula 2.5 and Euler's formula as follow,

$$\hat{X}_L^{up} = \frac{1}{\sqrt{2}}(\hat{x}_s^{out} + \hat{p}_c^{out}), \quad \hat{P}_L^{up} = -\frac{1}{\sqrt{2}}(\hat{x}_c^{out} - \hat{p}_s^{out}) \tag{2.51}$$

since $\hat{x}\sin(\Omega_L t) + \hat{p}\cos(\Omega_L t) \propto -i(\hat{a}e^{i\Omega_L t} - \hat{a}^\dagger e^{-i\Omega_L t})$ and $\hat{x}\cos(\Omega_L t) - \hat{p}\sin(\Omega_L t) \propto (\hat{a}e^{i\Omega_L t} + \hat{a}^\dagger e^{-i\Omega_L t})$. Then we can use the sum of two EPR operators discussed above to see if there exists entanglement between atoms and light and furthermore to evaluate the strength of it.

$$Var(\hat{X}_L^{up} - \hat{x}_A^{out}) + Var(\hat{P}_L^{up} + \hat{p}_A^{out}) < 2, \tag{2.52}$$

In the QND interaction picture, let us insert the input output relations 2.31 and assume for the coherent states of light and atoms $Var(\hat{x}^{in}_{c/s/c,1/s,1}) = Var(\hat{p}^{in}_{c/s/c,1/s,1}) = \frac{1}{2}$ and $Var(\hat{x}_A^{in}) = Var(\hat{p}_A^{in}) = \frac{1}{2}$, respectivly. The corresponding result is shown in Figure 2.5 where the minimum variance 0.6 corresponding to 5.2dB entanglement is achieved when $\kappa = 1.7$. Notice that here the atomic decoherence and the light losses are not included. And one can use the Heisenberg-Langevin equations of the canonical variables of atomic spins similar to Equation 2.41 and the typical beamsplitter model for the light losses to derive the general

formula. And also if tensor coupling is involved into the interaction, the canonical variances of effective light mode are differently defined as

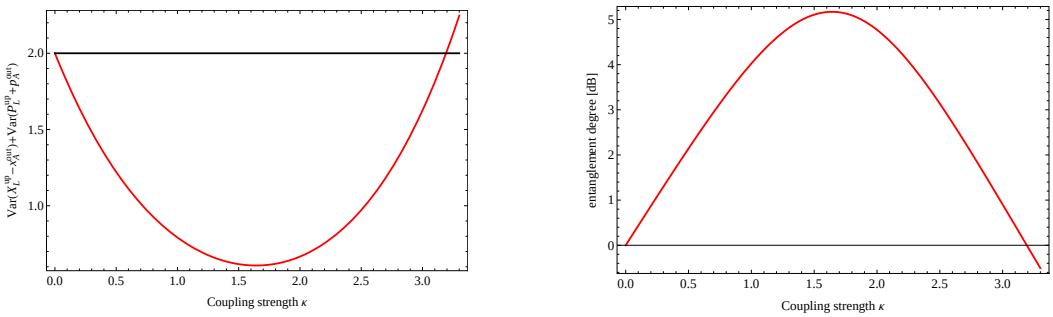

(a) (b)

Fig. 2.5 Collective variances of the output variables of atoms and light for QND interaction picture. (a) and (b) show the entanglement in ratio and dB unit, respectively.

$$\hat{X'}_L^{up} = \frac{1}{\sqrt{2}\zeta}(\hat{p}_{c-}^{out} - \zeta^2 \hat{x}_{s-}^{out}), \quad \hat{P'}_L^{up} = -\frac{1}{\sqrt{2}\zeta}(\hat{p}_{s-}^{out} + \zeta^2 \hat{x}_{c-}^{out}). \tag{2.53}$$

The analysis in detail can be found[32, 35]. Quantum entanglement between light and atoms is a basic block to construct the complicated quantum protocol, such as quantum teleportation, quantum memory and so on. Additionally, there exists another often used experimental setting where the light beam has interacted with two atomic ensembles in the magnetic field with oppositely oriented spins, i.e. $J_{x,1} = -J_{x,2} = J_x$. By doing quantum demolition measurement (QND) one can create the entanglement between these two atomic ensembles with the entanglement criteria as follow,

$$Var(\frac{\hat{J}_{y1} + \hat{J}_{y2}}{\sqrt{|J_x|}}) + Var(\frac{\hat{J}_{z1} + \hat{J}_{z2}}{\sqrt{|J_x|}}) < 2, \tag{2.54}$$

Since not used in the experiments of this thesis, I will not mention it here, and one can find the description in the previous theses[31, 34, 35].

2.4 Collective spin states in room temperature coated cells

2.4.1 Coating

Thermal atoms confined in a container will lose their spin orientation information after colliding with the bare glass walls, as a result of the interaction with the local electromagnetic field within the glass. Details can be found in Reference[45]. At present there exist two

methods with different mechanisms to suppress this effect and increase the spin coherence time (or called spin lifetime), one is to use the buffer gas to slow the atomic diffusion to the wall, and the other is to deposit the special chemical layer onto the inner surface of the cell. They have the different advantages in the applications, however, only the vapor cells with anti-relaxation coating are involved in the experimental research of this thesis. Some advantages and disadvantages of surface coating are summarized in the following.

1. spin-destruction collisions between alkali atoms and the buffer gas leads to the lost of spin angular momentum to motion momentum angular momentum and being destroyed, which broadens the magnetic linewidth. Especially when the cell size gets really smaller, one needs to increase the buffer gas pressure to keep the same diffusion time to the walls, however, the linewidth broadening resulting from alkali atoms colliding with buffer gas atoms becomes worse. Thus, anti-relaxation coating is usually utilized in the fabrication of miniature cells[26], where the linewidth can be greatly improved compared to the cell filled with buffer gases.

2. In the anti-relaxation coated cells there is no blockade for the atomic movement. Therefore, the whole cell can be treated as the active measurement volume even if the optical pumping beam dose not cover the cell perfectly due to motional averaging in the thermal vapor.

3. The atomic diffusion is relatively local in the cells filled with high pressure buffer gases. So the atoms in different parts of volume will precess with different Larmor frequency if there exists the magnetic field gradient, which will finally leads to the broadening of magnetic linewidth. However, this effect is reduced in the anti-relaxation coated cells, where the motional averaging makes the atoms precess on average over time with almost the same frequency with relative small fluctuation.

4. It is already 50 years since the first discovery of paraffin coating to protect the spin depolarization[46]. However, it is still commonly used below its melting temperature around $60^\circ \sim 80^\circ$, and also can maintain the spin polarization after up to 10^4 times of bounce[47]. Recently, it is reported that alkene coatings show a better performance in the surface coating and can support up to 10^6 alkali-metal-wall collisions before depolarizing the alkali-metal spins[48]. However, it only can be run below the melting temperature of 33°. Although Romalis's group and Balabas. et. al. reported different coating materials available at $160^\circ \sim 170^\circ$ and 100°, respectively[45, 49], their performances are not as good as that of the alkene coating at low temperature. So in the Spin-exchange relaxation-free magnetometry (SERF) achieving very high magnetic

field sensitivity in a near-zero magnetic field, the buffer gases is always used since it needs to operate at high temperature to obtain the high atomic density[50].

5. Although the study of the mechanism of relaxation of alkali atoms on the anti-relaxation coated wall was started in 1960[51], the precise nature of the physical and chemical interaction between alkali atoms and surface coating is still not fully understood. Additionally, the fabrication of coated cells is limited in the laboratories, and the fluctuation of the coating quality is quite large. Therefore, the way to develop the anti-relaxation coating technology is still hard and full of challenges.

2.4.2 Thermal averaging

In all the work presented in this thesis, the vapor cells at room-temperature are used to realize the quantum protocol for information and metrology application. The basic idea behind these applications is the atomic motional averaging which will be generally described here. The thermal velocity of atomic motion is $v = \sqrt{\frac{k_B T}{m_{Cs}}} \approx 137\text{m/s}$ at $T = 300K$, and the corresponding distribution follows the Maxwell-Boltzmann distribution with temperature T. The atomic motion leads to the Doppler broadening of $\nu^D_{FWHM} = \frac{\nu_0}{c}\sqrt{\frac{8k_B T \ln 2}{m_{Cs}}} = 378\text{MHz}$, where $\nu_0 = 351.726\text{THz}$ and c are the light frequency and speed, respectively, while k_B is the Boltzmann constant and m_{Cs} is the mass of Cesium atom with the value of $2.207 \times 10^{-25}\text{kg}$ [52]. Due to the fact that the atoms move in and out of the probe light beam many times if the interaction time is long enough, they on average have the same interaction strength with the light even if the laser beam does not fill the entire cell. And this is the typical setting where the transit time in the probe light with the diameter of beam waist $110\mu\text{m}$ is about $1\mu s$ and the interaction time is typically around $0.5ms$. Additionally, in the light propagation direction since $\Delta k \cdot L_{cell} = (\vec{k}_d - \vec{k}_q) \cdot L_{cell} \approx \Omega_L/c \cdot L_{cell} \ll \pi$, the atoms in different region of the cell experience almost the same phase $e^{i(\vec{k}_d - \vec{k}_q)z_i}$ where $\vec{k}_d$ and $\vec{k}_q$ are the wave vectors of drive and quantum light, respectively. Otherwise, if $\Delta k \cdot L_{cell}$ is comparable to π, the the atomic contribution will be washed out. The example can be found in[53], where the single photon source based on motional averaging is discussed.

Chapter 3

Experimental system

In this chapter, the experimental setup and measurement methods are presented in detail. The laser system and the corresponding function is discussed at first, which paves the way for preparation of initial spin states and probing processing. Then, the key element, microcell coupled into an optical cavity, is presented in Section 3.2 where the fabrication procedure is described in order to make the reader easily and intuitively understand the main results of this thesis. The general description of optical cavity is followed by another important part, characterization of the quality of our microcells and of optical pumping, which

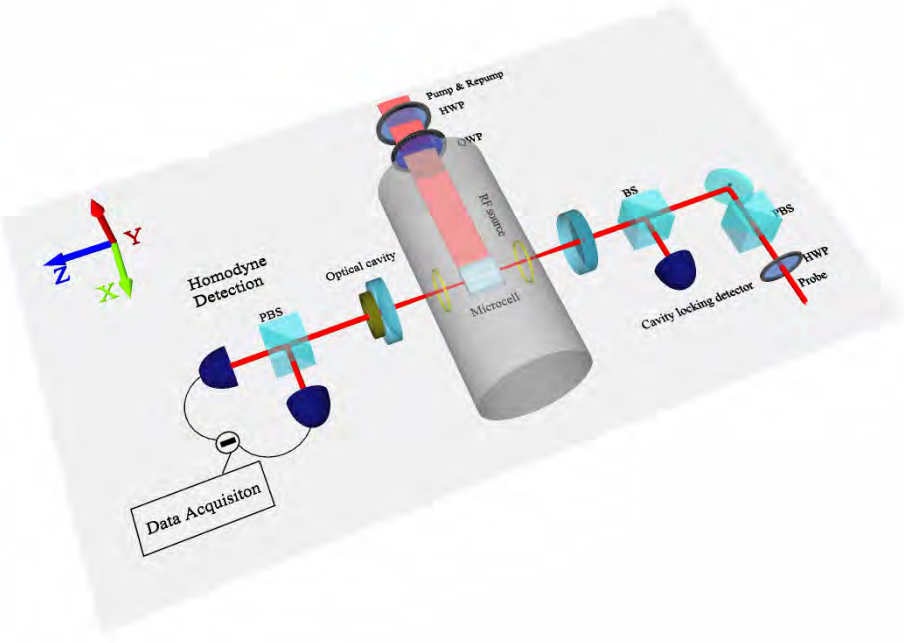

Fig. 3.1 Main scheme of the experimental setup.

are Faraday angle and magneto optical resonance (MORS) measurement, respectively. The

rather long part at the end of this chapter is devoted to the most critical measurement called quantum noise reconstruction in which measurement method including the calibration also, and the noise contributions from different sources are explained by relating to the theoretical formula given in previous chapter.

3.1 Laser system

As shown in Figure 3.1, there are totally three laser beams with different optical wavelengths composing the laser system in our setup, probe, pump and repump light beams, and the corresponding laser frequencies are given in Figure 3.2. Pump and repump beams are required to prepare the highly orientated spin state as the optical pumping, and the probe light is the beam interacting with atomic ensembles described in previous chapter.

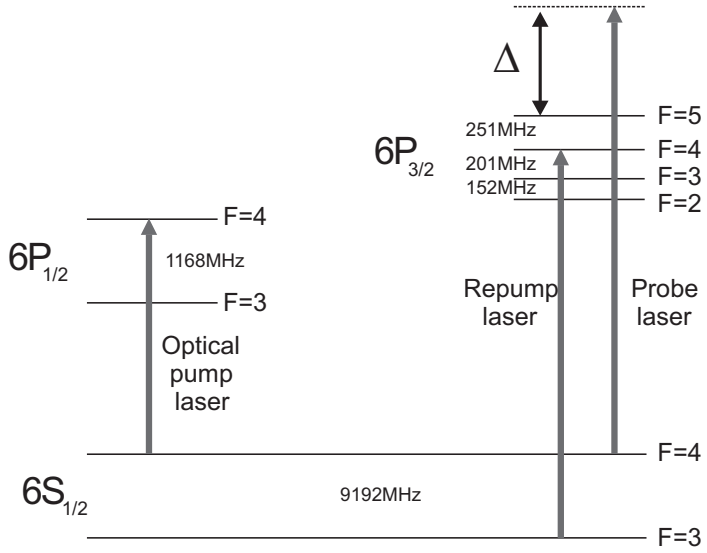

Fig. 3.2 Level scheme of Cesium and the laser frequencies of probe and optical pumping beams.

3.1.1 Probe light

The laser beam from distributed feedback laser TOPTICA DL100 is used as the probe light. Experimentally, the output of the laser is split into two beams after passing through the optical isolator, which is used to avoid the potential damage caused by backreflection. One of them is used as the main probe beam for the experiment and the other weaker fraction is for the laser frequency locking. Since we plan to have a large detuning with respect to the D2 transition, a fiber coupled electro optical modulator (EOM) is utilized to generate the

upper and lower sidebands at around 1GHz from the carrier frequency. Actually, in order to achieve the QND picture, typically we use the probe light with a blue detuning around 1.6GHz with respect to $6S_{1/2}F = 4 \rightarrow 6P_{3/2}F' = 5$ by locking the laser frequency to the second blue sideband, which means the relative large modulation depth is required. The line reflection alignment of the saturation absorption spectroscopy is followed to lock the blue or red sideband to an atomic transition. As shown in the right of Figure 3.3, the p-polarized light beam passes through the polarization beam splitter (PBS), Cs vapor cell, the optical attenuator and the quarter wave plate, and then is reflected by a 0° high reflection mirror. Because of the use of the quarter wave plate, the reflected weak signal beam with s-polarization carrying the absorption information is reflected by the PBS, and then hits the locking detector which provides the error signal for the electronic feedback. Usually, we run

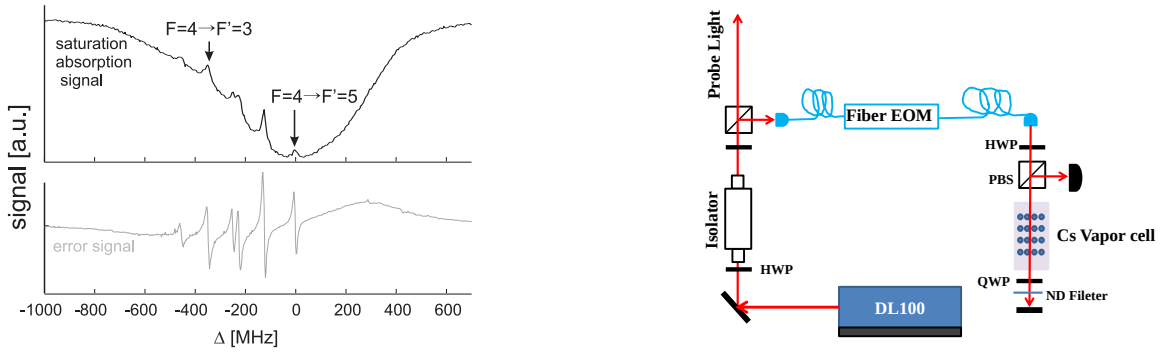

Fig. 3.3 Saturation absorption spectroscopy signal of probe light which corresponds to Cs D2 transition line and the experimental scheme of laser frequency locking system with the detuning of $\sim$ 1GHz. The black line is the saturation absorption signal and the gray one shows the error signal for the laser frequency locking.

the experiments in the pulse regime where the temporal profile of the laser beams is generated by means of intensity modulation. For the probe beam an EOM positioned between two PBSs is used as the intensity modulator to create the laser pulse with the duration of order of several millisecond. By using EOM instead of acoustic optical modulator (AOM), the sharp edges of the pulses including the high frequency components can be prevented. However, when running the experiment in the scheme of stroboscopic modulation, the intensity of the probe beam is modulated by AOM at twice the Larmor frequency $\sim$ 380kHz with the duty cycle around 15% due to its faster response as an optical switch.

3.1.2 Optical pumping

To prepare the highly oriented spin states, optical pumping is usually required[54]. Here the optical pumping is implemented by sending two circular polarized laser beams to the vapor cell. The pump laser at 894nm with the frequency corresponding to the Cs D1 transition $6S_{1/2}F = 4 \rightarrow 6P_{1/2}F' = 4$ comes from diode laser DL100 Pro which behaves very well in terms of frequency stability and shows low frequency noise. And the repump laser at 852nm is a homebuild Littrow configuration diode laser and grating stabilized to the Cs D2 transition $6S_{1/2}F = 3 \rightarrow 6P_{3/2}F' = 4$. The pump and repump laser beam overlapping with each other share the same propagation direction, parallel to the applied DC magnetic filed direction, and the same circular polarization σ_+ or σ_- as shown in Figure 3.1. The polarization direction of the optical pumping beams partially determines the final population of atoms. If choosing σ_+ polarized beams, the atoms will be populated at $F = 4, m_F = 4$ after the optical pumping. Otherwise, the atoms will be populated at $F = 4, m_F = -4$. The former is explained in Figure 3.4. For the σ_+ pump laser $F = 4, m_F = 4$ is a dark state, and the atoms in other Zeeman sublevels of ground state $6S_{1/2}F = 4$ absorb the σ_+ polarized pump photons and decay towards to $F = 4$ or $F = 3$. Due to the fact that σ_+ leads to $\Delta m_F = +1$ transition, finally the atoms still staying in the ground state of $F = 4$ will be populated into $F = 4, m_F = +4$. At the same time, the repump laser collects the atoms decaying to $F = 3$ and drives them back to $F = 4$. Following this logic we can see that the

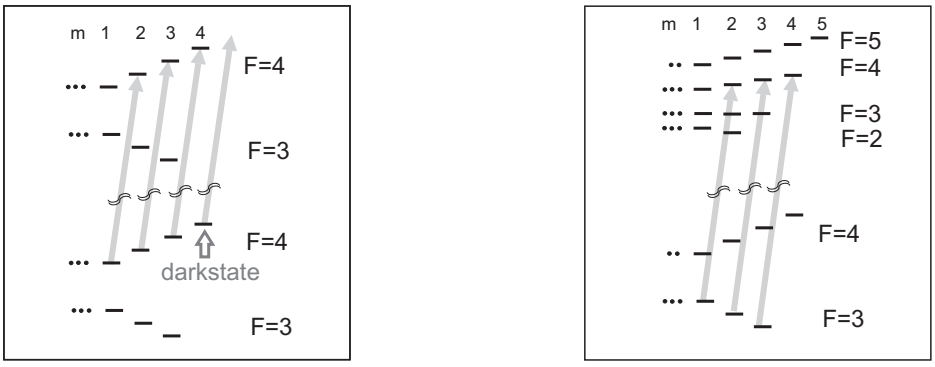

(a) (b)

Fig. 3.4 The atomic transitions induced by the σ_+ polarized pump (a) and repump (b) light beam, respectively.

atoms are fully populated into $F = 4, m_F = 4$ after an effective optical pumping process. Notice that since the repump laser is far off resonance to all transitions from the ground state $F = 4$, the broadening effect from it is negligible. In the experiment the intensity of repump beam can be set strong enough to make sure almost all the atoms go back to the ground state $F = 4$.

3.2 Microcell

In this section I will describe the key element of the whole thesis, micro-fabricated Cs vapor cell (microcell) which has experienced at least 3 times evolution on the fabrication. The current generation of microcell can provide the traverse spin lifetime (T_2 time) around 9ms, and the number of atoms about $10^7 \sim 10^8$ in a glass cell microchannel with the dimension of (300μm $\times$ 300μm $\times$ 10mm) depending on the environmental temperature. However, currently the light intensity transition through the microcell is not as good as we had expected which limits the degree of spin squeezing and single photon generation efficiency, which can be found in Chapter 5 and reference [53], respectively. At present we are struggling to reduce the optical losses by using CO_2 laser bonding between bare glass chip and windows with anti-reflection coating; the local heating can help us to avoid the damage on the coating surface.

3.2.1 Fabrication

The first generation of our microcell-chip was designed and fabricated by QUANTOP at Niels Bohr Institute and by Danchip at Danmarks Tekniske Universitet. Photos of cells are

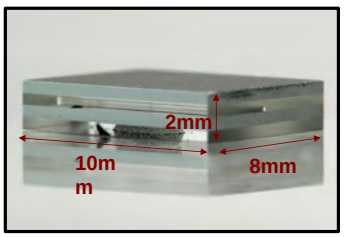

(a) 4-layers glass-silicon chip.

(b) Microcell sealed inside glass container.

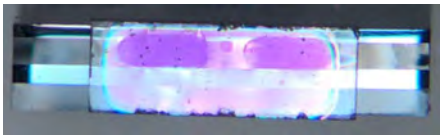

(c) laser bonding of windows.

Fig. 3.5 Photos of the first generation Cs vapor microcell.

shown in Figure 3.5. A chip is made of 4 layers of glass and silicon joined together through anodic bonding, and the microchannel with a $200\mu m \times 200\mu m$ cross section was developed on the middle glass layer by Micro saw. More complicated procedure was implemented

when fabricating the holes in the silicon layer with the size of $20 \sim 54\mu m$ for the injection of atomic vapor gas and anti-relaxation coating material. Details can be found in Appendix 2. Since two different materials were used to form the cell-chip, laser bonding between the chip and windows with anti-reflection coating layer did not work (see Figure 3.5(c)). Therefore, we decided to replace this 4-layer cell-chip with a single piece of glass chip.

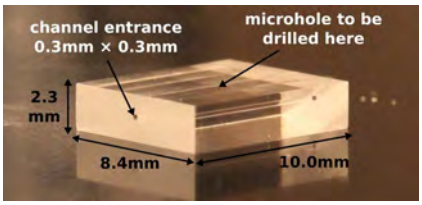

(a) Bare chip (no windows) with microchannel.

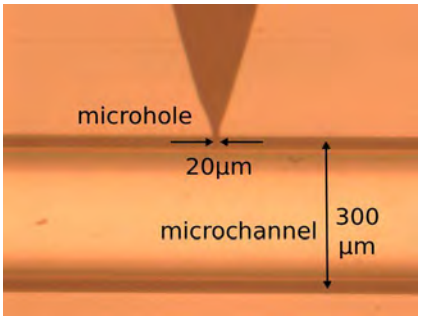

(b) Closeup of microchannel and laser-drilled microhole.

(c) Finished microcell with windows.

Fig. 3.6 Photos of the current Cs vapor microcell.

The current version of mircocell is shown in Figure 3.6, where microcell-chip is based on the borosilicate glass slab from VitroCom containing a microchannel with the cross-section of $300\mu m \times 300\mu m$. A microhole ($\sim 20\mu m$) is laser drilled on one of the microcell's surfaces to allow atoms to enter, and the surfaces of the glass chip are super-polished in order to avoid any air gaps. Although the current microcell is encapsulated in a cylinder glass container where the windows are attached by mechanical pressure, we are developing the glass-to-glass laser-bonding procedure in our lab to attach windows at the edges of the cell, and attach a round tube to the cell's top surface where the micro-hole sits. Note that in the fabrication of the current microcells the annealing procedure at 550° for the whole glass structure is implemented to remove stresses that the fusing process may have caused.

As mentioned at the end of previous chapter, since thermal atoms confined in a container will lose their spin orientation information after colliding with the bare glass walls, the anti-relaxation coating, Alkene C20, is deposited on the inner surface of the microcells by Misha Balabas, an coating expert from S. I. Vavilov State Optical Institute in Russia. In the first generation of microcell based on 4-layer silicon-glass chips, the typical spin depop-

ulation time T1 (also called longitude spin decoherence time) is $1 \sim 2$ms, corresponding to ~ 3000 times of bounces which is lower than the value we expected according to the

Cell No.	1	2	3	4	5	6
Volume[μl]	60	18	24	26	13	80
Radius[cm]	0.24	0.16	0.179	0.184	0.146	0.267
T1[ms]	200	54	95	75	60	80
Nb[$\times 10^3$]	13.3	5.4	8.6	6.6	6.6	4.8

Table 3.1 Number of bounce with 140° Alkene C20 coating.

coating performance on the macro-spherical vapor cells. When we switched to the current type of microcell based on the chip of borosilicate glass where the smooth channel surface is better for alkene coating deposition, we spent some time on investigating the coating condition. We made two batches of spherical vapor cells with different coating deposition temperatures (140° and 280°) since we thought the typical coating temperature (140°) was not sufficient to form the even distribution and thick enough coating layer. The corresponding results are shown in Table 3.1 and Table 3.2, and it is proved that the higher coating deposition temperature can really improve the coating quality. By looking into Table 3.2 where six spherical vapor cells with different sizes were involved in the test, it is found that

Cell No.	1	2	3	4	5	6
Volume[μl]	12	28	62	500	1800	4200
Radius[cm]	0.14	0.19	0.25	0.5	0.75	1
T1[ms]	110	207	336	220	1093	1382
Nb[$\times 10^3$]	12.64	17.77	22.33	7.230	23.48	22.33

Table 3.2 Number of bounce with 280° Alkene C20 coating.

the number of bounce keeps increasing when the size is very small, then achieves a constant value $\sim 2.3 \times 10^4$ except the abnormal one No.4. This can be explained in the following way. There are two different main mechanisms limiting the spin lifetime of atoms inside of the cell, one is from wall collision and the other is the leakage of the atoms from any holes which is determined by the ratio of hole size to the volume of the entire cell. All the cells almost have the gaps with the same size, thus it is very obvious when the leakage contribution is comparable to the wall collision contribution (in other words, the volume is quite small). This coating temperature then was used to fabricate the current microcells and resulted in a much better performance than before, the dark T_1 time is of ~ 17ms and dark T_2 time ~ 9ms. The measurement procedure for T_1 and T_2 is described in Section 3.2.2 and 3.2.3 below.

The main limitation for the current microcell is the light power transmission, which is $\sim 90\%$ now even if the good anti-reflection coated windows are attached, which poses some limitations for our experiments that will be discussed later. It could be from the coating damage when the pressure is applied to attach the windows, therefore, we are running the laser bonding procedure to attach the windows at the edges of the cell, and attach a round tube to the cell's top surface where the micro-hole is drilled.

3.2.2 Faraday angle

Faraday rotation measurement is one of the important test to characterize the quality of the vapor cells, which can determine the collective spin component in light propagation direction, and if the atomic ensemble is highly polarized the atomic density can be deduced for this measurement. Additionally, the evolution of Faraday angle can tell us the spin depolarization time due to the fact of

$$\theta_F(t) = -\frac{\Gamma\lambda^2 \langle J_x \rangle (t) \cdot a_1(\Delta)}{16A\Delta 2\pi} \tag{3.1}$$

where $\lambda = 852\text{nm}$ and $\Gamma = 2\pi \cdot 5.21\text{MHz}$ are the wavelength of the probe light and the full width at half maximum (FWHM) linewidth of the excited state, respectively, while $\langle J_x \rangle (t) = \langle J_x \rangle (0) e^{-t/T_1}$. For this measurement we are probing in the x-direction. We assume a fully oriented sample here, which means in the experiment one should make sure that the optical pumping is effective by checking the polarization and light intensity of pump and repump beams to maximize the Faraday angle appearing directly in the oscilloscope, then one can get the initial Faraday angle value as follow

$$\theta_F \approx -\frac{\Gamma\lambda^2 4 N_a a_1}{16A\Delta 2\pi} \approx -\frac{\Gamma\lambda^2 4 \rho a_1 L}{16\Delta 2\pi} \tag{3.2}$$

where ρ is the atomic density, while A and L are the area and length of the cell, respectively. It is found in Equation 3.2 that the Faraday angle is only proportional to the sample length with a given atomic density. Therefore, we send all three beams in the same direction parallel to the bias DC magnetic field, as shown in Figure 3.7. For the data presented in this section, beam pulses were created with a chopper and shutter. The pulse sequence was $\sim 50\text{ms}$ of combined pump/repump beam, followed by $\sim 50\text{ms}$ of probe beam. The static magnetic field was produced using a small ring magnet placed next to the microcell. We have since replaced the chopper with AOMs to create cleaner pulses. In addition, we have removed the magnet and instead installed a 3-layer μ metal shield containing DC coils around the microcell to generated a more homogenous bias magnetic field. Depending

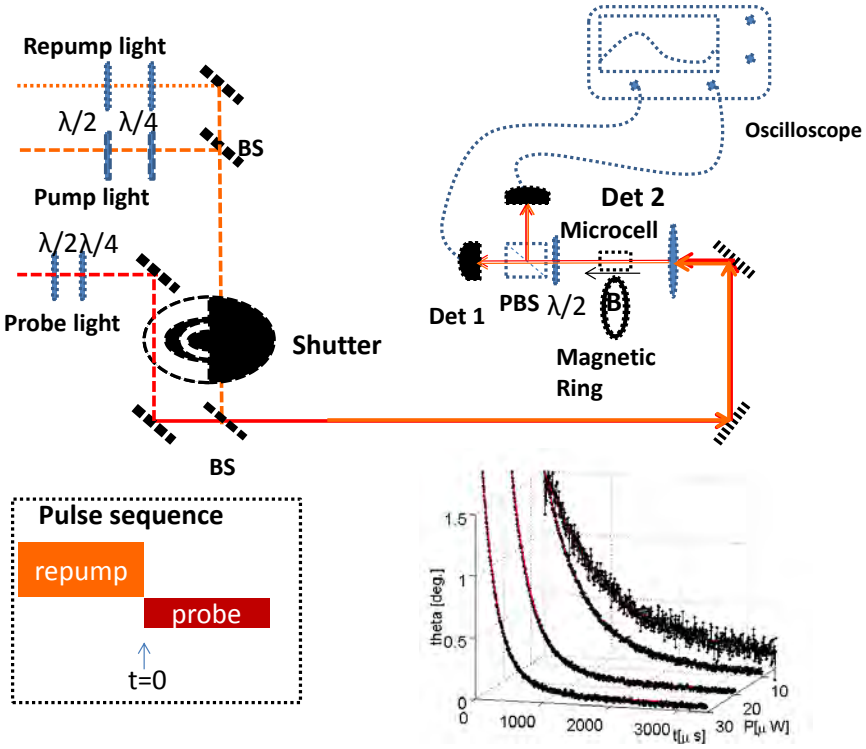

Fig. 3.7 Faraday rotation measurement.

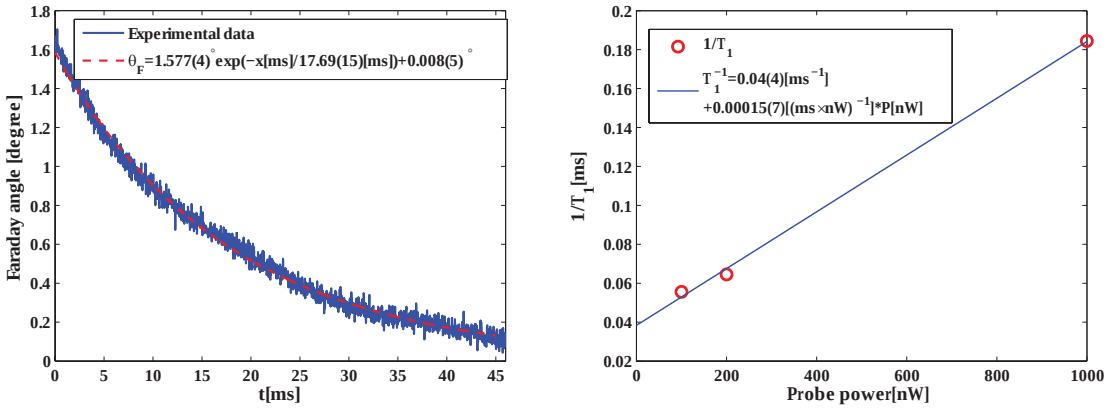

(a) (b)

Fig. 3.8 Results of Faraday rotation with $\Delta = 850$MHz. (a) shows the Faraday rotation evolution during the probing process, and (b) presents the values of $\frac{1}{T_1}$ with different probe power where the dark T_1 time can be extrapolated from the linear fitting.

on the room temperature the Faraday angle varies between 1.5° and 2.4°, and the average number of atoms is $\sim 10^7$ (see Figure 3.8).

3.2.3 T_1 and T_2

In general, we use two different decay constants to characterize the coherence of collective spin, T_1 and T_2. T_1 is the decay of classical mean value J_x in our experiment, and called spin depolarization time describing the reduction of vector length. Population transfer into $F = 3$ whose contribution to the Faraday rotation is negligible, and population also transfer into other magnetic sublevels $F = 4, m_F = 3, 2$ whose Faraday rotation contributions are reduced in a factor of $3/4$ and $1/2$, cause the decay of J_x when starting from the fully oriented state. Although Faraday rotation measurement has been used to measure the atomic density and also T_1 time as explained in last section, here I will introduce another method to characterize this T_1 time again which is more convenient once the microcell is coupled into the optical cavity and well aligned. The experimental setup is shown in Figure 3.1, and the corresponding pulse sequence is shown in Figure 3.9(a). The optical pumping polarizes

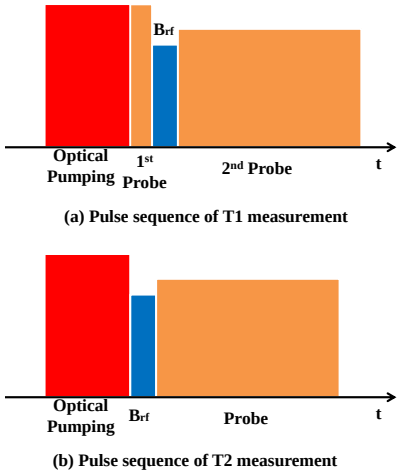

Fig. 3.9 Experimental pulse sequence for T_1 and T_2 measurement. The durations of optical pumping and RF pulses are 5ms and 200μs, respectively.

almost all the atoms into $F = 4, m_F = 4$ initially with the spin orientation above 98% (the corresponding characterization will be discussed later.). When the probe light is switched on, the decay of $\langle J_x \rangle$ gets faster than the decay in the dark due to spontaneous emission from the probe. Then a RF pulse that creates an excitation of $\Delta m_F = 1$ when the frequency is on resonance with Larmor frequency Ω_L is followed by the second probe pulse to measure that spin response which is proportional to the mean value of J_x[55]. Given a fixed probe power,

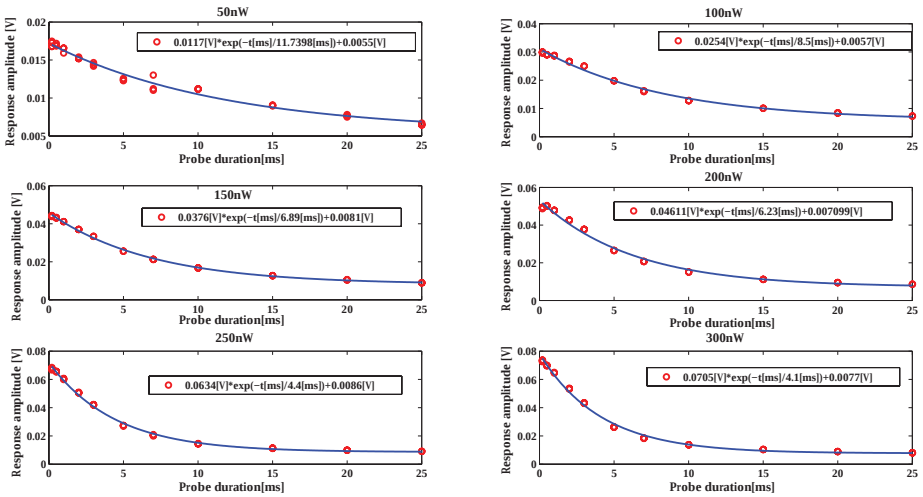

Fig. 3.10 T_1 measurement for different probe power with blue detuning at $\Delta = 975$MHz.

by changing the duration of the first probe pulse and recording the beginning of the spin response in the second probe pulse, one can get the full information of the evolution of $\langle J_x \rangle$,

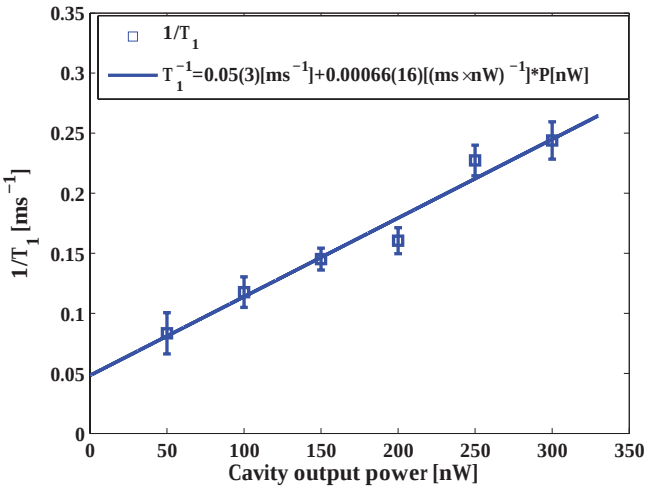

Fig. 3.11 T_1 time for different probe power with blue detuning at $\Delta = 975$MHz.

and furthermore can extract the T_1 time at this probe power by the exponential fitting of these data points. Collecting several T_1 values at different probe powers and linearly fitting their reciprocals, one can extrapolate T_1 value in the dark as presented in Figure 3.10 and Figure 3.11.

T_2 is the decay constant to describe the decoherence of transverse spin, and usually can be measured by recording the decay of the mean value in the rotating transversal spins as $\langle J_\perp \rangle (t) = \langle J_\perp^0 \rangle e^{-t/T_2}$. As discussed in[35, 56], the decay rate $\Gamma = (\pi T_2)^{-1}$ can be expressed

as follow,

$$\Gamma = a + b \cdot \theta_F + c \cdot P + d \cdot P^2 + e \cdot (\theta_F P). \tag{3.3}$$

The combination of the first two terms contributes to the decay rate in the dark, where

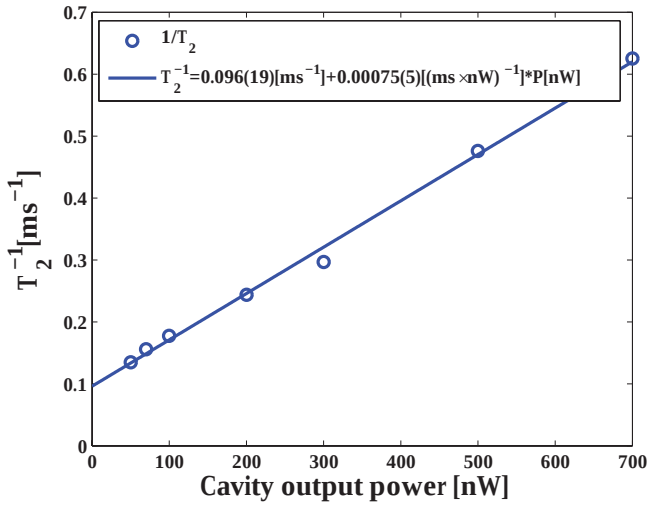

Fig. 3.12 $1/T_2$ for different probe powers with blue detuning $\Delta = 1.598$GHz. T_2 time in the dark can be extrapolated from the linear fitting which gives the value of about 10ms.

the constant a is from the wall collisions, losses due to atom leaving the effective cell volume to other part (e.g. the stem), and the magnetic field instabilities and inhomogeneity. The second term proportional to atom number $\theta_F \propto N_a$ comes mainly from the collisions between atoms. The spontaneous emission induced by the probe light is embodied in the term involving probe power P only, while the quadratic part in probe power probably results from the inhomogeneous intensity distribution of the light which causes atoms to experience different Stark shifts in different regions of the cell. The last term in Equation 3.3 is related to the higher order coherent interaction between light and atoms, and is called γ_{swap} in Equation 2.38 in order to be distinguished from the incoherent decay. In the experiment for T_2 estimation, we keep the setup as in Figure 3.1 but with a different pulse sequence from T1 measurement that is shown in Figure 3.9(b). Since we mainly concentrate on the QND picture in the work of this thesis, probe light with the blue detuning of $\Delta = 1.598$GHz is used to measure the T_2 time where the effect from the tensor interaction is very small and can be neglected according to Figure 2.17. The corresponding result is presented in Figure 3.12.

3.3 Optical cavity

Optical cavity is one of the widely used elements in physical research, which can enhance the interaction between light and matter[57, 58, 59], modify the spatial and spectral modes of light fields[60], provide phase feedback[61, 62]. In our setup shown in Figure 3.1, the optical depth in the atomic ensemble is enhanced by coupling the microcell into the fundamental mode of a standing wave cavity. This section is devoted to the general description of optical resonator and the related technologies. Let us consider a simple model of standing wave cavity with input and output concave mirrors M1 and M2. The corresponding curvatures are r_1 and r_2, respectively. In our experiment, because of the large diameter of magnetic shield a near concentric cavity is built with the curvature of $r_1 = r_2 = 110$mm. By using the method of equivalent confocal cavity[63], we can derive the formula about beam waist and beam size w_0 at the end mirrors $w_{1,2}$ as follow,

$$\begin{aligned} w_0 &= \sqrt{\frac{f\lambda}{\pi}}, \\ f^2 &= \frac{L(r-L)(r-L)(r+r-L)}{((L-R)+(L-R))^2}, \\ w_1 = w_2 &= \sqrt{\frac{\lambda L}{\pi}}\left(\frac{r^2\times(r-L)}{L(r-L)(r+r-L)}\right)^{1/4}, \end{aligned} \tag{3.4}$$

where f is the equivalent focal length. Figure 3.13 shows the dependence of these parameters on cavity length in our setup. At present we choose the cavity length as 218mm with

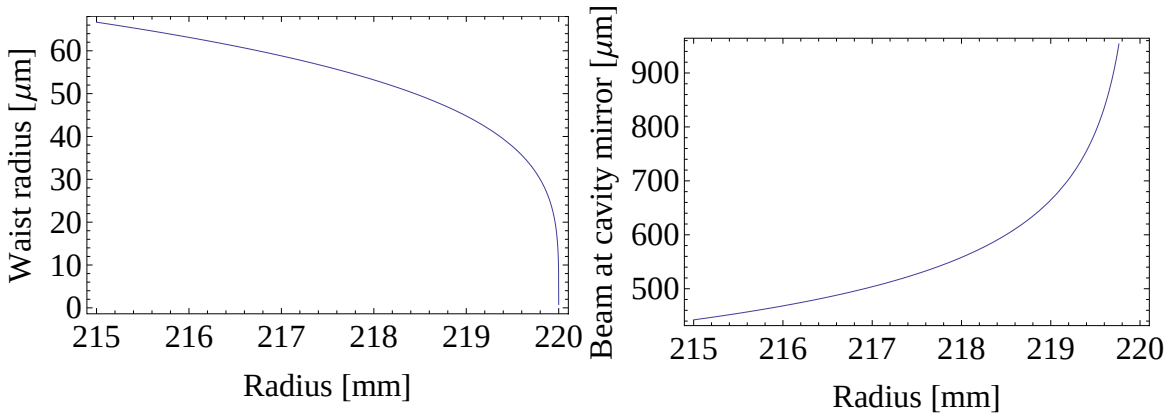

Fig. 3.13 Dependence of beam size on the cavity length. (a) shows the beam waist radius at different cavity length, and (b) shows the beam diameters on the end mirrors.

the beam waist of 110μm in diameter which is an optimal value for the interaction, a good

compromise between low clipping losses and good filling factor. And also with the consideration that the cavity mirrors are set out of the cylindrical magnetic shield whose diameter is 190mm.

Let us look at the cavity properties in the frequency domain. Given the intensity reflectivity of input and output mirrors as R_1 and R_2, and the round trip intracavity loss as l_{cav}, one can derive the formula for the finesse $\mathfrak{F}$ as follow[64],

$$\mathfrak{F} = \frac{\nu_{free}}{\Delta\nu} = \frac{\pi\sqrt{g_m}}{1-g_m}, (g_m = \sqrt{R_1 \cdot R_2(1-l_{cav})}) \tag{3.5}$$

where ν_{free} is the free spectral range (FSR) and $\Delta\nu$ is the cavity bandwidth, while g_m gives the amplitude reduction of the internal field during each round trip. If we introduce the phase difference for each trip as $\delta\phi = 2\pi(\nu_L - \nu_{cav}) \cdot 2L/c$ with the laser frequency ν_L and the eigenfrequency of cavity mode ν_{cav}, the total effect of cavity during one round trip can be described by $g(\nu) = g_m e^{-i\delta\phi}$. Therefore, the power spectrum of transmitted light and reflected light can be obtained as

$$\begin{aligned} P_{out} &= \frac{(1-R_1)(1-R_2)\,|g(\nu)|}{\sqrt{R_1 R_2}\,|1-g(\nu)|^2} P_{in}, \\ P_{ref} &= \frac{|R_1 - g(\nu)|^2}{R_1\,|1-g(\nu)|} P_{in} \end{aligned} \tag{3.6}$$

In Figure 3.14, the calculated power spectrums of both transmitted and reflected light are given under the experimental condition of $R_1 = 99.7\%$ and $R_2 = 80\%$ with the round trip loss of 13.3%, and the reason of choosing those values will be explained in Chapter 5 about conditional spin squeezing.

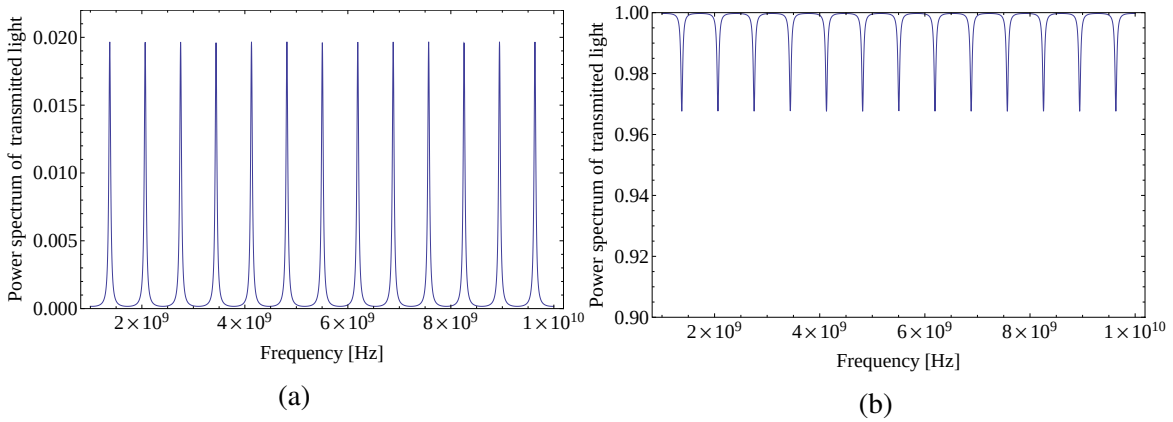

Fig. 3.14 Calculated power spectrum of transmitted(a) and reflected(b) light that have been normalized to the input power.

Experimentally, the optical cavity is frequency locked on resonance by a Pound-Drever-Hall technique[65]. Instead of the MHz phase modulation on the input light field, a 10kHz modulation is applied on the piezoelectric transducer (PIZZOMECHANIK GmbH)since the broad bandwidth of the cavity (about 40MHz) makes the phase modulation difficult. And details of frequency locking technology can be found in Appendix3.

3.4 Preparation and characterization of the atomic state

As mentioned above, optical pumping is employed to create the highly oriented spin states which is quite important in the interface between light and atoms. The circular polarized pump and repump beams, corresponding to Cs D1 and D2 transitions respectively, are sent to the vapor cell parallel to the DC magnetic field which creates the Zeeman splitting as the quantization axis. In order to verify the atomic CSS state, an RF magnetic field is employed to excite the coherent transition between different magnetic sublevels that can be read out by the probe light. This is called magneto optical resonance signal (MORS).

3.4.1 Magneto optical resonance

The MORS experiment can be run in frequency or time domain which shares the same setup as Figure 3.1. In this section I only shows the experiment in the time domain where the linewidth broadening from the pump beam is avoided. And MORS experiment in frequency domain can be found in[31, 34, 35]. The interaction of atoms with a magnetic field is described by the Hamiltonian which has been used in Chapter 2 when deriving the input-output formula in rotating frame

$$\hat{H}_{mag} = g_F \mu_F \mathbf{J} \cdot \mathbf{B} + O(B^2), \tag{3.7}$$

where μ_{B} is the total angular momentum of the atom. Notice that the second term in Equation 3.7 describes the higher order effect from the magnetic field which behaves approximately as the quadratic Zeeman frequency difference between $\hat{\sigma}_{m,m+1}$ and $\hat{\sigma}_{m-1,m}$ as $\nu_{qz} \approx \frac{2\Omega_L}{\nu_{hfs}}$ with the hyperfine splitting of the Cesium ground state $\nu_{hfs} = 9.1926$GHz. In the experiment, a DC bias magnetic field B_x induces the Larmor procession at $\Omega_L = g_F \mu_F B_x/\hbar$, and also the quadratic Zeeman splitting. Additionally, if an RF magnetic field at frequency Ω along the z-direction is added, the transverse spin components in the rotating frame can

be written as

$$\frac{\partial \hat{J}'_y}{\partial t} = -\omega_c \cos(\Omega_L t)\cos(\Omega t + \phi)J_x, \quad \frac{\partial \hat{J}'_z}{\partial t} = -\omega_s \sin(\Omega_L t)\sin(\Omega t + \phi)J_x, \tag{3.8}$$

with the Rabi frequency $\omega_{c,s} = g_F \mu_F B_{c,s}/\hbar$ where $B_{c,s}$ is the amplitude of the RF cosine and sine components. When the RF magnetic field is on resonance so that $\Omega = \Omega_L$ and setting $\phi = 0$, the above formula with the assumption of long interaction time $\omega_c T, \omega_s T \ll 1 \ll \Omega T$ can be rewritten as

$$\frac{\partial \hat{J}'_y}{\partial t} = -\frac{\omega_c J_x}{2}, \quad \frac{\partial \hat{J}'_z}{\partial t} = -\frac{\omega_s J_x}{2}. \tag{3.9}$$

Hence, a displacement in the rotating frame is created by the resonant RF magnetic field which represents an excitation of all $\Delta m = 1$ coherence and can be mapped onto the probe light through the interaction between light and atoms. By using Equation 2.25 and 2.33 we can get the MORS signal in frequency domain as

$$\begin{aligned} MORS(\Omega) &= \sqrt{\langle x_c^{out}\rangle^2 + \langle x_s^{out}\rangle^2} \\ &\propto \left| N_a \sum_{m=F}^{F-1} \frac{F(F+1) - m(m+1)}{i(\Omega_{m+1,m} - \Omega) - \Gamma_{m+1,m}/2} \left\langle \hat{\sigma}_{m+1,m+1} - \hat{\sigma}_{m,m} \right\rangle \right|, \end{aligned} \tag{3.10}$$

where $\Gamma_{m+1,m}$ are the FWHM linewidths of each coherence and $\Omega_{m+1,m}$ are the individual coherence evolution frequencies, while the measured light components $\left\langle x_{c,s}^{out} \right\rangle \propto \left\langle J_{y,z}^{in} \right\rangle$. This formula is the Fourier transformation of MORS signal in time domain

$$MORS(t) \propto \left| N_a \sum_{m=F}^{F-1} [F(F+1) - m(m+1)] e^{i\Omega_{m+1,m}t} e^{-\Gamma_{m+1,m}t/2} \left\langle \hat{\sigma}_{m+1,m+1} - \hat{\sigma}_{m,m} \right\rangle \right|. \tag{3.11}$$

Experimentally, a Larmor precession at frequency $\Omega = 698$kHz is induced by the DC bias magnetic field ($\sim$ 2Gauss), and the corresponding quadratic Zeeman splitting is 105Hz which allows us to resolve all the eight Lorentzian peaks with the weak probe beam. The pulse sequence is same as that in T_2 measurement, and a 100ms weak probe light pulse is used to guarantee the sufficient frequency resolution. Figure 3.15 and 3.16, show the partial and highly polarized MORS signals, respectively, where only repump light is employed in the former case and the complete optical pumping is used in the latter case. Note that the left graphs of these two figures present the detected signal in time domain where the beating comes from the coherent excitations in different magnetic sublevels. And the spin

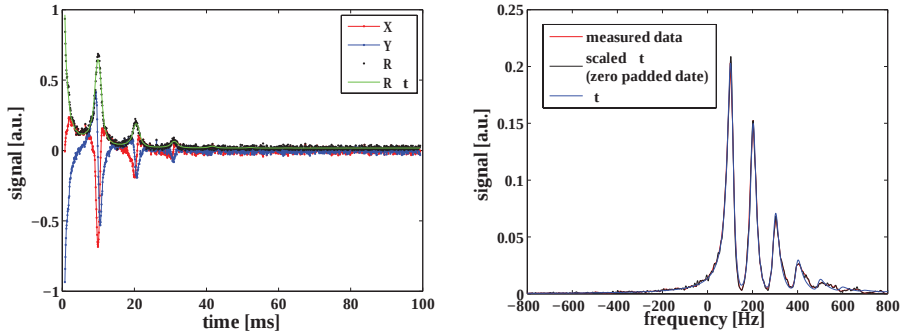

(a) (b)

Fig. 3.15 Pulsed MORS signal for an optical pumping cycle resulting in the 76% spin orientation when only the repump light is on.

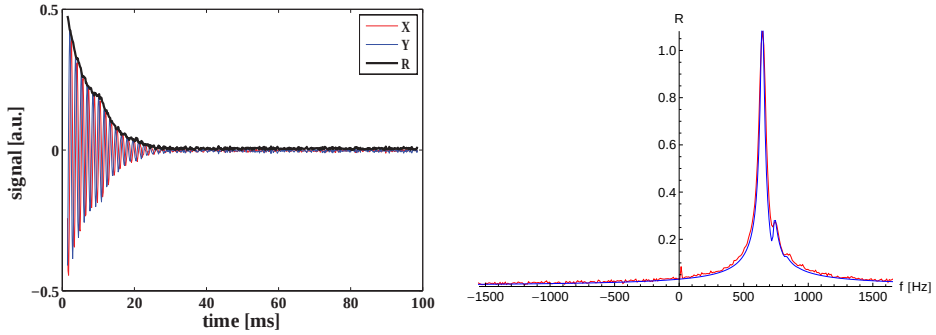

(a)

(b)

Fig. 3.16 Pulsed MORS signal for an optical pumping cycle resulting in the 98.5% spin orientation when both pump and repump light are on.

orientation is defined as

$$p_{F=4} = \frac{1}{4}\sum_{m=-4}^{4} m\hat{\sigma}_{m,m} \tag{3.12}$$

In general, the splitting between the peaks is determined by not only the quadratic Zeeman shift ν_{qz} but also quadratic Stark shift ν_{qs} which is given by[31]

$$\begin{aligned}\nu_{qs}[\mathrm{Hz}] &= -\frac{\Gamma\lambda^2 a_2(\Delta)}{16\pi^2 A\Delta}\Phi(t)[1+3\cos(2\alpha)] \\ &= 1.03\times 10^6\mathrm{Hz}\frac{P[\mathrm{mW}]a_2(\Delta)}{A[\mathrm{cm}^2]\Delta_{blue}(\mathrm{MHz})}[1+3\cos(2\alpha)],\end{aligned} \tag{3.13}$$

where α is the angle between the macroscopic spin direction (the x-axis) and the probe polarization direction. As shown in Equation 3.13, the quadratic Stark shift is related to the

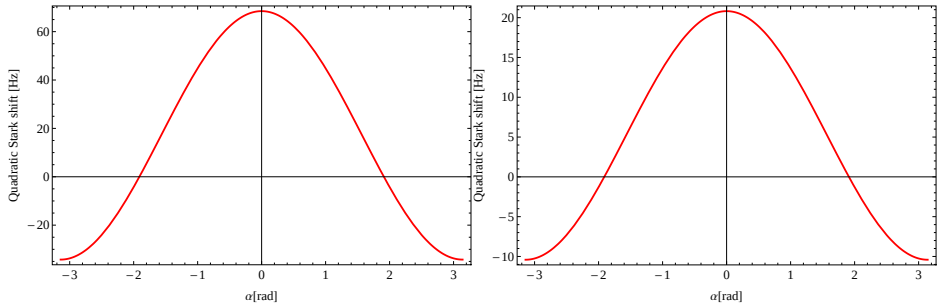

(a) $\Delta_{blue} = 850$MHz. (b) $\Delta_{blue} = 1.6$GHz.

Fig. 3.17 Quadratic Stark shifts for different polarization direction of probe light.

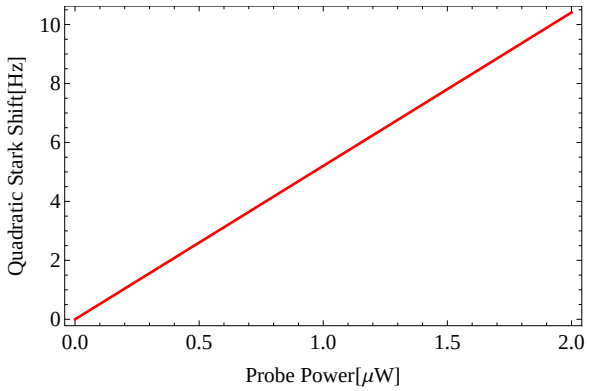

Fig. 3.18 Quadratic Stark shift for different probe power with blue detuning $\Delta = 1.6$GHz and y-direction linear polarization.

laser detuning ,polarization direction and intensity of the probe light. Figure 3.17 shows the shift evolution with different polarization direction at $\Delta_{\mathrm{blue}} = 850$MHz and $\Delta_{\mathrm{blue}} = 1.6$GHz.

Figure 3.18 gives the quadratic Stark shift for different probe powers at $\Delta_{\text{blue}} = 1.6\text{GHz}$. Since in the MORS experiment we use the probe beam with the intracavity power of $0.5\mu W$ and the detuning is $\Delta_{\text{blue}} = 1.6\text{GHz}$, this effect is negligible and the quadratic Zeeman effect is the dominant contribution to the splitting of the peaks.

3.5 Coupling strength

In this section I will introduce one of the key parameters in our experiment, the coupling strength κ. In the QND scenario mentioned in Chapter 2, this dimensionless constant can be represented as $\kappa^2 = a^2 \cdot S_x J_x T \propto N_a N_{ph}$ where N_a and N_{ph} are the number of atoms and photons respectively. Although only QND interaction is discussed in this thesis, the definitions for different scenarios can be found in[35]. There are two typical methods being used to find this constant, one is to transfer a known displacement of coherent light state to the atoms and then read out this coherent displacement of the atomic state[32], and the other method relies on the noise measurement of thermal atomic state[35]. The former called mean value transfer is quite useful, especially when calibrating the coupling strength in the non-QND picture where swapping interaction is included, but in the following I am focusing on the latter one.

Atomic spins in thermal equilibrium, that is the unpolarized spin state, are not affected by the higher order interaction. In the thermal state, it is fully symmetric which means $\hat{j}_x^2 = \hat{j}_y^2 = \hat{j}_z^2 = \frac{F(F+1)}{3} = \frac{20}{3}$. In this setting all atomic sublevels have the same population; the same gose for atoms in $F = 3$ manifold which are not observed in the measurement. Since there are 16 sublevels totally and 9 of which belong to $F = 4$, the observed spin noise will thus be $N_a \frac{20}{3} \cdot \frac{9}{16} = \frac{15}{4} N_a$. This is a factor of $\frac{15}{8}$ comparing with the atomic noise in the CSS state which is $FN_a/2 = 2N_a$. Therefore, the observed spin noise in the thermal state should be $\frac{15}{8} \cdot Var(\hat{x}_A(\hat{p}_A))_{CSS}$. Since in the thermal spin state the mean value of vector j_x equals to zero which leads to the fact that the enhancement from J_x of coupling the light variables to the atomic spin variables is negligible, the backaction of light on itself disappears. By looking at Equation 2.25, the corresponding input-output relation in terms of Stokes vectors can be read as

$$\begin{aligned} \hat{S}^{out}_{y(c,s)} &= \hat{S}^{in}_{y(c,s)} + \frac{aS_xT}{2}\hat{J}_{z,y} \\ &= \hat{S}^{in}_{y(c,s)} + \frac{\kappa\sqrt{S_xT}}{2\sqrt{J}}\hat{J}_{z,y}, \end{aligned} \tag{3.14}$$

where $J = 4N_a$ for hyperfine level $F = 4$. In the derivation from the first line to the second

line I use the fact that $\kappa = a\sqrt{S_x JT}$ and in the CSS state $J_x = J = 4N_a$ as mentioned before. If calculating the noise of the measured light variable $\hat{S}_{y(c,s)}$, we can get

$$Var(\hat{S}^{out}_{y(c,s)}) = Var(\hat{S}^{in}_{y(c,s)}) + \frac{\kappa^2 S_x T}{4J} Var(\hat{J}_{z,y}). \tag{3.15}$$

Let us use some knowledge about light noise which I will show in the next section. Assuming the input light is in the coherent state (or called shot noise limited), the noise of $Var(\hat{S}^{in}_{y(c,s)})$ is defined as $Var(\hat{S}^{in}_{y(c,s)}) = \frac{S_x T}{2} = \frac{N_{ph}}{4}$. Thus, Equation 3.15 can be rewritten as

$$\begin{aligned} Var(\hat{S}^{out}_{y(c,s)})_{thermal} &= \frac{S_x T}{2}[1 + \frac{\kappa^2}{2} Var(\frac{\hat{J}_{z,y}}{\sqrt{J}})] \\ &= \frac{S_x T}{2}[1 + \frac{\kappa^2}{2}\frac{15}{8}]. \end{aligned} \tag{3.16}$$

Furthermore, the coupling constant can be derived from the measured light noise $Var(\hat{S}^{out}_{y(c,s)})$ as

$$\begin{aligned} \kappa^2 &= \frac{\frac{Var(\hat{S}^{out}_{y(c,s)})_{thermal}}{\frac{S_x T}{2}} - 1}{15/16} \\ &= \frac{\sigma^2_{thermalSN} - 1}{15/16}, \end{aligned} \tag{3.17}$$

where $\sigma^2_{thermalSN}$ means the measured noise of the output light has been normalized into

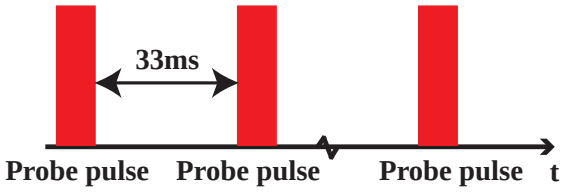

Fig. 3.19 Pulse sequence for the thermal noise measurement.

the shot noise unit. It is a good way to extract κ in the QND scenario from the noise measurement of atomic spins in the thermal equilibrium where laser detuning Δ_{blue} is much larger than the hyperfine splitting of the excited states so that the tensor interaction is significantly suppressed. However, when swap operation is included the coupling constant κ_{thermal} slightly differs from $\kappa = \sqrt{\frac{\gamma_s}{\gamma}}\frac{\sqrt{1-e^{-2\gamma T}}}{\zeta}$ involved in the real interaction. More details can be found in[35].

Figure 3.19 shows the pulse sequence for the thermal noise measurement where we choose the laser detuning as $\Delta_{\text{blue}} = 1.6$GHZ so that the role of tensor interaction can be neglected as discussed in Chapter 2. The time gap between two probe pulses is usually set to

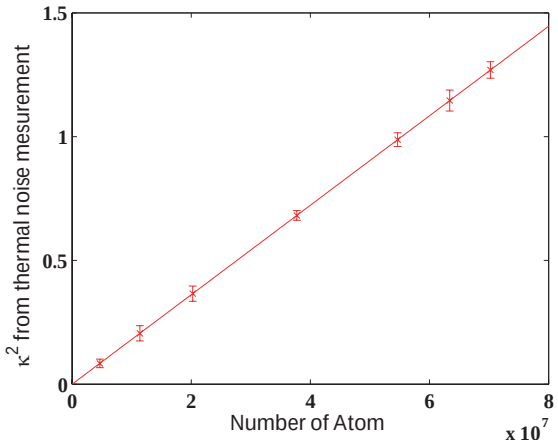

Fig. 3.20 κ^2 extracted from the thermal noise measurement for different numbers of atoms. Interaction time and laser detuning are 0.5ms and $\Delta_{\text{blue}} = 1.6$GHZ, respectively.

33ms to ensure the fully thermalization of atoms even if the probe beam has some pumping effect. Figure 3.20 and Figure 3.26(shown in next section) present the dependence of κ^2 on the number of atoms and photons, respectively. In order not to confuse the readers I should mention the way to change the number of atoms here. Previously, the number of atoms was changed by tuning the environment temperature inside the magnetic shield, however, the range is very limited, typically from $17°C$ to $30°C$ since only air heating process was employed but no cooling. In the procedure of measuring the data involved in Figure3.20, heating process is still kept but instead of air heating, a twisted wire with high resistance is wound around the aluminum cylinder where most of the magnetic coils are attached. By adding the current on this wire the stable environment temperature can be established inside the cylinder. We can decrease the number of atoms by weakening the repump beam but keeping the same intensity of pump beam to reduce the number of atoms in the $F = 4$. In this scheme, the number of atoms is calibrated against a response to a RF field.

3.6 Quantum noise

3.6.1 Light noise

Before describing the quantum noise measurement, I would like briefly to remind the readers about our detection system. Since the drive light or probe light is used as the strong local oscillator which shares the same phase as the generated quantum light and the polarization of the local oscillator light is orthogonal to that of the quantum beam as shown in Chapter 2, polarimetric measurement of light, also called polarization homodyne detection is employed

in our system which is in principle a typical balanced homodyne detection of light[64]. The corresponding schemes of $\hat{S}_y$ and $\hat{S}_z$ components are shown in Figure 3.21.

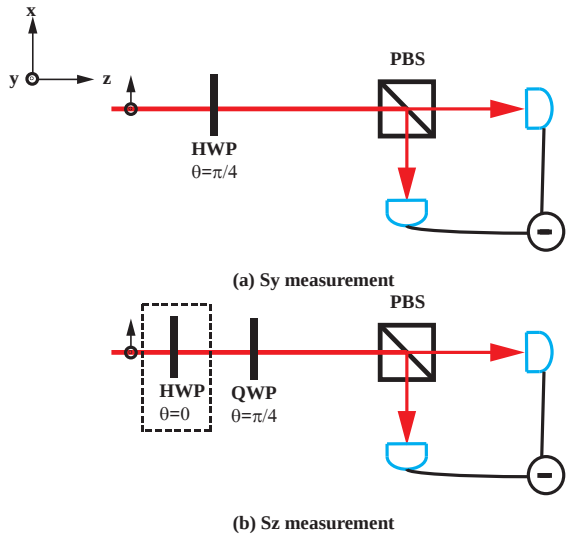

Fig. 3.21 Detector systems for measuring the $\hat{S}_y$ and $\hat{S}_z$ components,respectively. HWP: half-wave plate; QWP: quarter-wave plate; PBS: polarization beam splitter. θ is the angle between the polarization direction of light and the optical axis of waveplate.

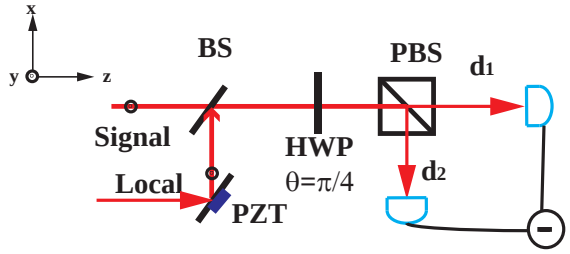

Fig. 3.22 Homodyne detection scheme. BS: 50/50 beam splitter

Figure 3.22 gives the typical homodyne detection scheme. Assuming the phase difference between the local oscillator $\hat{L}$ and the signal beam $\hat{a}$ is ϕ, and the output mode from the beam splitter can be written as

$$\hat{d}_1 = \frac{1}{\sqrt{2}}(\hat{a} - \hat{L}e^{i\phi}), \quad \hat{d}_2 = \frac{1}{\sqrt{2}}(\hat{a} + \hat{L}e^{i\phi}). \tag{3.18}$$

In the traditional scheme, the relative phase difference is controlled experimentally by the movement of piezoelectric ceramic which is connected to the high reflected mirror. The

photocurrents detected by two separated low noise detector with high gain are given as:

$$\begin{aligned} i_{d1} &= \hat{d}_1^{\dagger}\hat{d}_1 = \frac{1}{2}(\hat{a}^{\dagger}\hat{a} - \hat{a}^{\dagger}Le^{i\phi} - \hat{a}L^{\dagger}e^{-i\phi} + \hat{L}^{\dagger}\hat{L}), \\ i_{d2} &= \hat{d}_2^{\dagger}\hat{d}_2 = \frac{1}{2}(\hat{a}^{\dagger}\hat{a} + \hat{a}^{\dagger}Le^{i\phi} + \hat{a}L^{\dagger}e^{-i\phi} + \hat{L}^{\dagger}\hat{L}),, \end{aligned} \tag{3.19}$$

By linearization, which means the operator can be described by a classical component and a quantum noise operator, i.e. $\hat{a} = \alpha + \delta\hat{a}$ and $\hat{L} = l + \delta\hat{L}$, we can get the difference of photocurrents

$$\begin{aligned} i_{-} &= i_{d1} - i_{d2} = \hat{a}^{\dagger}Le^{i\phi} + \hat{a}L^{\dagger}e^{-i\phi} \\ &= \alpha^{*}le^{i\phi} + \alpha l^{*}e^{-i\phi} + \alpha^{*}\delta Le^{i\phi} + \alpha\delta L^{\dagger}e^{-i\phi} + l\delta\hat{a}^{\dagger}e^{i\phi} + l^{*}\delta\hat{a}e^{-i\phi}. \end{aligned} \tag{3.20}$$

Since in the experiment the intensity of local oscillator is much stronger than that of signal beam, i. e. $l \gg \alpha$ and assuming $l = l^{*}$, the third and fourth terms are negligible and Equation 3.20 can be simplified as

$$i_{-} = \alpha^{*}le^{i\phi} + \alpha le^{-i\phi} + l\delta\hat{a}^{\dagger}e^{i\phi} + l\delta\hat{a}e^{-i\phi}, \tag{3.21}$$

where the fluctuation part of the difference of photocurrents is

$$\delta i_{-} = l\delta\hat{a}^{\dagger}e^{i\phi} + l\delta\hat{a}e^{-i\phi}, \tag{3.22}$$

Therefore, when $\phi = 0$ $\delta i_{-} = l\delta X_s$ which is the quantum fluctuation of the amplitude quadrature, while when $\phi = \pi/2$ $\delta i_{-} = l\delta P_s$ corresponding to the quantum fluctuation of the phase quadrature. When the signal beam is replaced by the vacuum input, the quantum fluctuation is

$$\delta i_{-} = l\delta\hat{V}^{\dagger}e^{i\phi} + l\delta\hat{V}e^{-i\phi}, \tag{3.23}$$

which corresponds to the shot noise limit no matter which phase different one chooses.

In the polarization homodyne detection, by inserting a half-wave plate (HWP) in front of the polarization beam splitter (PBS), the light is split into 45° and -45° modes in the output ports of PBS ($\phi = 0$)and then directed into two photodiodes of ultra-low noise differential AC-coupled photodetector whose performance can be found in[66]. The measurement of the differential power of these two modes corresponds to the measurement of the $\hat{S}_y$ component. If we insert a quarter-wave plate (QWP) or a combination of HWP and QWP ($\phi = \pi/2$), the differential power of σ^{+} and σ^{-} modes can be detected which is the measurement of $\hat{S}_z$ component. Figure 3.23 shows the dependence of photon shot noise on the input

probe power, and the linearity demonstrates the behavior of photon shot noise limit since for the coherent state of light the variances of $\hat{S}_y$ and $\hat{S}_z$ should satisfy the condition of $Var(\hat{S}_y) = Var(\hat{S}_z) = \frac{S_x}{2} = \frac{N_{ph}}{4}$. I should mention that the data shown in Figure 3.23 were

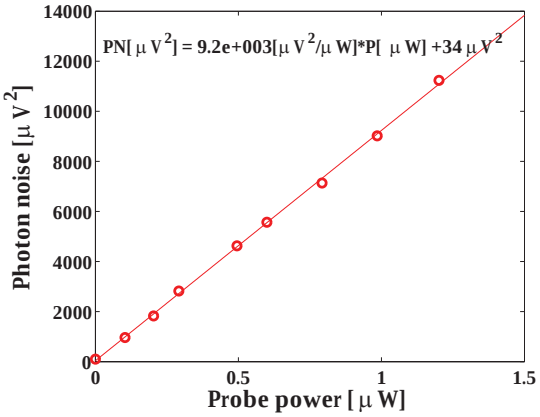

Fig. 3.23 Measured photon shot noise with different input light power.

taken by injecting the light beam into the detector directly without passing through the cavity and microcell. However, during the glass blowing phase in the fabrication of the new batch of microcell (Generation D and E), the effect of birefringence induced by intra-stress gets obvious. Although in the fabrication of Generation E an annealing process was implemented, this effect is not fully canceled which is shown in Figure 3.24. It can be explained in the following way. The cavity input linear polarized beam can be seen as a combination of σ^+ and σ^- circular polarized beam with a fixed phase difference. Inside the cavity these two modes experience fixed different phases when passing through the glass cylinder. However, the frequency fluctuation makes this phase difference random and with some uncertainty. Therefore, the output beam composed of these two circular polarized modes has the polarization uncertainty or called polarization noise.

3.6.2 Reconstruction of the atomic spin noise

Since the atomic observable cannot be measured directly in an easy way, the interaction between light and atoms is utilized to do the atomic state tomography where the information of atomic spins is mapped onto the light field which serves as quantum bus, and then read out by means of the detection of light.

In the QND picture we have derived the input-output relations for the light and atoms as Equation 2.31, and the corresponding quantum variances for the measured light observable

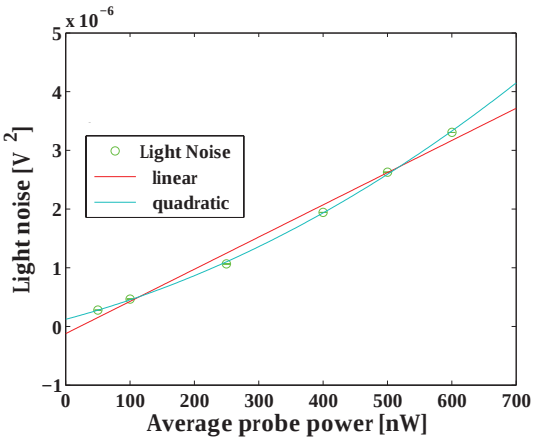

Fig. 3.24 Measured photon noise with different light power when Microcell E4 is coupled into the optical cavity.

can be given as follows

$$\begin{pmatrix} Var(\hat{x}_c^{out}) \\ Var(\hat{x}_s^{out}) \end{pmatrix} = \begin{pmatrix} Var(\hat{x}_c^{in}) \\ Var(\hat{x}_s^{in}) \end{pmatrix} + \frac{\kappa^2}{2}\begin{pmatrix} Var(\hat{p}_A^{in}) \\ Var(\hat{x}_A^{in}) \end{pmatrix} + \frac{\kappa^4}{16}\begin{pmatrix} Var(\hat{p}_s^{in}) \\ Var(\hat{p}_c^{in}) \end{pmatrix}, + \frac{\kappa^4}{48}\begin{pmatrix} Var(\hat{p}_{s,1}^{in}) \\ Var(\hat{p}_{c,1}^{in,}) \end{pmatrix} \tag{3.24}$$

Assuming the collective spin state of an atomic ensemble is prepared in CSS state which gives $Var(\hat{x}_A^{in}) = Var(\hat{p}_A^{in}) = \frac{1}{2}$, and the light field is shot noise limited, which means $Var(\hat{x}_{c,s}^{in}) = Var(\hat{p}_{c,s}^{in}) = \frac{1}{2}$ and $Var(\hat{p}_{c,1}^{in}) = Var(\hat{p}_{s,1}^{in}) = \frac{1}{2}$, Equation 3.24 can be simplified to

$$Var(\hat{x}_{c(s)}^{out}) = \frac{1}{2}[1 + \kappa^2/2 + \kappa^4/12]. \tag{3.25}$$

Physically, the first term is the shot noise of the probe light, the second term describes the spin noise, and the last term is from the quantum backaction noise of the measurement. In the experiment, the time-integrated homodyne signal is scaled by the shot noise of the light. Figure 3.25 shows the measured noise of $\hat{x}_{c,s}^{out}$ where the falling mode function $e^{-\gamma T}$ with $\gamma = 1/T_2$ has been used as mentioned in Chapter 2. The quadratic dependence of measured noise on the probe power is partially from the backaction contribution shown in Equation 3.25 since $\kappa^2 \propto N_{ph}$ as well as the spontaneous emission. To understand Equation 3.25, the measured noise from the output light $\sigma^2_{measured}(\hat{S}_y^{out})$ is firstly normalized into the shot noise unit as $Var(\hat{x}_{c(s)}^{out}) = \frac{\sigma^2_{measured} - \sigma^2_{EN}}{\sigma^2_{lightraw} - \sigma^2_{EN}}$ where σ^2_{EN} is the noise floor coming from the measurement apparatus or called electronic noise, and the corresponding data are shown in Figure 3.26. As discussed above, the coupling strength κ^2 is proportional to the photon number or probe

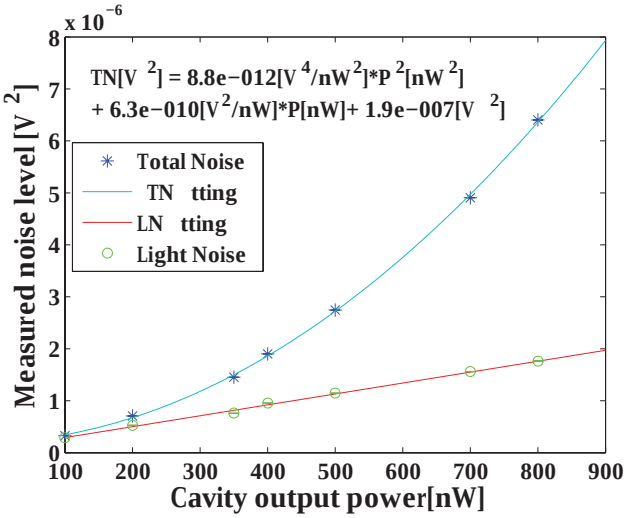

Fig. 3.25 The measured noise level as a function of probe power with the interaction time of $T = 0.5$ms

power. The quadratic dependence of $Var(\hat{x}^{out}_{c(s)})$ on the probe power originates from the effect of quantum backaction and the decoherence resulting from spontaneous emission. The quadratic behavior from quantum backaction noise has been explained, and additionally as for the spontaneous emission it can be intuitively understood in the following way. As described in[29], spontaneous emission rate can be read as $\eta = \frac{\kappa^2}{d}$ where d is the optical depth in the atomic ensemble, and this decay effect can be simply seen as a loss channel similar to the beam splitter model. In other word, the noise term from the spin contribution including the spontaneous emission can be rewritten as $\frac{\kappa^2}{2}(1 + C\frac{\kappa^2}{d}) = \frac{\kappa^2}{2} + C\frac{\kappa^4}{2d}$ where C is a constant of the order unity. Thus, the decoherence from spontaneous emission is proportional to κ^4 as well as backaction noise. Therefore, in this picture the atomic noise can be calculated as

$$Var(\hat{p}_A) = \frac{2}{\kappa^2}[\frac{\sigma^2_{measured} - \sigma^2_{EN}}{\sigma^2_{lightraw} - \sigma^2_{EN}} - (1 + \frac{\kappa^4}{12})] \tag{3.26}$$

However, if we can do a back-action evasion measurement and assume the spontaneous emission is weak, the terms proportional to fourth power of κ will almost disappear which makes the analysis easier. In this case, the quantum variance of atomic spins can be written as

$$Var(\hat{p}_A) = \frac{2}{\kappa^2}[\frac{\sigma^2_{measured} - \sigma^2_{EN}}{\sigma^2_{lightraw} - \sigma^2_{EN}} - 1]. \tag{3.27}$$

Although this scheme will be discussed in the following chapter, here I simply show the result in Figure 3.27. The reconstructed atomic noise in the thermal equilibrium and highly

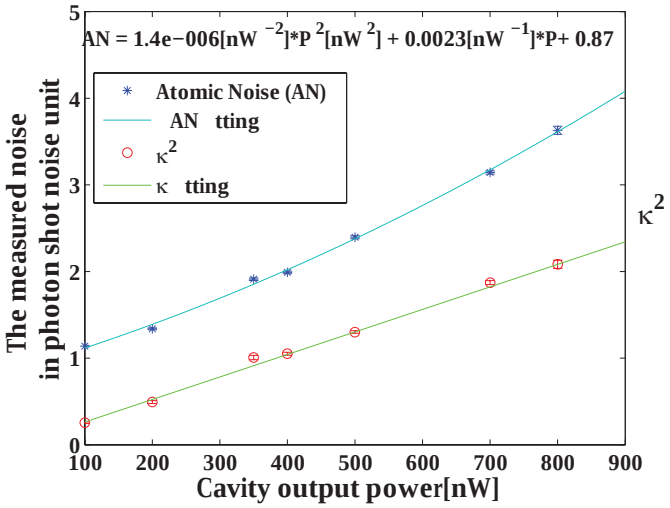

Fig. 3.26 The normalized noise level as a function of probe power. Atomic noise (AN) means the measured total noise has been normalized into the light shot noise unit.

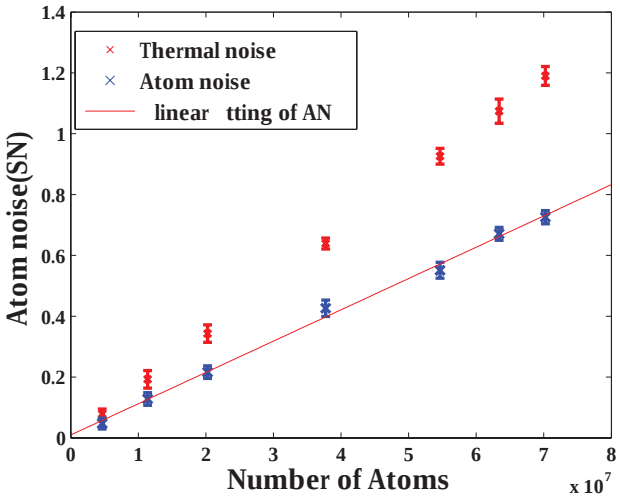

Fig. 3.27 Atomic noise of polarized and unpolarized atoms for different number of atoms.

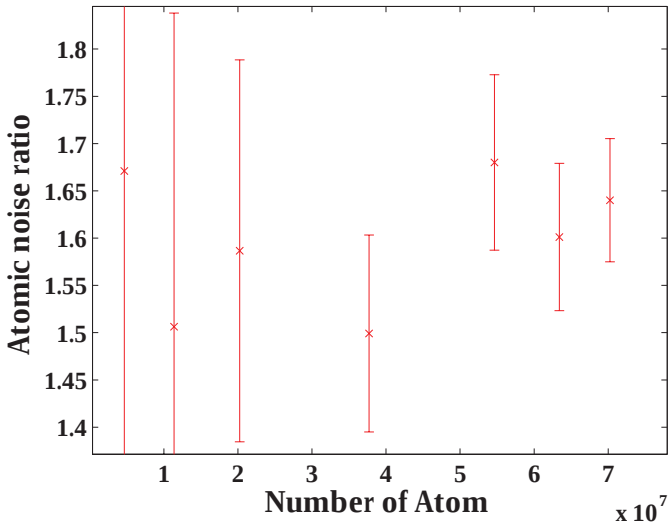

Fig. 3.28 Atomic noise ratio of unpolarized and polarized atomic ensembles for different number of atoms.

polarized state are plotted as a function of the number of atoms in the cell. The linear dependence of atomic noise to some extent proves the fact of back-action evasion. Figure 3.28 gives the ratio of thermal atomic noise and highly polarized atomic noise. In the ideal case (CSS state), the ratio should be $\frac{15}{8} = 1.875$, however, as mentioned earlier in this chapter the spin orientation is around 98% which leads to the atomic noise 15% above the atomic projection noise according to the dependence of atomic noise on the spin orientation shown in Figure 3.29. This is in agreement with the experimental results presented here.

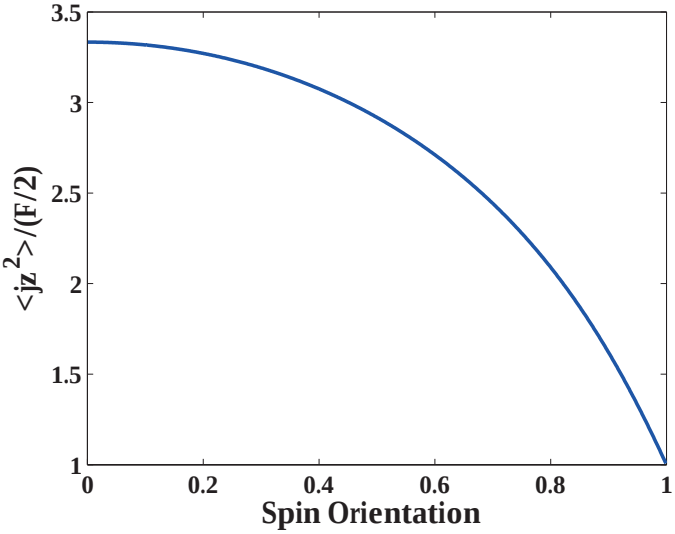

Fig. 3.29 Noise versus spin orientation in atomic projection noise unit.

Chapter 4

Backaction evasion and conditional spin squeezing by stroboscopic probing

4.1 Stroboscopic probing

4.1.1 Introduction

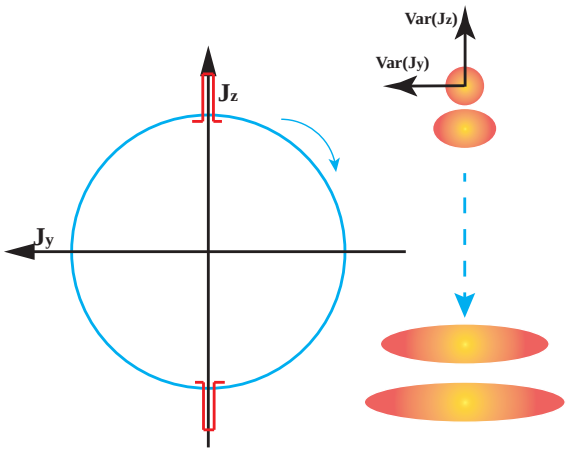

Fig. 4.1 Scheme of Stroboscopic probing procedure.

In this chapter we describe the "Generation of a squeezed state of an oscillator by stroboscopic back-action-evading measurement" experiment. Although the Heisenberg uncertainty sets the limit of how precisely two non-commuting variables, such as canonical atomic variables with the commutation relation $[\hat{x}_A, \hat{p}_A] = i$, can be measured simultaneously, when probing a single quadrature[67]. In other words, single-quadrature detection can take a form similar to a QND measurement where the backaction does not affect the dynamics of

the quantity being measured and only the conjugate unmeasured quadrature suffers from the backaction disturbance. In order to remove the accuracy limit set by the quantum mechanical backaction during the measurement of single quadrature of mechanical oscillator's motion, Braginsky *et al* [68]and Zimmermann *et al*[69] suggested to modulate the measurement strength with the period proportional to half period of the oscillation. This method is called stroboscopic backaction evading measurement.

4.1.2 Protocol

To understand this scheme intuitively, I make a drawing in Figure 4.1. For the spin oscillator with Larmor frequency Ω one of the canonical variables can be expressed as $\hat{X}(t) = \hat{X}_0\cos(\Omega t) + \hat{P}_0\cos(\Omega t)$ with $\hat{X}_0 = \frac{\hat{J}_y^{in}}{\sqrt{J_x}}$ and $\hat{P}_0 = \frac{\hat{J}_z^{in}}{\sqrt{J_x}}$. And the light-atom interaction (the coupling between meter and system being measured) can be approximated by the QND-type Hamiltonian $\hat{H}_{\rm int} = 2\frac{\kappa}{\sqrt{N_{ph}J_x}}\hat{S}_z\hat{J}_z$ when laser detuning is large enough, i.e. $\left[\hat{H}_{\rm int}, \hat{J}_z\right] = 0$. If the δ-pulsed probing is switched on at times $t = 0, \frac{\pi}{\Omega}, ..., \frac{n\pi}{\Omega}$ the noise of the probe light does not couple to the spin component $\hat{J}_z$, however, the other conjugate quadrature $\hat{J}_y$ will be strongly disturbed by the backaction noise. In such an ideal setup, only measurement-imprecision noise associated with intrinsic fluctuation of the detection affects the measurement precision which is the shot noise in the light.

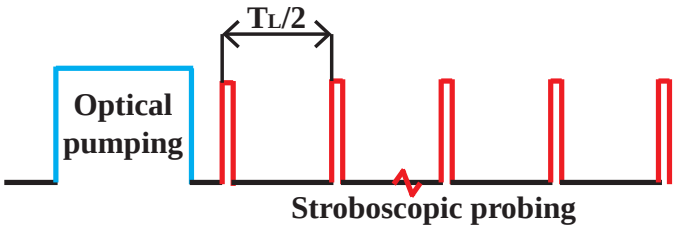

Fig. 4.2 Pulse sequence of stroboscopic backaction-evading measurement. T_L is the period of Larmor oscillation.

In our scheme the Stokes element $\hat{S}_y^{out}$ of the linearly polarized probe beam with stroboscopic intensity-modulation at twice the spin oscillator frequency is detected and the Fourier component $\cos(\Omega t)$ is measured by a lock-in amplifier. In this case the measured atomic variable $\frac{\hat{J}_z(t)}{\sqrt{J_x}}$ is integrated over one Larmor cycle and weighted with a cosine wave (from the lock-in amplifier demodulation) and a pulse-shaped function (from the stroboscopic modulation of the probe)

$$\hat{X}(kT) = \frac{1}{TD}\int_{kT}^{(k+1)T} dt \frac{\hat{J}_z(t)}{\sqrt{J_x}} u(t)\cos(\Omega t) \tag{4.1}$$

where $k \in \mathbb{N}$, $T = 2\pi/\Omega$ is the Larmor period, and the stroboscopic function $u(t)$ with duty cycle D is given by:

$$u(t) = \begin{cases} 1 & : \quad -\frac{DT}{4} + kT \leq t \leq \frac{DT}{4} + kT \\ 0 & : \quad \frac{DT}{4} + kT < t < -\frac{DT}{4} + (k+1/2)T \\ 1 & : \quad -\frac{DT}{4} + (k+1/2)T \leq t \leq \frac{DT}{4} + (k+1/2)T \end{cases} \tag{4.2}$$

We defined $u(t)$ in such a way so that the the overlap with the lock-in cosine quadrature is maximized.

To simplify the calculation we will consider no weighting of the data with a mode function, so that the measurement record of cosine quadrature $\hat{S}_y^{out}$ over the measurement period of time $\tau = NT$ is given by:

$$S_{y,\tau} = \sum_{k=0}^{N} \left[\hat{Y}(kT) + \beta \bar{S}_x T \sqrt{J_x} \hat{X}(kT)\right] \tag{4.3}$$

$$\hat{Y}(kT) = \int_{kT}^{(k+1)T} dt \hat{S}_y^{in}(t) u(t) \cos(\Omega t), \tag{4.4}$$

where β is defined as $\beta = a = -\frac{\Gamma\lambda^2}{8A\Delta 2\pi} a_1$. Note that$\langle \hat{X}(k_1 T)\hat{Y}(k_2 T)\rangle = 0$ since there are no correlations between $\hat{S}_y^{in}$ and the spin components.

For a coherent field linearly polarized in the y-direction $\langle \hat{S}_y^{in}(t)\hat{S}_y^{in}(t')\rangle = \langle \hat{S}_z^{in}(t)\hat{S}_z^{in}(t')\rangle = \frac{S_x}{2}\delta(t-t')$ and $|\langle S_x\rangle| = S_x = \frac{\Phi T}{2}$ where Φ is the flux of photons, and thus

$$\langle \hat{Y}(k_1 T)\hat{Y}(k_2 T)\rangle = \frac{\bar{\Phi} T}{8}\left[1 + \mathrm{Sinc}\left(\pi D\right)\right]\delta_{k_1 k_2} = \langle \hat{Y}^2\rangle_0 \delta_{k_1 k_2} \tag{4.5}$$

where $\bar{S}_x = \frac{\bar{\Phi} T}{2}$ denotes the average over the whole Larmor period, and δ denotes the Kronecker delta.

The variable $\hat{X}(kT)$ has two contributions:

$$\hat{X}(kT) = \breve{X}(kT) + \tilde{X}(kT) \tag{4.6}$$

The term $\breve{X}(kT)$ gives rise to the effective "spin projection noise"[1] related to the initial

[1] Spin projection noise is used to describe the noise in the $\hat{J}_z$ variable. Here, the variable is not $\hat{J}_z$.

quantum state of the ensemble

$$\begin{aligned}\breve{X}(kT) &= \frac{1}{TD}\int_{kT}^{(k+1)T} dtu(t)\cos(\Omega t)\left[\frac{\hat{J}_z^{in}}{\sqrt{J_x}}\cos(\Omega t)+\frac{\hat{J}_y^{in}}{\sqrt{J_x}}\sin(\Omega t)\right] \\ &= \frac{\hat{J}_z^{in}\left[1+\mathrm{Sinc}(\pi D)\right]}{2\sqrt{J_x}},\end{aligned} \tag{4.7}$$

where the fact of $\cos(\alpha)=\cos(-\alpha)$ is used to achieve the result in the second line. The'spin projection noise" corresponds to the noise level:

$$\begin{aligned}\langle\hat{X}^2\rangle_0 = \langle\breve{X}^2\rangle &= \frac{\langle(\hat{J}_z^{in})^2\rangle\left[1+\mathrm{Sinc}(\pi D)\right]^2}{4J_x} \\ &= \frac{\left[1+\mathrm{Sinc}(\pi D)\right]^2}{8},\end{aligned} \tag{4.8}$$

where we use the CSS state condition $\mathrm{Var}(\frac{\hat{J}_z^{in}}{\sqrt{J_z}})=\frac{1}{2}$ so that the conditional variance should be compared with this level. The term $\tilde{X}(kT)$ in Equation (4.6) gives rise to the noise that describes the coupling of the quantum probe noise to the measured $\hat{J}_z$ (i.e. backaction effect):

$$\begin{aligned}\tilde{X}(kT) &= \frac{1}{TD}\int_{kT}^{(k+1)T} dtu(t)\cos(\Omega t)\frac{\tilde{J}_z(t)}{\sqrt{J_x}} \\ \tilde{J}_z(t) &= \beta\bar{J}_x\int_0^t dt'\sin\left[\Omega(t-t')\right]\hat{S}_z(t')\end{aligned} \tag{4.9}$$

Clearly:

$$\langle\breve{X}(k_1T)\tilde{X}(k_2T)\rangle = 0 \tag{4.10}$$

The correlation $\langle \tilde{X}(k_1T)\tilde{X}(k_2T)\rangle$ can be written as:

$$\begin{aligned}\langle \tilde{X}(k_1T)\tilde{X}(k_2T)\rangle = &\frac{1}{(TD)^2 J_x}\int_{\alpha(k_1)}^{\beta(k_1)}\int_{\alpha(k_2)}^{\beta(k_2)} dt_2 dt_1 \cos(\Omega t_1)\cos(\Omega t_2)\langle \tilde{J}_z(t_1)\tilde{J}_z(t_2)\rangle \\ &+\frac{1}{(TD)^2 J_x}\int_{\alpha(k_1)}^{\beta(k_1)}\int_{\gamma(k_2)}^{\delta(k_2)} dt_2 dt_1 \cos(\Omega t_1)\cos(\Omega t_2)\langle \tilde{J}_z(t_1)\tilde{J}_z(t_2)\rangle \\ &+\frac{1}{(TD)^2 J_x}\int_{\gamma(k_1)}^{\delta(k_1)}\int_{\alpha(k_2)}^{\beta(k_2)} dt_2 dt_1 \cos(\Omega t_1)\cos(\Omega t_2)\langle \tilde{J}_z(t_1)\tilde{J}_z(t_2)\rangle \\ &+\frac{1}{(TD)^2 J_x}\int_{\gamma(k_1)}^{\delta(k_1)}\int_{\gamma(k_2)}^{\delta(k_2)} dt_2 dt_1 \cos(\Omega t_1)\cos(\Omega t_2)\langle \tilde{J}_z(t_1)\tilde{J}_z(t_2)\rangle\end{aligned} \tag{4.11}$$

where:

$$\begin{aligned}\alpha(k) &= -TD/4 + kT, \;\; \gamma(k) = -TD/4 + (k+1/2)T, \\ \beta(k) &= \;\; TD/4 + kT, \;\; \delta(k) = \;\; TD/4 + (k+1/2)T\end{aligned} \tag{4.12}$$

To evaluate the correlation $\langle \tilde{X}(k_1T)\tilde{X}(k_2T)\rangle$ we need to know the correlation $\langle \tilde{J}_z(t_1)\tilde{J}_z(t_2)\rangle$, which is:

$$\begin{aligned}\langle \tilde{J}_z(t_1)\tilde{J}_z(t_2)\rangle &= \beta^2 \bar{J}_x^2 \int_0^{t_1}\int_0^{t_2} d\tau_1 d\tau_2 \sin\left[\Omega(t_1-\tau_1)\right]\sin\left[\Omega(t_2-\tau_2)\right]\langle \hat{S}_z(\tau_1)\hat{S}_z(\tau_2)\rangle \\ &= \frac{\beta^2 \bar{J}_x^2 \bar{S}_x}{D}\int_0^{\min(t_1,t_2)} d\tau \sin\left[\Omega(t_1-\tau)\right]\sin\left[\Omega(t_2-\tau)\right] u(\tau)\end{aligned} \tag{4.13}$$

The integral I in Equation (4.13) can be written in the form:

$$I = \frac{(1+N_p)TD}{2}\Big\{\cos\left[\Omega(t_1-t_2)\right] - \cos\left[\Omega(t_1+t_2)\right]\mathrm{Sinc}\left(\pi D\right)\Big\} + \delta I \tag{4.14}$$

where $N_p \in \mathbb{N}$ is the number of Larmor cycles in the $\min(t_1,t_2)$, defined by the equation

$$N_p = \mathrm{Int}\left\{\min(t_1,t_2)/T\right\} \tag{4.15}$$

and

$$\delta I = \int_{-DT/4+(N_p+1)T}^{\min(t_1,t_2)} d\tau \sin\left[\Omega(t_1-\tau)\right]\sin\left[\Omega(t_2-\tau)\right] u(\tau) \tag{4.16}$$

which gives:

$$\delta I = \begin{cases} \delta I_1 & : \quad -\frac{DT}{4} + (N_p+1)T \le \min(t_1,t_2) \le \frac{DT}{4} + (N_p+1)T \\ \delta I_2 & : \quad \frac{DT}{4} + (N_p+1)T < \min(t_1,t_2) < -\frac{DT}{4} + (N_p+3/2)T \\ \delta I_3 & : \quad -\frac{DT}{4} + (N_p+3/2)T \le \min(t_1,t_2) \le \frac{DT}{4} + (N_p+3/2)T \end{cases} \tag{4.17}$$

where:

$$\begin{aligned} \delta I_1 &= \frac{\min(t_1,t_2) - (N_p+1)T + TD/4}{2} \cos\left[\omega(t_1-t_2)\right] \\ &\quad + \frac{T}{8\pi} \sin\left[\omega|t_1-t_2|\right] - \frac{T}{8\pi} \sin\left[\pi D + \omega(t_1+t_2)\right] \\ \delta I_2 &= \frac{TD}{4}\left[\cos\left[\omega(t_1-t_2)\right] - \cos\left[\omega(t_1+t_2)\right] \mathrm{Sinc}(\pi D)\right] \\ \delta I_3 &= \frac{\min(t_1,t_2) - (N_p+3/2)T + 3TD/4}{2} \cos\left[\omega(t_1-t_2)\right] \\ &\quad + \frac{T}{8\pi}\left[\sin\left[\omega|t_1-t_2|\right] + \sin\left[\omega(t_1+t_2) - \pi D\right] - 2\sin\left[\omega(t_1+t_2) + \pi D\right]\right] \end{aligned} \tag{4.18}$$

We can then evaluate the integrals in Equation (4.11), and after some algebra we have:

$$\langle \tilde{X}(k_1 T)\tilde{X}(k_2 T)\rangle = \frac{\left[\mathfrak{K} + 2\min(k_1,k_2)\right]\beta^2 J_x \bar{\Phi}_x T}{64}\left[1 - \mathrm{Sinc}(\pi D)\right]\left[1 + \mathrm{Sinc}(\pi D)\right]^2 \tag{4.19}$$

where $\mathfrak{K}$ is a numerical factor with the values of

$$\mathfrak{K}\begin{cases} = 1 & k_1 \neq k_2 \\ \approx 2.4 & k_1 = k_2 \end{cases} \tag{4.20}$$

Here, we will consider the case where we are measuring over many cycles. In this case the exact value of $\mathfrak{K}$ will not be relevant ($\mathfrak{K} \ll N$), and the measurement variance is

$$\begin{aligned} Var(\hat{S}^{out}_{y,\tau}) &= N\langle \hat{Y}^2\rangle_0 + \frac{\beta^2 J_x \bar{\Phi}^2 N^2 T^2}{4} Var\left(\frac{\hat{J}^{in}_z}{\sqrt{J_x}}\right) + \frac{\beta^2 J_x \bar{\Phi}^2 T^2}{4} \sum_{k_1=0}^{N-1}\sum_{k_2=0}^{N-1} \langle \tilde{X}(k_1 T)\tilde{X}(k_2 T)\rangle \\ &\approx \frac{\bar{\Phi}\tau}{8}\left[1 + \mathrm{Sinc}(\pi D)\right]\left[1 + \tilde{\kappa}^2 + \frac{\tilde{\kappa}^4}{3}\frac{1 - \mathrm{Sinc}(\pi D)}{1 + \mathrm{Sinc}(\pi D)}\right] \end{aligned} \tag{4.21}$$

where the effective coupling constant is

$$\tilde{\kappa}^2 = \frac{1}{4}\beta^2 J_x \bar{\Phi}_x \tau\left[1 + \mathrm{Sinc}(\pi D)\right], \tag{4.22}$$

with $\tau = NT$ being the total measurement time. It can be found in Equation 4.21 that for a stroboscopic probing the backaction coupling constant is given by

$$C = \frac{1 - \mathrm{Sinc}(\pi D)}{1 + \mathrm{Sinc}(\pi D)}, \tag{4.23}$$

As shown in Figure 4.3 when the duty cycle is 0, which means stroboscopic modulated

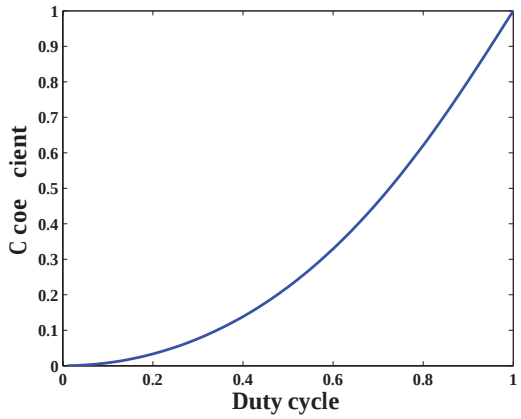

Fig. 4.3 Backaction coupling constant C coefficient dependent on duty cycle.

probe beam behaves as a δ pulse sequence a perfect QND measurement ($C = 0$) can be achieved, while for a continuous probing (i.e.duty cycle $D = 100\%$) $C = 1$.

4.2 Experimental demonstration of backaction evasion measurement

The spin oscillator is realized in room-temperature, optically-pumped Cesium atoms, contained in a glass cell microchannel, $300\mu m \times 300\mu m$ in cross section and 1 cm in length. An alkene coating deposited at the inner cell walls dramatically suppresses spin-relaxation due to the wall collisions. Atoms bounce off the walls and cross the optical mode cross section with the waist of $55\mu m$ approximately 5×10^3 times before their quantum spin state decoheres in 10ms due to wall collisions. The atom-atom collision rate at the low Cs pressure used here is negligible. As the typical light pulse duration of 0.5ms is much greater than the atom transient time of 1.5μsec and the oscillator period (typical $\Omega \sim 380$kHz) the thermally moving atoms cross the optical mode many times in the same state and hence the detected optical mode couples to the symmetric spin mode (equivalently to the oscillator position $\hat{X}$). We emphasize that the thermal motion of the atoms does not affect the oscilla-

tor temperature, which is determined by the spin distribution. The microcell is placed inside a standing wave optical cavity with a finesse $F \approx 17$ determined by the single-pass losses in the cell windows of 6.5% and the output coupler transmission of 80% which is close to the optimal value $T_{out} \approx l_{cav}$ where l_{cav} is the round trip loss when light propagates through the cell. The cavity is kept on resonance with light using the Pound-Drever-Hall technique. The number of atoms in the F = 4 hyperfine ground state coupled to the light field has been adjusted within the $\sim 10^7 - 10^8$ range by changing the cell temperature (typically $\sim 26^\circ$) and optical pumping for the maximal QND interaction strength. The frequency of the oscillator can be tuned with B_0. An acousto-optic modulator is used to stroboscopically modulate the intensity of the probe beam at twice the Larmor frequency. The experiment was operated with $\sim 15\%$ stroboscopic duty cycle, with probe wavelength blue detuned by 1.6GHz with respect to the D2 transition. The $\hat{S}_{y,\tau}$ operator is measured by balanced polarimetry and lock-in detection. The data are weighted with an exponential mode function: $f(t) = e^{-\gamma t}$ where γ is the decoherence rate in the presence of the probe. The exponential falling mode function is used to assess the measured noise. To collect statistics for the variance estimation, each measurement is repeated 2×10^4 times.

Photon shot noise level

The photon shot noise level can be estimated from a polarimetry noise measurement when the oscillator frequency is tuned away from the lock-in detection bandwidth. The noise associated with the spin-oscillator has a Lorentzian power spectrum centered at Larmor frequency with width set by the decoherence rate; therefore if the oscillator frequency is set many line-widths away from the lock-in bandwidth, the oscillator noise is filtered out and the measurement noise only depends on the probe light noise of white spectrum. The oscillator frequency can be tuned by changing the bias magnetic field. The probe noise is verified to scale linearly with the power as expected for the photon shot noise power. The $\cos(\Omega t)$ component of the measurement $\hat{\tilde{S}}_y^{out}$ over time τ, weighted by the exponential mode function $f(t) = e^{-\gamma_m t}$ is given by $PSN_\tau = \mathrm{Var}[\int_0^\tau dt \hat{\tilde{S}}_y^{out} \cos(\Omega t) f(t)]$

Electronic noise and detection losses

The photodetector electronic noise is at the level of $\sim 10\%$ of the photon shot noise for the power used in the squeezing experiment. The detection efficiency of the light field at the output of the cavity is $\sim 85\%$, limited mainly by the detector quantum efficiency.

Atomic CSS state noise

The oscillator ground state noise is calibrated against a measurement in the thermal state of the atomic ensemble. Including decoherence, but neglecting change in the spin variance (e.g. due to loss of atoms from depumping into the F = 3 manifold. Also, we neglect that the variance of the noise changes due to the change in the spin polarization.), the two-time spin correlation can be written in the form: $\langle \hat{J}_z(t)\hat{J}_z(t')\rangle = \langle \hat{J}_z^2\rangle e^{-\gamma|t-t'|}\cos[\Omega(t-t')]$,where γ is the decay rate and $\langle \hat{J}_z^2\rangle$ is the variance in the spin state. It can be shown that the $\cos(\Omega t)$ component of the measurement $\hat{S}_y^{out}$ over time τ, weighted by the exponential mode function $f(t) = e^{-\gamma_m t}$is given (in the absence of back-action) by:

$$\frac{\mathrm{Var}[\int_0^\tau dt \hat{S}_y^{out}\cos(\Omega t)f(t)]}{PSN_\tau} = 1 + 2\beta^2 S_x \frac{\gamma - e^{2\gamma_m\tau}\gamma + [1 + e^{2\gamma_m\tau} - 2e^{(\gamma_m-\gamma)\tau}]\gamma_m}{(e^{2\gamma_m\tau}-1)(\gamma_m-\gamma)(\gamma_m+\gamma)}\langle \hat{J}_z^2\rangle, \quad (4.24)$$

which for $\gamma_m = \pm\gamma$ reduces to:

$$\frac{\mathrm{Var}[\int_0^\tau dt \hat{S}_y^{out}\cos(\Omega t)f(t)]}{PSN_\tau} = 1 + \beta^2 S_x \tau \frac{1 + \gamma\tau - \gamma\tau\coth(\gamma\tau)}{\gamma\tau}\langle \hat{J}_z^2\rangle. \quad (4.25)$$

In the thermal state, where no back-action occurs, the spin variance is

$$\langle \hat{J}_z^2\rangle_{thermal} = \frac{2F+1}{4F} N_A F(F+1)/3 \quad (4.26)$$

where F = 4 is the total spin in the probed manifold, N_A is the total number of atoms in the ensemble and the factor $(2F+1)/(4F)$ is the fraction of atoms in the F = 4 manifold when the atoms in the ensemble are in the thermal state. We note that in the experiment described here, the contribution of atoms in the F = 3 manifold to the thermal spin noise measurement is estimated to be $< 3\%$. The ground state of the oscillator corresponds to the coherent spin state of maximum $J_x = N_A F$, leading to $\langle \hat{J}_z^2\rangle = N_A F/2$. Assuming the same decoherence rate for coherent and thermal states, we find that the contribution of atomic spin in the ground state with $J_x = N_A F$ to the measured noise is given by (in units of PSN_τ):

$$\kappa^2 \mathrm{Var}(\hat{p}_A)_0 = \frac{6F}{(F+1)(2F+1)}\left[\frac{\mathrm{Var}[\int_0^\tau dt \hat{S}_y^{out}\cos(\Omega t)f(t)]_{thermal}}{PSN_\tau} - 1\right]. \quad (4.27)$$

There is a small discrepancy in the decoherence rate and the loss rate of atoms due to the probe scattering for the coherent and thermal rates; for the timescales of the experiment, the effect of this difference is estimated to be less than 10%. In Figure 4.4 the atomic noise

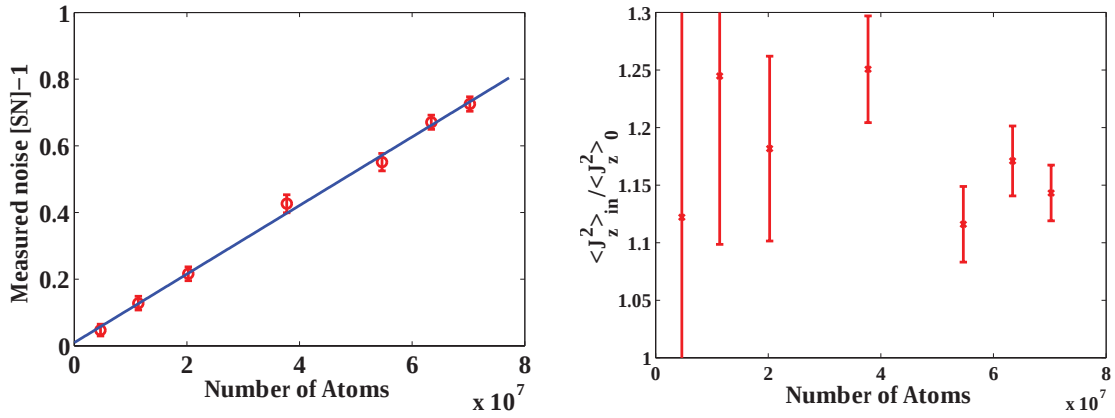

(a) (b)

Fig. 4.4 (a)Measured noise for different atom numbers where the measured noise is first normalized to the photon shot noise and then the unity is subtracted.(b)Measured spin noise that is normalized into CSS spin noise for different the number of atoms.

variance in the state prepared by optical pumping is plotted as a function of the atomic number. The observed linear scaling indicates a quantum-limited performance and a QND character of the measurement. In the right graph the ratio of the measured variance to the calibrated CSS state imprecision is shown to be 1.16 at the working point (last point corresponds to $26.5°C$). The increased measured variance in the initial atomic state is due to the imperfect optical pumping. The occupation probability distribution among the Zeeman levels can be found from the magneto-optical resonance signal. Assuming a spin-temperature distribution, it is found that after optical pumping $\sim 98\%$ of the atoms are in the end state $|F=4,m_F=4\rangle$, with $\sim 2\%$ occupation probability for the $|F=4,m_F=3\rangle$ state, and negligible probabilities for the other states. This is consistent with the $\sim 16\%$ increase of the measured variance compared to the CSS state noise. As mentioned before, in order to change the atomic density heating is still kept but instead of air heating a twisted wire with high resistance is wound around the aluminum cylinder where most of the magnetic coils are attached(see Appendix 1). By adding the current on this wire the stable environment temperature can be established inside the cylinder (the range is $17°C \sim 27°C$). Additionally, we decrease the number of atoms furthermore by weakening the repump beam but keeping the same intensity of pump beam to reduce the number of atoms staying in $F=4$. In this scheme, the number of atoms is calibrated against a response to a RF field.

The QND character of the measurement is demonstrated in Figure 4.5, where the measured variance of the spin oscillator is plotted as a function of the number of the probe photons in the pulse. For a continuous probe (100% duty cycle), the imprecision in units of CSS state fluctuations increases with the number of photons in the pulse. In contrast, for

a stroboscopic probe with a small duty cycle ($\sim 15\%$) the noise remains nearly independent of the pulse strength over the measured range. The demonstrated reduction of probe back-action is more than 10dB compared to a continuous probing of the atomic ensemble.

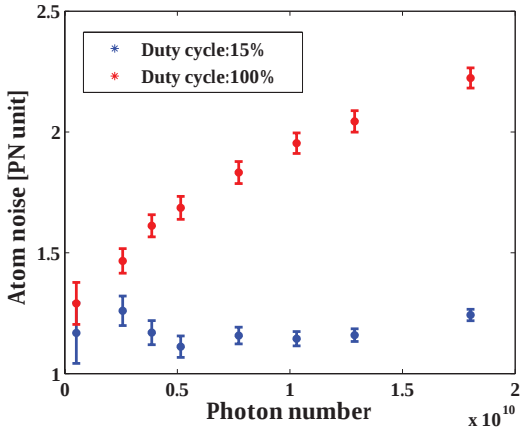

Fig. 4.5 Measured spin noise that is normalized into CSS spin noise for different photon numbers.

4.3 2dB-conditional spin squeezing

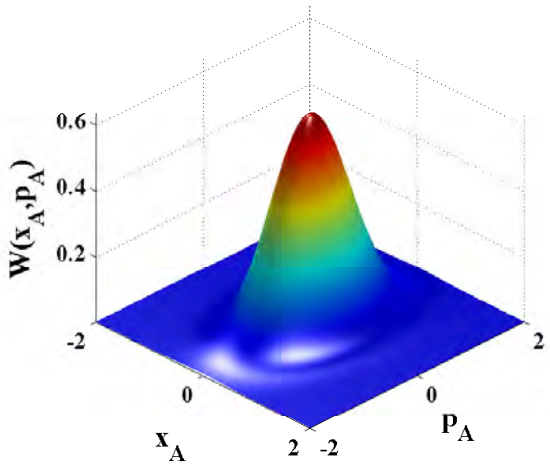

Fig. 4.6 Wigner distribution of atomic coherent state.

4.3.1 Introduction

Surpassing the standard quantum limit in the measurement has been always a long-term goal for quantum metrology and quantum communication. Recently, squeezed vacuum states of light has been used to improve the sensitivity of a gravitational-wave observatory in GEO200 project[12]. Spin-squeezed states of atomic ensembles was suggested to be prepared for the improvement of sensitivity in atomic spectroscopy, interferometry and atomic clocks[13, 14, 15, 16]. Until now, several schemes have been proposed to generate spin-squeezed states, including the direct interaction of spins[17], electron-nucleus entanglement[18], mapping of squeezed light onto atoms[19], multiple passes of light through atoms[20] and a projective Faraday interaction based on QND measurement[21, 22]. In this section we report the realization of spin squeezing by QND measurement.

4.3.2 Squeezing mechanism

Measurement process can be usually divided into three distinct sections: the preparation of a probe, its interaction with the system to be measured and the probe readout. In our protocol a Faraday interaction is utilized to create the correlation between light and atoms, and then this shot-noise limited light beam as a probe is sent to the homodyne detection system to extract the information of one of the spin components projecting the collective spin into a state with reduced fluctuations in this component. In general, the input-output relations after backaction-evading measurement can be given as

$$\begin{aligned} \hat{x}_L^{out} &= \hat{x}_L^{in} + \tilde{\kappa}\hat{p}_A^{in} \\ \hat{p}_A^{out} &= \hat{p}_A^{in}, \end{aligned} \tag{4.28}$$

where $\hat{x}_L$ and $\hat{p}_A$ represent the canonical variables of light and atoms, respectively. According to the formula for the variance of a Gaussian distributed variable $\hat{p}_A$ conditioned on the measurement of another correlated Gaussian variable $\hat{x}_L$ which is

$$\mathrm{Var}\left[\hat{p}_A\right]\Big|_{\hat{x}_L} = \mathrm{Var}\left[\hat{p}_A\right] - \frac{\mathrm{Cov}^2\left[\hat{p}_A,\hat{x}_L\right]}{\mathrm{Var}\left[\hat{x}_L\right]} \tag{4.29}$$

where $\mathrm{Cov}\left[\hat{p}_A,\hat{x}_L\right]$ represents the covariance of $\hat{x}_L$ and $\hat{p}_A$, we can calculate the conditional variance of one spin component $\hat{p}_A$ as

$$\mathrm{Var}\left[\hat{p}_A\right]\Big|_{\hat{x}_L} = \frac{1}{1+\tilde{\kappa}^2}\frac{1}{2}, \tag{4.30}$$

where we assume the initial light and atoms are prepared in their coherent states.

Following the discussion in the previous section, backaction evading measurement by the stroboscopic modulation of the probe can be used to generate a spin squeezed state. And the corresponding conditional variance of the collective spin component $\hat{X}(NT)$ can be read as

$$\mathrm{Var}\left[\hat{X}(NT)\right]\Big|_{\hat{S}_{y,\tau}} = \langle \hat{X}^2(NT)\rangle - \frac{\mathrm{Cov}^2\left[\hat{X}(NT),\hat{S}_{y,\tau}\right]}{\mathrm{Var}\left[\hat{S}_{y,\tau}\right]}, \tag{4.31}$$

where $\mathrm{Cov}\left[\hat{X}(NT),\hat{S}_{y,\tau}\right]$ represents the covariance of $\hat{X}(NT)$ and $\hat{S}_{y,\tau}$ which can be calculated as follows:

$$\begin{aligned}\mathrm{Cov}\left[\hat{X}(NT),\hat{S}_{y,\tau}\right] &= \frac{\beta\sqrt{J_x}\bar{\Phi}T}{2}\left[N\mathrm{Var}\left[\hat{X}_0\right] + \sum_{k=0}^{N-1}\langle\tilde{X}(NT)\tilde{X}(kT)\rangle\right] \\ &\approx \frac{\beta\sqrt{J_x}\bar{\Phi}\tau}{16}\left[1+\mathrm{Sinc}(\pi D)\right]^2\left[1+\frac{\tilde{\kappa}^2}{2}\frac{1-\mathrm{Sinc}(\pi D)}{1+\mathrm{Sinc}(\pi D)}\right]\end{aligned} \tag{4.32}$$

And the unconditional variance of $\hat{X}(NT)$ is

$$\begin{aligned}\mathrm{Var}\left[\hat{X}(NT)\right] &= \mathrm{Var}\left[\hat{X}_0\right] + \langle\tilde{X}(NT)\tilde{X}(NT)\rangle \\ &\approx \mathrm{Var}\left[\hat{X}_0\right]\left[1+\tilde{\kappa}^2\frac{1-\mathrm{Sinc}(\pi D)}{1+\mathrm{Sinc}(\pi D)}\right]\end{aligned} \tag{4.33}$$

We find that the squeezing is

$$\xi^2 = \frac{\mathrm{Var}\left[\hat{X}(NT)\right]\Big|_{\hat{S}_{y,\tau}}}{\mathrm{Var}\left[\hat{X}_0\right]} \approx 1+\tilde{\kappa}^2\frac{1-\mathrm{Sinc}(\pi D)}{1+\mathrm{Sinc}(\pi D)} - \frac{\tilde{\kappa}^2\left[1+\frac{\tilde{\kappa}^2}{2}\frac{1-\mathrm{Sinc}(\pi D)}{1+\mathrm{Sinc}(\pi D)}\right]^2}{1+\tilde{\kappa}^2+\frac{\tilde{\kappa}^4}{3}\frac{1-\mathrm{Sinc}(\pi D)}{1+\mathrm{Sinc}(\pi D)}} \tag{4.34}$$

In the limit of duty cycle $D=0$, we will have $\xi_0^2 = 1/(1+\tilde{\kappa}^2)$ in agreement with Equation 4.30.

So far, it has been assumed that the oscillator does not experience any decoherence. The presence of decoherence results in reduction of the realized squeezing[13]:

$$\xi^2 \approx \xi_0^2 + \eta_\tau \tag{4.35}$$

where η_τ scales with the decoherence events during the measurement time τ and depends on the decay mechanism. The decoherence can be linked to the light-probe, or it can be associated with coupling to a bath present even in the absence of the probe (e.g. coupling

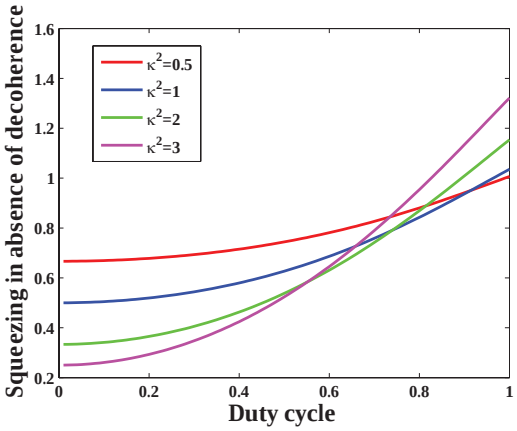

Fig. 4.7 squeezing dependence on duty cycle for different coupling strength κ^2 where decoherence is assumed to be negligible.

to the thermal phonon bath of a mechanical oscillator, or spin decay in the dark for a spin oscillator). In [29] exact relations for the probe induced decoherence and associated noise have been derived for the case of a spin oscillator. It is shown there that the probe induced noise can be written

$$\eta_\tau = h\frac{\tilde{\kappa}^2}{d} \tag{4.36}$$

where h is a numerical factor of order unity that depends on the probe polarization and the light-atom detuning, and $d = n_A\sigma_0 l$ is the optical depth on resonance, with n_A being the atomic density, σ_0 the absorption cross section on resonance and l the length of the cell.

4.3.3 Experimental realization

To study the generation of spin-squeezed states, two QND pulses are employed as shown in Figure 4.8: the first provides information about the oscillator observable $\hat{x} = \hat{J}_z/\sqrt{J_x}$, and the second pulse evaluates the observable variance conditioned on the first measurement. The exponential falling mode function $f(t) = e^{-\gamma t}$ is used to assess the measured noise of the second pulse, while the first pulse measurement is defined with a rising mode $f(t) = e^{+\gamma t}$, which is similar to the situation of writing and reading process where the falling (rising) mode is used to moderate the effect of decoherence which reduces the correlation between the pulses. Thus the first measurement result is given by

$$\hat{Q}_A = \sqrt{\frac{4\gamma}{e^{2\gamma T_A}-1}}\int_0^{T_A} dt\hat{S}_y^{out}e^{\gamma t}\cos(\Omega t), \tag{4.37}$$

and the second measurement result is defined as

$$\hat{Q}_B = \sqrt{\frac{4\gamma}{1-e^{-2\gamma T_B}}} \int_{T_A}^{T_A+T_B} dt \hat{S}_y^{out} e^{-\gamma t} \cos(\Omega t), \tag{4.38}$$

where T_A and T_B are the durations of two successive pulses, respectively. With the sub-

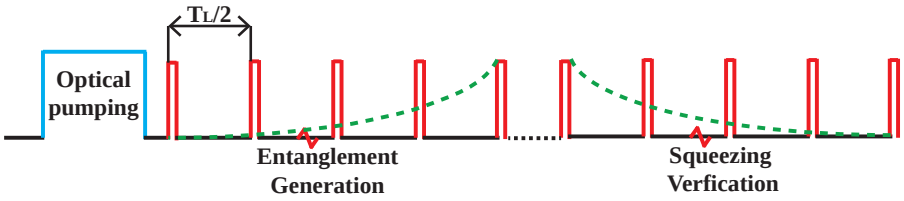

Fig. 4.8 Pulse sequence for generation and demonstration of conditional spin-squeezing by stroboscopic backaction evading measurement.

straction of the photon shot noise for the same pulse duration from the measured noise, the measured spin noise normalized into photon shot noise unit can be written as

$$\begin{aligned} \mathrm{Var}(\hat{x}_{m,A}) &= [\frac{\mathrm{Var}(\hat{Q}_A)}{PSN_A} - 1], \\ \mathrm{Var}(\hat{x}_{m,B}) &= [\frac{\mathrm{Var}(\hat{Q}_B)}{PSN_B} - 1], \end{aligned} \tag{4.39}$$

and furthermore the conditional variance is given by

$$\mathrm{Var}[\hat{x}_{m,B} \mid \hat{x}_{m,A}] = [\frac{\mathrm{Var}[\hat{Q}_B \mid \hat{Q}_A]}{PSN_B} - 1] = [\frac{\mathrm{Var}(\hat{Q}_B)}{PSN_B} - \frac{\mathrm{Cov}^2[\hat{Q}_B, \hat{Q}_A]}{PSN_B \mathrm{Var}(\hat{Q}_A)} - 1] \tag{4.40}$$

4.3.4 Results

In Figure 4.9 the oscillator noise in the first and second pulse, conditionally and unconditionally to the first measurement, are plotted as a function of the number of photons in the first pulse $N_{ph,A}$. In the experiment, the probe power averaged over an oscillator period is maintained constant and the duration of the first pulse T_A is varied. The duration of the second pulse is fixed to 0.5ms, which corresponds to $\sim 27 \times 10^7$ photons. The expected noise for CSS state of atomic ensemble (denoted by the subscript 0) is also plotted for comparison. Due to the correlation between the first and the second pulse, the conditional variance of the second pulse is significantly reduced below the imprecision in the CSS state, leading to squeezing. The data in Figure 4.9 indicate an additional squeezing mechanism unrelated to the information gain by measurement, since the unconditional noise for both the first and

second pulse drops below the ground state uncertainty. This kind of squeezing is due to the second-rank tensor polarizability dynamics. In Figure 4.10 the conditional noise is eval-

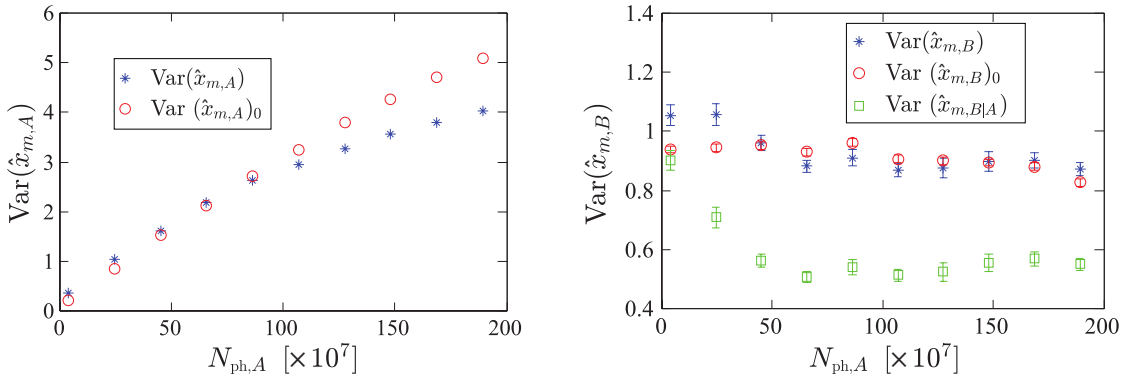

Fig. 4.9 (a) Measured noise (Var($\hat{x}_{m,A}$)) and expected noise in the oscillator ground state (Var($\hat{x}_{m,A}$)$_0$) as a function of the number of photons $N_{ph,A}$; (b) Comparison of expected ground state noise (Var($\hat{x}_{m,B}$)$_0$) with unconditional and conditional to the first pulse measured noises (Var($\hat{x}_{m,B}$) and Var($\hat{x}_{m,A}$)$_0$ respectively) as a function of the number of photons in the first pulse.

uated with respect to the measured unconditional imprecision. A comparison of the data in Figure 4.10 with those in Figure 4.9 indicates that the realized degree of squeezing is dominated by the information gain through the QND measurement.

In evaluating the squeezing degree, the measured variance is normalized to the macroscopic spin component J_x at the end of the first pulse: $\tilde{\xi}^2 = \mathrm{Var}[\hat{x}_{m,B} \mid \hat{x}_{m,A}]/[\mathrm{Var}(\hat{x}_{m,B}) f_d]$, where $f_d = J_x(T_A)/(4N_A)$ accounts for the reduction of the mean spin during the first measurement. The reduction of the mean spin J_x is characterized by an independent measurement of the response to an external coherent perturbation that was mentioned in Chapter3. The probe pulse of duration T_A, applied after the optical pumping phase, is followed by a resonant RF excitation pulse, much shorter than the decoherence time, and the response, which is proportional to the mean spin J_x, is recorded. In Figure 4.10(b) the demonstrated squeezing according to the Wineland criterion is plotted as a function of $N_{ph,A}$. The Wineland squeezing evaluates the effect of noise suppression in spectroscopic sensitivity: $\xi_W^2 = \mathrm{Var}[\hat{x}_{m,B} \mid \hat{x}_{m,A}]/[\mathrm{Var}(\hat{x}_m)_0 f_d^2]$. The data show that the created squeezed state offers the possibility of enhanced magnetic field measurement below the ground state uncertainty.

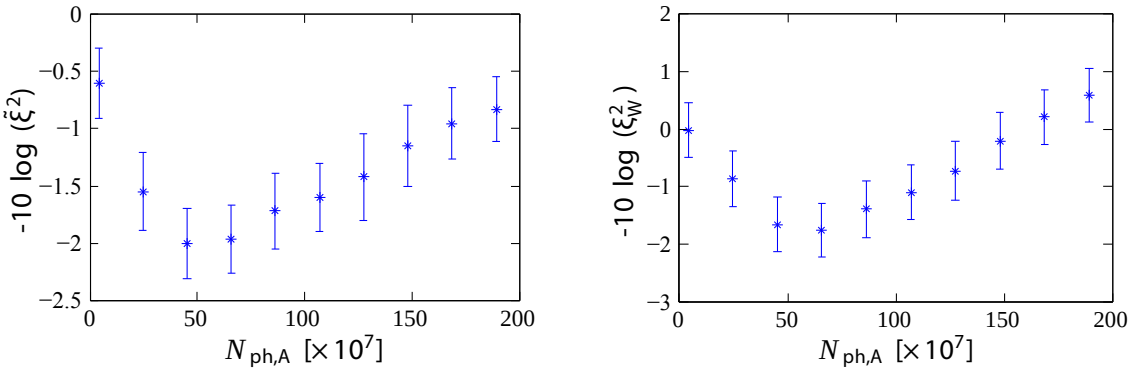

Fig. 4.10 (a) Uncertainty reduction of the oscillator position by using the information gained by a QND measurement. (b) Demonstrated squeezing according to the Wineland criterion, which quantifies the spectroscopic sensitivity enhancement with respect to the sensitivity in the ground state of the oscillator.

4.4 Conclusion and outlook

In summary, we have experimentally developed the quantum backaction evading measurement of one quadrature of collective spin components by stroboscopically modulating the intensity of probe beam at twice Larmor frequency. The collective spin of an atomic ensemble precessing in magnetic field is coupled to the optical mode of a cavity, and the cavity output field detected with polarization homodyne detection serves as the meter. Furthermore, a spin-squeezed state conditioned on the light-polarization measurement with 2.2 ± 0.3dB noise reduction below the spin projection noise limit for the measured quadrature has been demonstrated. Compared to the previous attempts where the reduction in the backaction noise was demonstrated but not the spin-squeezed state[70], the requirement of sufficient strength of the QND measurement with respect to the decoherence caused by the environment is satisfied by placing the atomic ensemble into an optical cavity, and keeping the spins into a spin-protecting environment. The demonstrated squeezing holds promise for metrological advantage in quantum sensing which will be shown in the next chapter.

The effect of the optical cavity will be discussed in the following chapter. It is found that the optimal squeezing $\xi^2_{opt} \propto 1/\sqrt{\mathfrak{F}}$ with the cavity finesse of $\mathfrak{F}$ can be achieved with an impedance matched cavity with the output coupler transmission $T_{out} \approx l_{cav}$ where l_{cav} is the round-trip intensity loss. Currently, the losses are limited from the single-pass loss in the cell windows which is 6.5% at present due to the deterioration of the anti-reflection coating when the windows are attached, therefore, by improving the windows attaching procedure we expect this value to get smaller by a factor of $3 \sim 4$ resulting in a stronger

spin squeezing above 5dB. We are now trying to improve this value by using the CO_2 laser bonding technology, and have achieved the single-pass loss about 2%, and we hope this property can survive after injecting the anti-relaxation coating material and Cesium gas.

Chapter 5

Cavity enhanced atomic magnetometer beyond the quantum noise limit

5.1 Introduction

In this chapter we describe the "Quantum noise limited cavity-enhanced radio-frequency atomic magnetometer" experiment. Atomic magnetometry has great potential to be used in many areas of research and technology, including biomedicine, geophysics, space exploration, navigation, unexploded ordnance, chemistry, and fundamental physics[71]. Optically probed, spin-polarized atomic ensembles have achieved sensitivities comparable or even surpassing superconducting quantum interference devices[72] benefiting from the advent of reliable diode lasers and the production of dense atomic vapors with long ground-state relaxation times. Additionally, removing the requirement of cryogenic cooling makes the atomic magnetometers easier to be miniaturized. Small-sized ensembles not only offer the possibility of sensing with high spatial resolution, but also reduce the sensitivity to field gradients, especially in the the small-sized anti-relaxation coated vapor cell. Also, miniature sensors are attractive for scalability (putting many sensor together if one wants to have a network).

A key parameter that determines the sensitivity and the efficiency of quantum protocol is the optical depth of the ensembles, which is a linear function of atomic density. In order to obtain a higher density in the single-pass scheme, the heating procedure is typically implemented. However, as mentioned in Chapter 3, most of the anti-relaxation coatings can not bear temperatures higher than $80^{\circ}C$, and after some point spin-exchange collisions between alkali atoms can become the dominant relaxation mechanism.. Although spin-exchange relaxation-free (SREF) magnetometer was developed to overcome this effect, the

limited magnetic-field range sets a fundamental obstacle to the range of this technology. Recently, a multi-pass approach has been applied to atomic magnetometry in order to increase the interaction volume[73], however, the requirement of sizeable atomic ensembles for this multi-pass approach rules out the possibility of detecting the magnetic field with high spatial resolution. In the work present in this chapter, micro-fabricated Cs vapor cell coupled into an optical cavity is used as the atomic ensemble to enhance the optical depth.

Another key parameter is the spin-relaxation time that is limited by several mechanisms, one of the most important being depolarization caused by collisions with the cell walls that enclose the atomic vapor. At present there exist two methods with different mechanisms to suppress this effect and elongate the spin coherence time (called spin lifetime): one is to use the buffer gas to slow the atomic diffusion to the wall, and the other is to deposit a special chemical layer onto the inner surface of the cell. They have the different advantages in the applications which can be found in Chapter 2. An alkene coating deposited at the inner cell walls of our mirocells dramatically suppresses spin-relaxation due to the wall collisions, resulting in longitudinal spin lifetime $T_1 \approx 17$ms and transverse spin lifetime $T_2 \approx 10$ms in the absence of light fields.

As discussed in[45], the Heisenberg uncertainty sets the fundamental limits on the best sensitivity that can be achieved in the optical magnetometer based on the interaction between light and atoms. There are three fundamental noise sources that could potentially limit the precision of the magnetic field estimation: the shot noise of the detected probe light field, the spin projection noise associated with the quantum state of the ensemble, and the back-action noise of the quantum probe. In this chapter, by using QND and backaction evading measurement we demonstrate a quantum noise limited radio-frequency atomic magnetometer, and furthermore, an improvement of the sensitivity for broadband magnetometry beyond the projection noise limit by implementing conditional spin squeezing.

5.2 Quantum noise limited RF magnetometer

5.2.1 A pulsed RF magnetometer

In the radio-frequency (rf) atomic-optical magnetometry, a polarized spin ensemble is prepared by optical pumping in the presence of a static magnetic field, which sets the atomic Larmor frequency (Figure 5.2). A transverse rf magnetic field resonant with the atomic Larmor frequency causes the spin ensemble to precess and the angle of precession is proportional to the rf magnetic field. The spin dynamics are monitored with a weak off-resonant linearly polarized probe beam. As the probe beam travels through the atomic vapor, its plane

of polarization rotates by an angle proportional to the spin component along the propagation direction according to the Faraday paramagnetic effect.

Consider an atomic ensemble with N_A fully polarized atoms in a state of magnetic quantum number $m_F = F$ along quantization axis x resulting in a collective spin component J_x with the length of FN_A, and two small transverse spin components $\hat{J}_y$ and $\hat{J}_z$, which can be viewed as quantum variables satisfying Heisenberg uncertainty relation $\mathrm{Var}(\hat{J}_y) \cdot \mathrm{Var}(\hat{J}_z) \geq J_x/2$. The spin $\vec{J}$ rotation in $y-z$ plane responding to an RF magnetic pulse at Larmor frequency along the z direction can be given as follows according to Equation 3.8

$$\langle J_z \rangle = \Omega/B \cdot B_{\mathrm{rf}} J_x T_1 T_2 \frac{[e^{-T/T_1} - e^{-T/T_2}]}{2(T_1 - T_2)}, \tag{5.1}$$

where $\Omega/2\pi$ is the Larmor frequency of spin $\vec{J}$ precession in a DC magnetic field of B along x axis and $\Omega/B = g_F \mu_B/\hbar = 2.2 \times 10^{10} \mathrm{rad}/(\sec \cdot \text{ Tesla})$ for cesium, while T_2 is the spin decoherence time during the RF pulse where this coherence time equals the decay time in the in the dark and T is the duration of the RF pulse. And then by measuring the polarization rotation of the probe light that interacts with the atomic spins, the spin information can be extracted from the difference of photocurrents in the balanced polarimetry output. With the assumption of large laser blue detuning the input-output relation in the rotating frame can be written as

$$\begin{aligned}
\hat{S}_y^{out}(t) &= \hat{S}_y^{in}(t) + aS_x(\hat{J'}_y(t)\sin(\Omega_L t) + \hat{J'}_z(t)\cos(\Omega_L t)), \\
\hat{S}_z^{out}(t) &= \hat{S}_z^{in}(t), \\
\hat{J'}_y(t) &= \hat{J'}_y(0) + \int_0^t aJ_x \hat{S}_z^{in}(t')\cos(\Omega_L t')dt', \\
\hat{J'}_z(t) &= \hat{J'}_z(0) - \int_0^t aJ_x \hat{S}_z^{in}(t')\sin(\Omega_L t')dt',
\end{aligned}$$

5.2.2 Quantum noise limited RF magnetometer based on backaction evasion measurement

Experimentally, the Stokes component $\hat{S}_y$ that characterizes the linear polarization in the $\pm 45^o$ basis is measured in a balanced polarimetry scheme. The cosine and sine components at the Larmor frequency are extracted with a lock-in amplifier, and are weighted with an exponentially decaying mode function. The relevant observable after measuring time T is then: $\hat{S}_{y,c} \propto \int_0^T dt \hat{S}_y(t) e^{-\gamma t} \cos \Omega_L t$, where γ is the decay rate of the transverse spin. It can

then be shown that[35]:

$$\hat{S}^{out}_{y,c} = \hat{S}^{in}_{y,c} + \bar{\kappa}\sqrt{\frac{S_x}{J_x}}\hat{J}^{in}_z - \frac{\bar{\kappa}^2}{2}[\hat{S}^{in}_{z,s} + \frac{\hat{S}^{in}_{z,s1}}{\sqrt{3}}], \tag{5.3}$$

where $\bar{\kappa} = a/2\sqrt{N_{ph}FN_a}$ with $S_x = N_{ph}/2$ and $J_x = FN_a$ while $\hat{S}_{z,s1} \propto \int_0^T \hat{S}_z(t)\sin(\Omega t)(T/2 - t)dt$. With the assumption of shot noise limited input light field and collective atomic spins in the CSS state, i.e. $\mathrm{Var}(\hat{S}^{in}_{y,c}) = \mathrm{Var}(\hat{S}^{in}_{z,s}) = \mathrm{Var}(\hat{S}^{in}_{z,s1}) = S_x/2 = N_{ph}/4$ and $\mathrm{Var}(\hat{J}^{in}_z) = J_x/2$, the variance of $\mathrm{Var}(\hat{S}^{out}_{y,c})$ is given by

$$\mathrm{Var}(\hat{S}^{out}_{y,c}) = \frac{S_x}{2}[1 + \bar{\kappa}^2 + \frac{\bar{\kappa}^4}{3}] = \frac{N_{ph}}{4}[1 + \bar{\kappa}^2 + \frac{\bar{\kappa}^4}{3}] \tag{5.4}$$

As discussed in Chapter 4, there are three terms contributing in the total noise: the photon shot noise, spin projection noise and the backaction noise. Because of the vacuum input of light field which means $\langle\hat{S}^{in}_y\rangle = \langle\hat{S}^{in}_z\rangle = 0$. When an applied rf magnetic pulse has initially created a non-zero spin-component$\langle\hat{J}^{in}_z\rangle \neq 0$ as described in Equation 5.1, the measured magnetometer signal can be written as

$$\langle\hat{S}^{out}_{y,c}(t)\rangle = a \cdot S_x\langle\hat{J}_z(t)\rangle, \tag{5.5}$$

As shown in the equations above, the signal grows linearly with $\bar{\kappa}$, and the noise grows as $\sqrt{1 + \bar{\kappa}^2 + \bar{\kappa}^4/3}$, therefore, neglecting the decoherence from the spontaneous emission the magnetic sensitivity $\delta B_{rf} \propto 1/SNR \propto \sqrt{1 + \bar{\kappa}^2 + \bar{\kappa}^4/3}/\bar{\kappa}$. The red curve in Figure 5.1 shows how the SNR depends on coupling strength $\bar{\kappa}$. According to the calculation, there exist an optimal strength $\bar{\kappa}^2_{opt} = \sqrt{3}$ where the signal to noise ration is maximized.

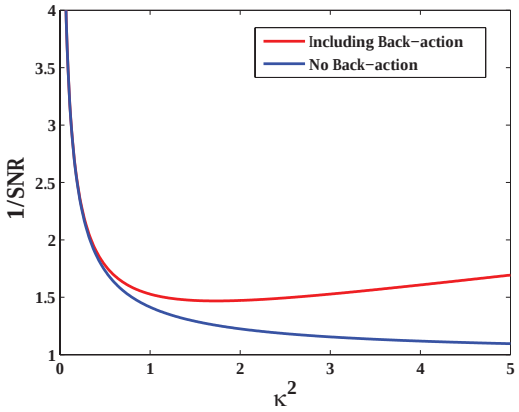

Fig. 5.1 1/SNR for the different magnetometers as a function of the coupling strength $\bar{\kappa}$.

However, if implementing the backacion evading measurement, the optimal sensitivity can be improved by a factor of ~ 1.47 that is also presented in Figure 5.1 as the blue curve. As demonstrated in Chapter 4, backaction evading measurement can be realized by stroboscopically pulsing the probe beam at twice the frequency of Larmor spin precession. The measurement record $\hat{S}^{out}_{y,T} = \int_0^T dt \hat{S}_y(t)\cos(\Omega t) f(t)$ (f(t) is the mode function as described in Chapter 4) the $\cos(\Omega t)$ Fourier component of the photocurrent integrated over the pulse length can be written as

$$Var(\hat{S}^{out}_{y,T}) \approx \frac{\bar{\Phi}T}{8}\left[1+\mathrm{Sinc}(\pi D)\right]\left[1+\tilde{\kappa}^2+\frac{\tilde{\kappa}^4}{3}\frac{1-\mathrm{Sinc}(\pi D)}{1+\mathrm{Sinc}(\pi D)}\right]$$

where the effective coupling constant is

$$\tilde{\kappa}^2 = \frac{1}{4}a^2 J_x \bar{\Phi} T\left[1+\mathrm{Sinc}(\pi D)\right],$$

where D is the duty cycle of the probe and $\bar{\Phi}$ is the average photon flux related to the number of photon: $N_{ph} = \bar{\Phi}T$. In the limit of $D = 1$ for the continuous probing, $\tilde{\kappa}^2 = \frac{1}{4}a^2 J_x \bar{\Phi} T$ which is exactly the expression of $\bar{\kappa}^2$ presented above. However, in the opposite limit $D \to 0$, the backaction coupling constant $C = \frac{1-\mathrm{Sinc}(\pi D)}{1+\mathrm{Sinc}(\pi D)}$ tends to zero. And the variance of the measured signal is

$$Var(\hat{S}^{out}_{y,T}) \approx \frac{\bar{\Phi}T}{4}\left[1+\tilde{\kappa}^2\right], \tag{5.6}$$

with the coupling strength $\tilde{\kappa}^2 = \frac{1}{2}a^2 J_x N_{ph}$. The same result has been achieved by using two oppositely oriented ensembles where the backaction noise on the two ensembles cancel each other[55]. If one could reach the limit $\tilde{\kappa}^2 \to \infty$ the noise contribution from the light field would be negligible and the measurement would behave as the blue curve in Figure 5.1, assuming no decoherence. However, decoherence from the spontaneous emission $\propto \tilde{\kappa}^4$ gets comparable to other noise sources at some point which will be discussed later.

5.2.3 Experimental realization

The experimental scheme is shown in Figure 5.2. We adopted a measuring scheme with separate intervals of quantum state preparation (optical pumping), spin evolution in the presence of the RF magnetic field, and state characterization with a probe pulse[55]. In this mode of operation the magnetometer response to the RF field is limited by the spin coherence lifetime in the absence of optical pumping and probing light fields. The probe light injected into the cavity is linearly polarized orthogonal to the direction of the atomic spin whose intensity is stroboscopically modulated at twice the Larmor frequency with the

duty cycle $\sim 15\%$. In this geometry the cross polarization scattering between the strong coherent optical polarization mode and the orthogonal quantum mode occurs only due to the coherent Faraday interaction. The Stokes component $\hat{S}_y$ that characterizes the linear polarization in the $\pm 45^o$ basis is measured in a balanced polarimetry scheme. The cosine and sine components at the Larmor frequency are extracted with a lock-in amplifier, and are weighted with an exponentially decaying mode function, which underweighs the measurement at late times when the probe-induced destruction of the spin state is stronger. The relevant observable after measuring time T is then: $\hat{S}_{y,c} \propto \int_0^T dt \hat{S}_y(t) e^{-\gamma t} \cos(\Omega t)$, where γ is the decay rate of the transverse spin, including incoherent and coherent processes[55], and Ω is the Larmor frequency. Although the tensor interaction between light and atoms has

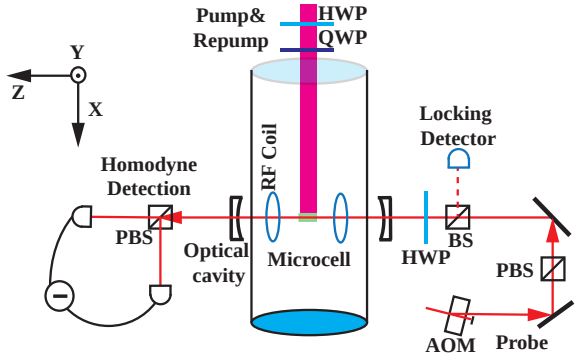

(a)

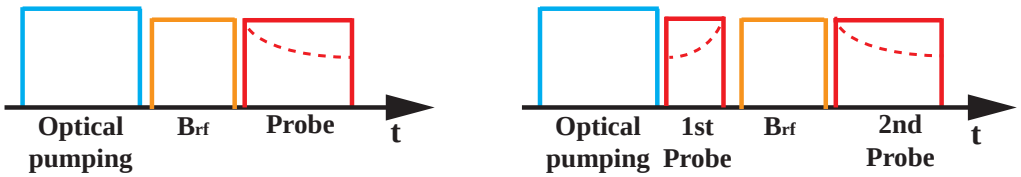

(b) (c)

Fig. 5.2 (a) Outline of experimental setup for cavity enhanced projection-noise limited atomic magnetometry. AOM: Acousto-optic modulator; PBS: Polarization beamsplitter; BS: Beam splitter; HWP: Half waveplate; QWP: quarter waveplate. The antirelaxation coated micro-channel filled with Cesium atoms is aligned with the TEM_{00} mode of the optical cavity. The atomic cell is inclosed in the magnetic shields with 3-layer μ metal. The atoms are polarized along the quantization axis $\vec{x}$ by optical pumping in the and the dc magnetic field $B_{\vec{x}}$. A pulse of $\vec{B}_{\rm rf}$ field at the Larmor frequency Ω to be measured is applied orthogonally to the $\vec{B}$ field. The polarization rotation of the top-hat shaped probe beam pulse is detected by the polarization homodyning. The lock-in amplifier measures the $cos(\Omega t)$ and $sin(\Omega t)$ components of the photocurrent. (b)Pulse sequence for the quantum noise limited magnetometer. The temporal mode function for the probe is shown with a dashed red curve.(c)Pulse sequence for the spin squeezing-assisted magnetometer.

been used to enhance the magnetometer sensitivity[55], the magnetometer data presented in this work were taken at large enough probe detuning ($\Delta = 1.6$GHz blue detuned from the $F = 4 \mapsto F' = 5$ D2 transition) so that we can keep the vector interaction only, and neglect the second rank tensor polarizability.

5.2.4 Results

Atomic density

As mentioned in the beginning of this chapter, one way to improve magnetometer sensitivity is to increase the density of alkali-metal atoms. The heating is realized by a twisted wire with high resistance wounded around the aluminum cylinder where most of the magnetic coils are attached. By adding current on this wire a stable temperature can be established inside the cylinder. Figure 5.3 presents the spin response to a fixed RF excitation as a function of the environment temperature. Since the atomic ensemble is prepared in the highly oriented state (98% spin orientation) and the photon number is fixed during this measurement, the spin response is linearly proportional to the number of atoms as shown in Equation 5.1. In Figure 5.4, the experimental results for the RF magnetic field sensitivity

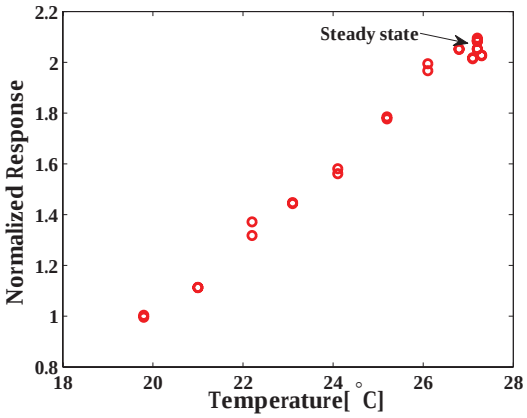

Fig. 5.3 Normalized spin response to the fixed RF excitation as a function of the environment temperature.

as a function of the probe power are plotted when the duty cycle of the probe pulse is 100% and the backaction coupling constant $C = 1$. In the measurement the spin vector is kicked by applying a 8ms RF magnetic pulse at the Larmor frequency of 380kHz with the RMS amplitude of $B_{rf} = 243$pT and the resulted non-zero mean value is then mapped onto the light field$\hat{S}_y^{out}$. The geometric design and calibration of the magnetic system can be found in Appedix 1 and the corresponding measurement details can be found in [34]. Due to

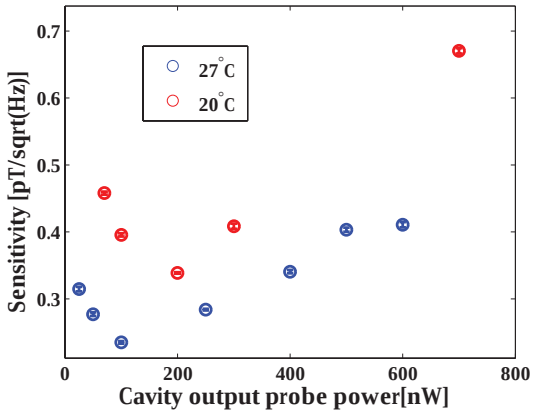

Fig. 5.4 Magnetic sensitivity versus cavity output probe power at $20^{\circ}C$ and $27^{\circ}C$. Since the duty cycle of the probe pulse is 100%, the backaction coupling constant is $C = 1$.

increasing the atomic density by a factor of ~ 2.2, the best sensitivity in the continuous probing scheme is improved from $338.7\text{fT}/\sqrt{\text{Hz}}$ to $235.0\text{fT}/\sqrt{\text{Hz}}$, a factor of 1.44, which is in agreement with the theoretical prediction of $B_{rf}^{sen} \propto 1/\sqrt{N_a}$.

Optimal duration of the RF magnetic pulse

The duration of the RF magnetic pulse chosen above is an optimal value depending on the magnetometer bandwidth $\delta_A = 1/T_2$. Let us simply look at the physical idea inside. When the initial spin state is prepared in the CSS state by optical pumping which corresponds to the minimal transverse spin variances $\text{Var}(\hat{J}_y) = \text{Var}(\hat{J}_z) = J_x/2$, the projection noise limited sensitivity to the magnetic field can be expressed as

$$\begin{aligned} B_{\text{sen}} &= B_{\min}\sqrt{T} \\ &= [\Omega/B\sqrt{FN_A/2}T_1T_2(e^{-T/T_1} - e^{-T/T_2})/[(T_1 - T_2)]]^{-1} \cdot \sqrt{T}. \end{aligned} \tag{5.7}$$

If assuming $T_1 \gg T_2$, PN-limited magnetic sensitivity in two extreme situations of the duration of rf pulse can be expressed as

$$B_{\text{sen}} \begin{cases} \approx [\Omega/B\sqrt{FN_A/2}]^{-1}\frac{1}{\sqrt{T}} & T \ll T_2 \\ \approx [\Omega/B\sqrt{FN_A/2}]^{-1}\frac{\sqrt{T}}{T_2} & T_2 \ll T \ll T_1 \end{cases} \tag{5.8}$$

In Figure 5.5, I plot the sensitivities calculated from these two extreme cases (blue curve represents the case for $T \ll T_2$, and violet curve gives the sensitivity for $T \gg T_2$), and also the theoretical prediction from Equation 5.7. Roughly speaking, when the duration of RF-pulse $T \approx T_2$ one can achieve the best sensitivity. Figure 5.6 gives the experimental

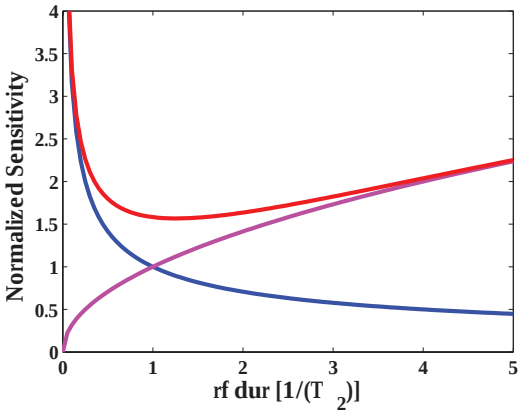

Fig. 5.5 Optimal duration of rf-pulse. Blue curve represents the case for $T \ll T_2$, and violet curve gives the sensitivity for $T \gg T_2$. The theoretical prediction from Equation 5.7 is presented as red curve.

demonstration with the optimal probe power of 200nW.

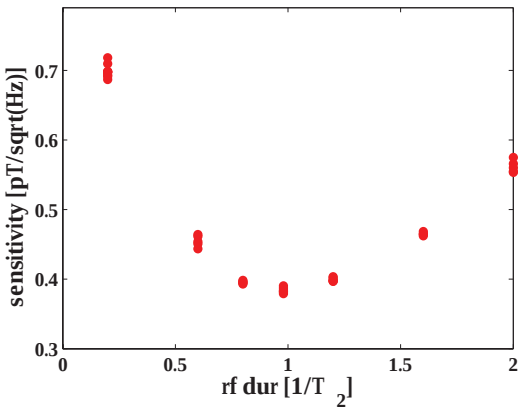

Fig. 5.6 Magnetic sensitivity versus the duration of RF pulse. Since the duty cycle of the probe pulse is 100%, the backaction coupling constant $C = 1$.

Quantum noise limited magnetometer

We now focus on the quantum noise limited RF magnetometer based on backaction evasion measurement. As described before by stroboscopically pulsing the probe beam at twice the frequency of Larmor spin precession, the backaction evading measurement can be realized. In this measurement, by tuning the phase of $\cos(\Omega t)$ component on the Lockin Amplifier, we can transfer the spin response signal into the $\cos(\Omega t)$ component of the measured light field $\hat{S}_y^{out}$. At the same time the phase between the synchronous intensity-modulated signal

and the RF-pulse signal should be optimized to reach the maximal response. Thus, the signal to noise ratio can be simply calculated as

$$\mathrm{SNR} = \frac{|\hat{S}_{y,c}^{out}|}{\sqrt{\mathrm{Var}(\hat{S}_{y,c}^{out})}}$$

In Figure 5.7, the measured sensitivities as a function of probe power for two protocols at $27^{\circ}C$ are plotted. As we expected, the best sensitivity is improved by a factor of 1.48, and also after some probe power the decoherence induced by spontaneous emission gets obvious which strong enough to change the trend of monotonically decreasing sensitivity and furthermore obstructs the realization of an ideal PN-limited magnetometer. However, the best sensitivity achieved here is $158 \pm 1.17\mathrm{fT}/\sqrt{\mathrm{Hz}}$.

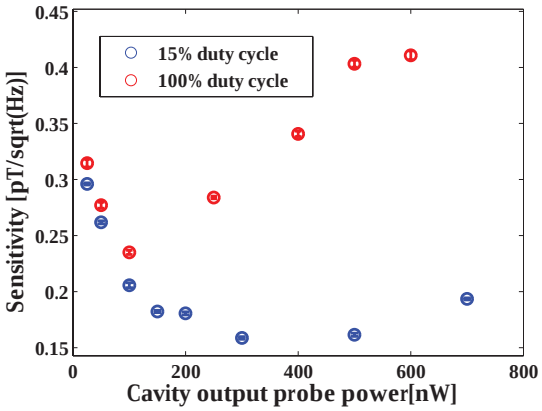

Fig. 5.7 Magnetic field sensitivity versus cavity output probe power at $27^{\circ}C$. The red circle shows the sensitivity when probe pulse is not modulated, while the blue circle presents the sensitivity when the probe beam is stroboscopically pulsed at twice the frequency of Larmor spin precession with 15% duty cycle. The measurement was performed at 380kHz with the optimized RF pulse duration of 8ms.

5.3 Magnetic sensitivity beyond the quantum noise limit by spin squeezing

5.3.1 Protocol

Having demonstrated the back action evading magnetometer and projection noise limited performance, we have been able to make one step further and overcome this limit by sandwiching the RF pulse between two back action evading measurements as shown in Figure

5.2c. As demonstrated in the previous work[21, 22, 74], a sufficiently strong quantum non-demolition (QND) measurement can generate a spin squeezed state (SSS) of the measured variable. In the context of magnetometry SSS generated by the first optical pulse is followed by the magnetic field pulse to be measured. The cycle is completed by the second optical pulse which measures the displacement of the SSS caused by the magnetic field. In[55] this approach was used for magnetometry with two atomic ensembles for which a light-matter interaction without stroboscopic modulation generates a two mode squeezed state. Here, we use the stroboscopic QND measurement of $\hat{J}_z$ to generate a SSS state and to realize the magnetometer beyond the quantum noise limit. Let us denote the variances of the first and second probe pulses as $Var(\hat{S}_y^1)$ and $Var(\hat{S}_y^2)$, respectively. The conditional variance of $\hat{S}_y^2$ expressed as $\mathrm{Var}(\hat{S}_y^2|\hat{S}_y^1) = \mathrm{Var}(\hat{S}_y^2) - \frac{\mathrm{Cov}^2(\hat{S}_y^1,\hat{S}_y^2)}{\mathrm{Var}(\hat{S}_y^1)}$, is reduced due to quantum correlation between the spin states probed by the two pulses. This noise reduction which leads to the improved sensitivity is dependent on the covariance of $\hat{S}_y^1$ and $\hat{S}_y^2$, $\mathrm{Cov}^2(\hat{S}_y^1,\hat{S}_y^2)$.

5.3.2 Experimental results

In Figure 5.8, we plot the magnetic sensitivity as a function of radio-frequency bandwidth, where we see an improvement of 13% due to employing the conditional SSS and this improvement vanishes when the RF-pulse duration reaches 3ms. The most pronounced improvement occurs at a higher bandwidth (shorter RF-pulse duration) due to the decoherence of the spin state between the two measurements.

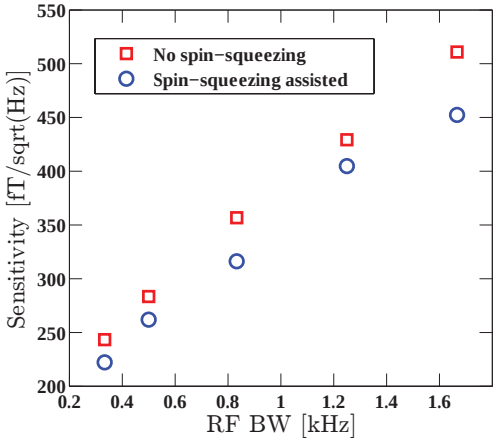

Fig. 5.8 Sensitivity for stroboscopic modulation and entanglement-assisted scheme. During the probe pulses, the average cavity output power is fixed at 100nW, with the interaction times of 1ms and 2ms,respectively.

5.4 Effect of optical cavity

As described in this thesis, a microcell coupled into an optical cavity is the key element of the experimental setup whose optical depth is enhanced by a factor of $2\mathfrak{F}/\pi$. Here I will explain the reason of introducing an optical resonator in detail. Let us denote the power transmission coefficients of the input and output couplers, the round trip intracavity losses, and atomic single pass absorption as $T_{1,c}$, $T_{2,c}$, l_{cav} and d_Δ, respectively. The cavity power transmission coefficient on resonance is $4T_{1,c}T_{2,c}/(T_{1,c}+T_{2,c}+l_{cav}+2d_\Delta)^2$. With the assumption of $2d_\Delta \ll T_{1,c}+T_{2,c}+l_{cav}$, this coefficient can be expended as $4T_{1,c}T_{2,c}/(T_{1,c}+T_{2,c}+l_{cav})^2\cdot(1-2\mathfrak{F}d_\Delta/\pi)$, where $\mathfrak{F}=2\pi/(T_{1,c}+T_{2,c}+l_{cav})$ is the cavity finesse. Clearly, the single pass atomic absorption d_Δ is enhanced by a factor of $2\mathfrak{F}/\pi$. From Kramers-Kronig relations the phase shift, and therefore the polarization rotation angle, is enhanced by the same factor. The input-output relations presented in Chapter 2 is modified by enhancing the light-matter coherent interaction by $2\mathfrak{F}/\pi$. If κ_0 is the coupling constant in the absence of cavity, then for the same number of detected photons in the pulse the cavity-enhanced coupling constant is $\kappa_{cav}=\frac{2\mathfrak{F}}{\pi}\kappa_0$.

When back-action noise exists, SNR $\propto \kappa/\sqrt{1+\kappa^2+\kappa^4/3}$ will always reach the upper bound when $\kappa^2=\sqrt{3}$ if we do not consider the spontaneous emission due to $d\gg 1$. In this sense, introducing the optical cavity cannot give a significant improvement on the magnetic field sensitivity except the reduction of decoherent process. We have done this comparison in the continuous magnetometer measurement using Microcell C7 with $T_2\sim 5$ms which gives the finesses of 10 when coupling into the optical cavity. ($R_1=99.97\%$ and $R_2=80\%$). As shown in Figure 5.9, with the help of optical cavity, we only gained an improvement of magnetic sensitivity by 6%.

In the case of the back-action evasion, the optical cavity can improve the sensitivity further, since in this case SNR $\propto \kappa/\sqrt{1+\kappa^2}$. In addition, with the presence of the optical cavity, the conditional spin squeezing can also be improved where the realized squeezing is limited by the noise due to decoherence events. The probe-induced decoherence noise is proportional to the intracavity light-power experienced by the atomic ensemble Pin, which is related to the power at the output of the cavity (P_{out}) through: $P_{out}=P_{in}(\frac{2}{T_{2c}}-1)$, where T_2 is the output mirror coupler power transmission. For a standing wave cavity, maximum squeezing is achieved for $T_{1c}\ll T_{2c}$, so that the quantum light field generated inside the cavity from the interaction with the atoms has very small losses to the unobserved direction. Assuming only probe-induced decoherence and for $T_{1c}\ll T_{2c}\ll 1$, ξ^2 can be written in the

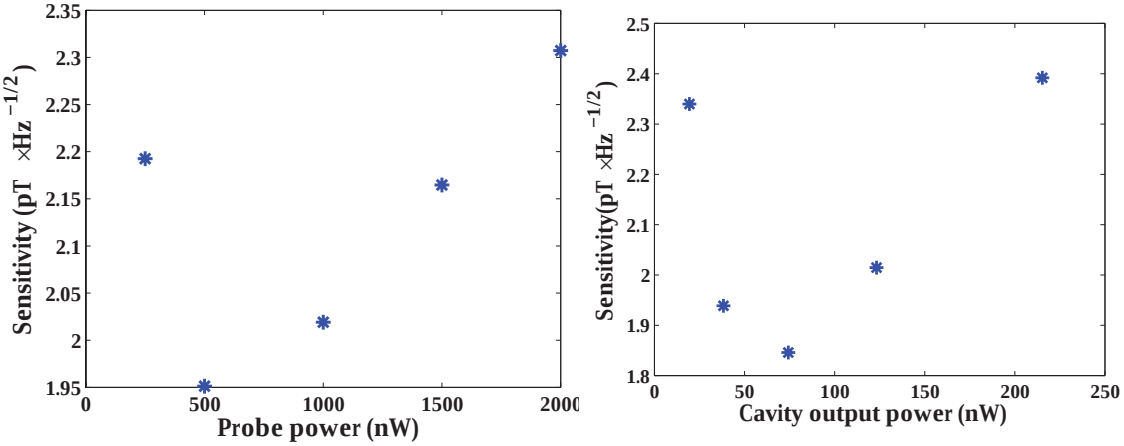

(a) (b)

Fig. 5.9 Magnetic sensitivity of Continuous RF magnetometer without optical cavity (a) and with optical cavity (b), respectively. Larmor frequency Ω:84.5kHz, and the spin orientation is above 90% by sending $59\mu W$ repump beam and $16\mu W$ pump beam.

form

$$\begin{aligned}\xi^2 &= \frac{1}{1+(2\mathfrak{F}/\pi)^2\kappa_0^2} + \eta_0\left(\frac{2}{T_{2c}} - 1\right) \\ &\approx \frac{1}{1+(2\mathfrak{F}/\pi)^2\kappa_0^2} + \eta_0\frac{\mathfrak{F}(T_{2c}+l_{cav})}{\pi T_{2c}}\end{aligned} \tag{5.9}$$

where η_0 is the decoherence noise due to the light-probe in the absence of the cavity for the same detected probe power.. For small but finite intracavity losses, optimizing with respect to the number of photons in the light pulse (κ_0) and the output coupler transmission, the squeezing is:

$$\xi_{opt}^2 \approx (2 - \sqrt{\frac{h}{(2\mathfrak{F}/\pi)d_0}})\sqrt{\frac{h}{(2\mathfrak{F}/\pi)d_0}} \approx \sqrt{\frac{h}{(\mathfrak{F}/2\pi)d_0}} \tag{5.10}$$

with the optimal $T_2^{opt} = l_{cav}$ and $\kappa_{0,opt}^2 = \frac{\sqrt{(d_0/h)(2\mathfrak{F}/\pi)}-1}{(2\mathfrak{F}/\pi)^2}$. However, the intensity transmission of the output coupler in the current setup is 20% which is a little bit higher than the intracavity loss 13%. Therefore, if we can match those two values in next step, we believe the spin squeezing can be improved.

5.5 Conclusion and outlook

In conclusion, we report a projection noise limited optical magnetometer at room temperature with an RF magnetic-field sensitivity of $158 \pm 1\text{fT}/\sqrt{\text{Hz}}$ and 2D spatial resolution of $300\mu\text{m}$. It utilizes a microfabricated Cs vapor cell with antirelaxation coating coupled into an optical cavity to enhance the light-atoms interaction. Combining the stroboscopic back-action evading measurement with the cavity enhanced interaction, we improve the sensitivity beyond the quantum noise limit by 13%. The room temperature quantum magnetometer described here may find applications in many fields, such as biological and medical sensing.

Chapter 6

Deterministic quantum teleportation between distant atomic objects

6.1 Introduction

In this chapter I describe the "Deterministic quantum teleportation between distant atomic objects" experiment. The results have been published in Nature Physics. As a key ingredient in quantum networks and one of the building blocks for quantum computation, quantum teleportation, originally introduced for discrete variables[1] and later adapted for continuous variables[75], denotes the transfer of a quantum mechanical state without the transmission of a physical system carrying this state. The first experimentally realized teleportation protocols employed light as the carrier of the quantum states[76, 77]. Also several protocols for atoms were realized, e.g. using two closely positioned ions [78] and later two ions in independent vacuum chambers separated by one meter[79]. Most protocols for distant atoms or atomic ensembles at the sending and receiving end are conditional in nature, such that either the measurement outcome determines the success of the protocol or a heralded entanglement generation is employed. Whereas probabilistic teleportation, in which entanglement is distributed by photon counting, is capable of reaching distances of many kilometres[80], the power of continuous-variable teleportation is that it succeeds deterministically in every attempt, that it is capable of teleporting complex quantum states[81] and that it can be used in universal quantum computation[82]. Here, we present an atomic teleportation experiment that works deterministically and on demand where a state transfer of the the spin state between two atomic ensemble of $N_A \approx 10^{11}$ Cesium atoms at room-temperature is realized.

6.2 Teleportation protocol

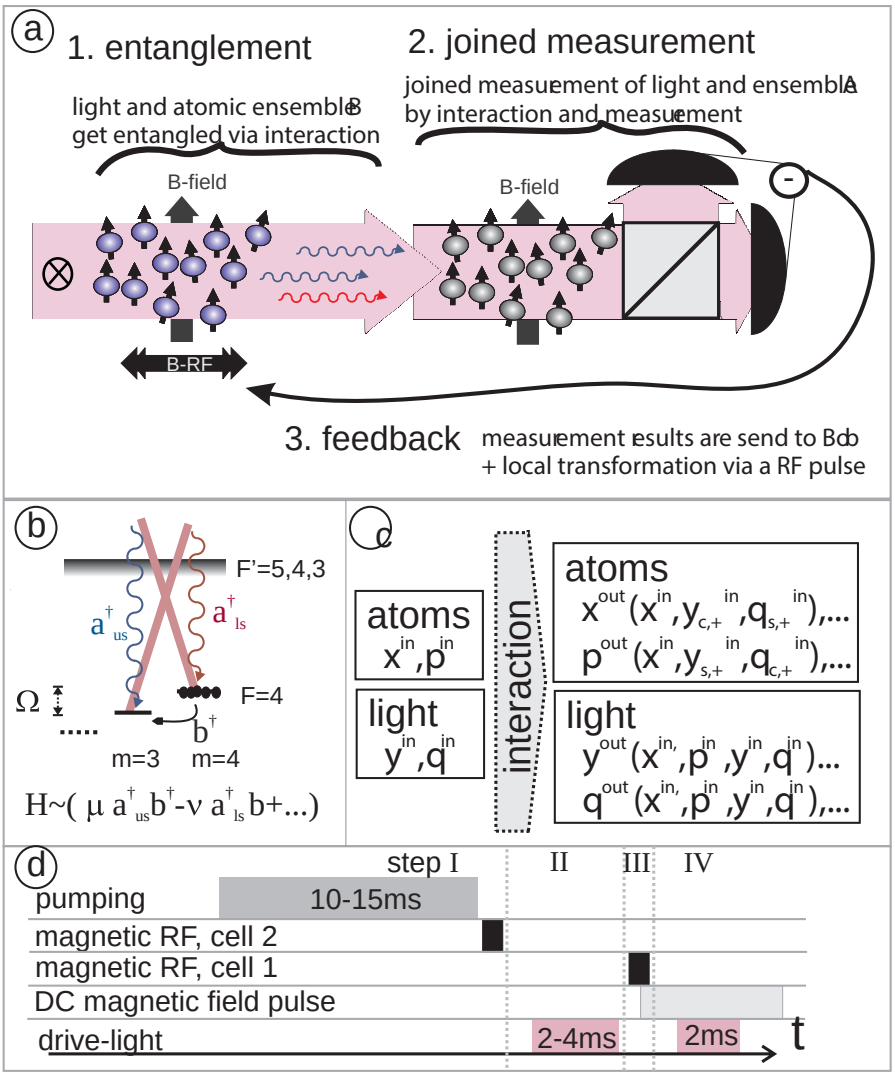

Fig. 6.1 The experimental layout. A strong driving pulse propagates first through ensemble B creating the modes $x_L = y'$, $p_L = q'$entangled with B and then through ensemble A whose state is to be teleported. Joint measurements on the modes y'' are performed using polarization homodyning. Teleportation is completed by classical communication of these results to B. See the text for further details. RF, radiofrequency. b, The level scheme and relevant transitions. Classical drive field (thick lines) and quantum fields forming the modes y;q (wavy lines) are shown. d, The time line of the experiment. I, preparation of the input state; II, entanglement and joint measurement; III, feedback; IV, read-out of the teleported state. In the (c) the effect of the interaction with this linear Hamiltonian H is depicted. We choose to consider the atomic operators in the rotating frame, so that they are not mixed in the interaction.

A standard teleportation scheme involving the three parties Alice, Bob and Charlie consists of the following three steps, which allow Alice to teleport a quantum state provided by Charlie to Bob. (i) Alice and Bob establish an entangled link, which is shared between the two remote parties. (ii) Alice performs a Bell measurement on her part of the entangled state shared with Bob and an unknown quantum state prepared by Charlie. (iii) Alice uses a classical channel to communicate the measurement outcome to Bob, who performs a local operation on his quantum state conditioned on Alice's result. In our experiment these two objects are an atomic ensemble at site B and a photonic wave packet generated by interaction of this ensemble with a driving light pulse (see Figure 6.1). The wave packet travels to site A, the location of the atomic ensemble whose state is to be teleported. This step establishes a quantum link between the two locations. Following the interaction of ensemble A and the wave packet, a measurement is performed on the transmitted light. The results of this measurement are communicated through a classical channel to site B, where they are fed back through local operations on the second entangled object, that is, ensemble B, thus completing the process of teleportation.

6.2.1 Generation and distribution of the Einstein-Podolsky-Rosen entangled state

As discussed in[83], EPR entangled state is required to establish the quantum channel between two stations involved in the quantum teleportation protocol which should satisfy a generic condition in the continuous-variable regime for Gaussian states as mentioned in terms of $\mathrm{Var}(\hat{X}_1-\hat{X}_2)+\mathrm{Var}(\hat{P}_1+\hat{P}_2)<2$ where the canonical variables follow the canonical commutation relation $[X_i,X_j]=0$ and $[X_i,P_j]=i\delta_{ij}$. In our scheme, an entangling interaction $\hat{a}^{\dagger}_{us}\hat{b}^{\dagger}+H.C.$ is taking place, where one atomic excitation $\hat{b}^{\dagger}=(\hat{x}_B+\hat{p}_B)/\sqrt{2}$ is accompanied by the creation of a photon $\hat{a}^{\dagger}_{us}$ in the upper sideband of the x-polarization mode. This kind of light-atom entanglement generation is discussed in detail in Chapter 2, and the full Hamiltonian can be written as

$$\begin{aligned}\hat{H}_{int} &= \frac{\hbar a}{2}\int_0^L dz[(\zeta^2+1)(\hat{a}_L\hat{b}^{\dagger}_A+\hat{a}^{\dagger}_L\hat{b}_A)-(1-\zeta^2)(\hat{a}^{\dagger}_L\hat{b}^{\dagger}_A+\hat{a}_L\hat{b}_A)]\\ &\propto [(\zeta^2+1)\hat{H}_{BS}-(1-\zeta^2)\hat{H}_{TMS}]\end{aligned}$$

where the normalized collective ground state spin operators in the rotating frame at Ω are $\hat{x}_{A,B}=\hat{J}_y^{A,B}/\sqrt{J_x}$ and $\hat{p}_{A,B}=\hat{J}_z^{A,B}/\sqrt{J_x}$ which follow the canonical commutation relation $[\hat{x}_{A,B},\hat{p}_{A,B}]=i$ with variances $\mathrm{var}(\hat{x})=\mathrm{var}(\hat{p})=1/2$ for the CSS, while the corresponding variables for the upper sideband light mode are defined in Equation 2.51. From the Hamilto-

nian above, it is found that the weight coefficients are related to the ratio between vector and tensor coupling strength as $\zeta^2 = \frac{14a_2}{a_1}$. In other words, the relative strengths of two different interaction can be changed by detuning the laser frequency. The satisfaction of condition $Var(\hat{X}_L^{up} - \hat{x}_B^{out}) + Var(\hat{P}_L^{up} + \hat{p}_B^{out}) < 2$ proves the establishment of entanglement between an atomic ensemble at site B and the light field which is then sent to Alice at site A.

6.2.2 Bell measurement at Alice's station

The spin information to be teleported of ensemble A is displaced with mean values $\langle x_A \rangle$ and $\langle p_A \rangle$ by a weak radiofrequency magnetic field pulse of frequency corresponding to the creation of a coherent superposition of electronic ground states $m_F = 3$ and $m_F = 4$. The following interaction between light field and atomic ensemble A at site A leads to partial mapping of its state onto light and is followed by the Bell measurements on the light modes of the upper and lower sidebands performed using polarization homodyning with the driving light acting as the local oscillator yielding $\hat{X}_L^c = \frac{1}{\sqrt{2}}(\hat{x}^{up} + \hat{x}^{low})$ and $\hat{X}_L^s = \frac{1}{\sqrt{2}}(\hat{p}^{low} - \hat{x}^{up})$. The measurements of $\hat{X}_L^c$ and $\hat{X}_L^s$ serve as the joint measurement of ensemble A and the light coming from site B. As mentioned before in order to compensate the atomic decay, an exponential mode function is applied, and thus the read-out mode is $\hat{x}_{c/s,-} \propto \int_0^T dt \hat{x}(t) e^{-\gamma t} \cos / \sin(\Omega t)$ where T is the pulse duration and γ is the decay rate of the atomic state. The completed input-output relations about $\hat{x}_{c/s,-}$ including the tensor interaction can be found in Equation 2.38 or [32].

6.2.3 Classical communication and feedback at Bob's station

The teleportation protocol is completed by sending the measurement results $\hat{x}_{c/s,-}^{out}$ through a classical link to the site B with gain $g_x = g_p = g$ where spin rotations in the y-z plane conditioned on these results are performed using phase- and amplitude controlled radiofrequency magnetic field pulses at frequency Ω. The final canonical variable of atomic ensemble B is[32]

$$\begin{aligned} \begin{pmatrix} \hat{x}_B^{\text{tele}} \\ \hat{p}_B^{\text{tele}} \end{pmatrix} = \bar{C}_B \begin{pmatrix} \hat{x}_B^{in} \\ \hat{p}_B^{in} \end{pmatrix} + \bar{C}_A \begin{pmatrix} \hat{x}_A^{in} \\ \hat{p}_A^{in} \end{pmatrix} + \bar{C}_{A,N} \begin{pmatrix} \hat{F}_{xA}^{in} \\ \hat{p}_{pA}^{in} \end{pmatrix} \\ + \bar{C}_{B,N} \begin{pmatrix} \hat{F}_{xA}^{in} \\ \hat{p}_{pA}^{in} \end{pmatrix} + \bar{C}_x \begin{pmatrix} \hat{x}_{s,f_x}^{in} \\ \hat{x}_{c,f_x}^{in} \end{pmatrix} + \bar{C}_p \begin{pmatrix} \hat{p}_{c,f_p}^{in} \\ -\hat{p}_{s,f_p}^{in} \end{pmatrix}, \end{aligned} \tag{6.1}$$

where the modes appearing in this equation are defined as

$$\begin{aligned}
\bar{f}_{N,B} &= \sqrt{2\gamma_{extra}}[e^{-\gamma(T-t)} + \frac{\sqrt{2\gamma_s\gamma}g}{\zeta\sqrt{1-e^{-2\gamma T}}}\int_t^T d\tau e^{-\gamma(2\tau-t)}[1-2\gamma_s(\tau-t)]],\\
\bar{f}_{N,A} &= \frac{\sqrt{\gamma_s\gamma_{extra}}g}{\zeta\sqrt{\gamma}\sqrt{1-e^{-2\gamma T}}}(e^{-\gamma t} - e^{-2\gamma T+\gamma t}),\\
\bar{f}_x &= -\zeta\sqrt{2\gamma_s}e^{-\gamma(T-t)} + \frac{\gamma_s g}{\sqrt{\gamma}\sqrt{1-e^{-2\gamma T}}}\frac{2\gamma}{\gamma_s}e^{-\gamma t}\\
&\quad - \frac{\gamma_s g}{\sqrt{\gamma}\sqrt{1-e^{-2\gamma T}}}[e^{-\gamma t}(2-\frac{\gamma_s}{\gamma}) - e^{-2\gamma T+\gamma t}(2-\frac{\gamma_s}{\gamma}-2\gamma_s(T-t))],\\
\bar{f}_p &= \frac{\sqrt{2\gamma_s}}{\zeta}e^{-\gamma(T-t)} + \frac{\gamma_s g}{\zeta^2\sqrt{\gamma}\sqrt{1-e^{-2\gamma T}}}(2-\frac{\gamma_s}{\gamma})e^{-\gamma t}\\
&\quad - \frac{\gamma_s g}{\zeta^2\sqrt{\gamma}\sqrt{1-e^{-2\gamma T}}}e^{-2\gamma T+\gamma t}[2-\frac{\gamma_s}{\gamma}-2\gamma_s(T-t)],
\end{aligned}$$

and the corresponding normalization factors read

$$\bar{N}_{B/A} = \int_0^T dt\,\bar{f}_{N,B/A}(t)^2, \quad \bar{N}_{x/p} = \frac{1}{2}\int_0^T dt\,\bar{f}_{N,x/p}(t)^2,$$

while the coefficients appearing in the equation above are given by

$$\begin{aligned}
\bar{C}_B &= e^{-\gamma T} + \frac{\sqrt{\gamma_s}g}{\zeta\sqrt{2\gamma}}[\sqrt{1-e^{-2\gamma T}}(1-\frac{\gamma_s}{\gamma}) + 2\gamma_s T\frac{e^{-2\gamma T}}{\sqrt{1-e^{-2\gamma T}}}],\\
\bar{C}_A &= \frac{\sqrt{\gamma_s}g}{\zeta\sqrt{2\gamma}}\sqrt{1-e^{-2\gamma T}},\\
\bar{C}_{B/A,N} &= \sqrt{\bar{N}_{B/A}}, \bar{C}_{x/y} = \sqrt{\bar{N}_{x/y}},
\end{aligned}$$

6.3 Experimental realization

6.3.1 Experimental setup

The layout and the time sequence for teleportation and verification are shown in Figure 6.1. A y-polarized, 3ms-long 5.6mW drive light pulse is sent through ensemble B which is blue detuned from the D_2 line $F = 4 \rightarrow F = 5$ transition by $\Delta = 850$MHz. The interaction creates the entanglement between the x-polarized forward scattered mode and the the collective spin B. The quantum light co-propagating with the drive light is then directed through ensemble A where the dispersive interaction leads to partial mapping the spin state of atomic ensemble A onto the light field, and then a measurement of one of the quadrature operators $\sim \hat{S}_y$ in

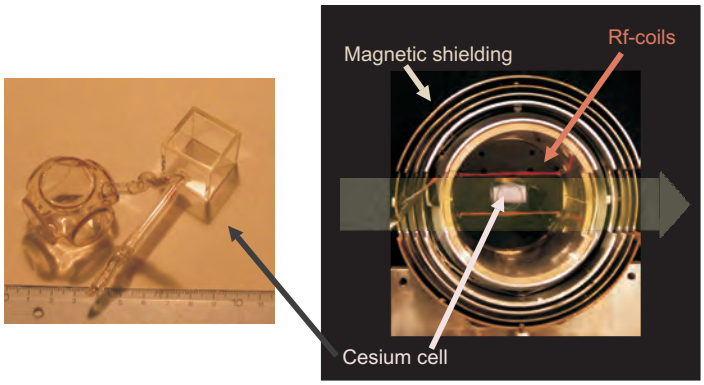

Fig. 6.2 Two glass cells filled with Cesium are shown on the left. The square glass cell consisting $N_A \approx 10^{11} \sim 10^{12}$ atoms is used in this quantum teleportation experiment which is situated in a magnetic shield shown on the right. The bias magnetic field of 0.9G is pointing out of the picture plane here and is created by four coil pairs. The RF coil are oriented such that the RF field lies orthogonal to the bias field and macroscopic spin. Two apertures along the transversal direction allow the light beam to pass the cell. The pump beams are aligned in direction of the main axis and also a small and weak probe light beam to monitor the atomic density by measuring the Faraday angle directly.

the x-polarization mode behind the ensemble constitutes the Bell measurement where as mentioned in the protocol section the driving light acts as the local oscillator to perform the polarization homodyning detection. The photocurrent is analyzed with a lock-in amplifier at Ω and further computer processed to obtain measurements of the temporal modes of interest to compensate the atomic decay where an exponential mode function is applied, and thus the read-out mode is $\hat{x}_{c/s,-} \propto \int_0^T dt\hat{x}(t)e^{-\gamma t}\cos/\sin(\Omega t)$. The teleportation protocol is completed by sending the measurement results $\hat{x}^{out}_{c/s,-}$ through a classical link to the site B with gain $g_x = g_p = g$ where spin rotations in the y-z plane conditioned on these results are performed using phase- and amplitude controlled radiofrequency magnetic field pulses at frequency Ω. The deterministic character of homodyne process ensures success of the teleportation in every attempt. It should be noticed that experimentally for the read-out of each individual ensemble the other ensemble is detuned from the atom-light interaction by briefly detuning the B field in the respective cell.

6.3.2 Experimental results

The reconstruction of the collective spin state as described before relies on the input-output relation of light variables, and for the off-resonant light-atom interaction this linear trans-

formation is given as

$$\hat{x}^{out}_{c/s,-} = \kappa \cdot \hat{p}_A/\hat{x}_A + c_x \cdot \hat{x}^{in}_{c/s,f_x} + c_p \cdot \hat{p}^{in}_{c/s,f_p} + c_N \cdot \hat{F}_{p/x},$$

Here, the first term is a contribution of the atomic spin variable due to Faraday rotation of light polarization, the second term is proportional to the input value of the light quadrature $\hat{x}_L$ of the temporal mode f_x and the third term is the contribution of the other quadrature of input light $\hat{p}_L$ of temporal mode f_p resulting from back action of light on atoms (see Supplementary Information). All input light modes are always in a coherent or vacuum state with $\mathrm{Var}(\hat{x}^{in}_{c/s,f_x}) = \mathrm{Var}(\hat{p}^{in}_{c/s,f_p}) = 1/2$. The last term describes additional noise arising from atomic decoherence with $\mathrm{Var}(\hat{F}_{p/x}) = m/2$ with $m = 1.3$ calculated from the atomic spin relaxation[29]. In our experiment since A y-polarized, 2ms-long 5.6mW light pulse blue detuned from the D_2 line $F = 4 \rightarrow F = 5$ transition by $\Delta = 850$MHz drives the interaction, $\zeta^2 = 1/6.3$ is calculated from Clebsh-Gordon coefficients and experimentally verified while the relaxation rates are measured with the results of $\gamma = 99.3 \pm 0.2 s^{-1}$ and $\gamma_{\mathrm{extra}} = 26.3 \pm 0.2 s^{-1}$. The coupling strength is measured as $\kappa = 0.87$ by using the mean value transfer[35]. According to these measured parameters the coefficients shown in equation above can be found with the values of $c_x = 0.93$, $c_p = 0.50$ and $c_N = 0.17$. Additionally, For the atomic-state reconstruction the detection efficiencies including optical losses $\eta_B = 0.8 \pm 0.03$ and $\eta_A = 0.89 \pm 0.03$ for ensembles B/A are taken into account. Using equation above the mean values of the input states of ensemble A are found from measurements of light variables as $\langle x_A \rangle = \langle x^A_{c,-} \rangle / \kappa$ and $\langle p_A \rangle = \langle x^A_{s,-} \rangle / \kappa$ with the variance of $\mathrm{Var}(x_A) = (\mathrm{Var}(x_{c,-}) - c_x^2/2 - c_p^2/2 - c_N^2 m/2)/\kappa^2$ and $\mathrm{Var}(p_A) = (\mathrm{Var}(x_{s,-}) - c_x^2/2 - c_p^2/2 - c_N^2 m/2)/\kappa^2$. It is found that the initial spin state with the variance of $\mathrm{Var}(x_A) = \mathrm{Var}(p_A) = (1.03 \pm 0.03) \cdot 1/2$ is close to the coherent spin state.

6.3.3 Fidelity

To verify whether or not a successful quantum teleportation event is performed, the fidelity of state transfer is compared to the classical benchmark fidelity which has a rigorous form of $(1+\bar{n})/(1+2\bar{n})$ [84] where $\bar{n} = \langle b^\dagger b \rangle$ is the mean number of spin excitations for the displacement of Gaussian distribution. The performance of the protocol is assessed using the average fidelity with respect to a Gaussian distribution of coherent input states as figure of merit. The fidelity is given by the overlap of the final atomic state in ensemble B $\left|\Psi^{\mathrm{tele}}_B\right\rangle$, which is described by x^{tele}_B and p^{tele}_B and the optimal final state which is defined by the initial state in ensemble A x^{in}_A and p^{in}_A. For a given coherent input state with mean values $\langle x_A \rangle$ and

$\langle p_A \rangle$, the single-shot fidelity is given by

$$F(\langle x_A \rangle, \langle p_A \rangle) = 2\frac{e^{-\frac{-\left|\langle x_A \rangle - \langle x_B^{\text{tele}} \rangle\right|^2}{1+2\text{Var}(x_B^{\text{tele}})} - \frac{\left|\langle p_A \rangle - \langle p_B^{\text{tele}} \rangle\right|^2}{1+2\text{Var}(p_B^{\text{tele}})}}}{\sqrt{(1+2\text{Var}(x_B^{\text{tele}}))(1+2\text{Var}(p_B^{\text{tele}}))}} \tag{6.2}$$

such that the average fidelity $\bar{F}(\bar{n})$ with respect to a Gaussian distribution with width $\bar{n}$

$$\begin{aligned}\bar{F}(\bar{n}) &= \frac{1}{2\pi\bar{n}} \int\int_{-\infty}^{\infty} d\langle x_A \rangle d\langle p_A \rangle F(\langle x_A \rangle, \langle p_A \rangle) e^{-\frac{\langle x_A \rangle^2 + \langle p_A \rangle^2}{2\bar{n}}} \\ &= \sqrt{\frac{2}{1+2\text{Var}(x_B^{\text{tele}}) + 2\bar{n}(1-\left|\frac{\langle x_B \rangle}{\langle x_A \rangle}\right|)^2}} \cdot \sqrt{\frac{2}{1+2\text{Var}(p_B^{\text{tele}}) + 2\bar{n}(1-\left|\frac{\langle p_B \rangle}{\langle p_A \rangle}\right|)^2}}.\end{aligned} \tag{6.3}$$

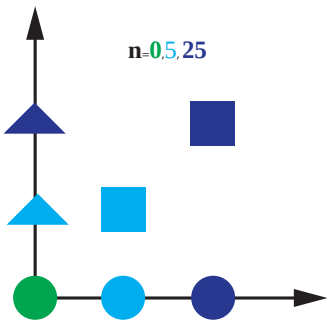

Fig. 6.3 The mean value of different input states.

Experimentally, we perform the teleportation using various sets of CSSs of ensemble A with varying $\langle \hat{J}_{y,z} \rangle$, corresponding to displaced vacuum (coherent states) as input states shown in Figure 6.3 (the vacuum, the CSS with displacements of 5 in vacuum units and phases $0, \pi/4, \pi/2$, and the CSS with displacements of 25 in vacuum units and phases $0, \pi/4, \pi/2$). For every input state, $10,000 \sim 20,000$ teleportations have been performed with one full cycle of the protocol lasting 20ms. Figure 6.4 (a) shows the variance of the teleported states as a function of gain g. The quadratic dependence of the variances on g predicted by the model fits the experimental data very well. For a certain range of g the atomic variances are reduced owing to the entanglement of the transmitted light with ensemble B. Figure 6.4 (b) presents the experimental fidelity, which is above the classical benchmark for $\bar{n} \leqslant 7$. The blue dots represents the scheme that the feedback is done by preforming a displacement with a radio-frequency pulse applied to ensemble B, followed by a reading pulse to verity the atomic states, while the red dots give the results in the scheme that the verification read-out is done firstly, followed by the displacement operation applied to the

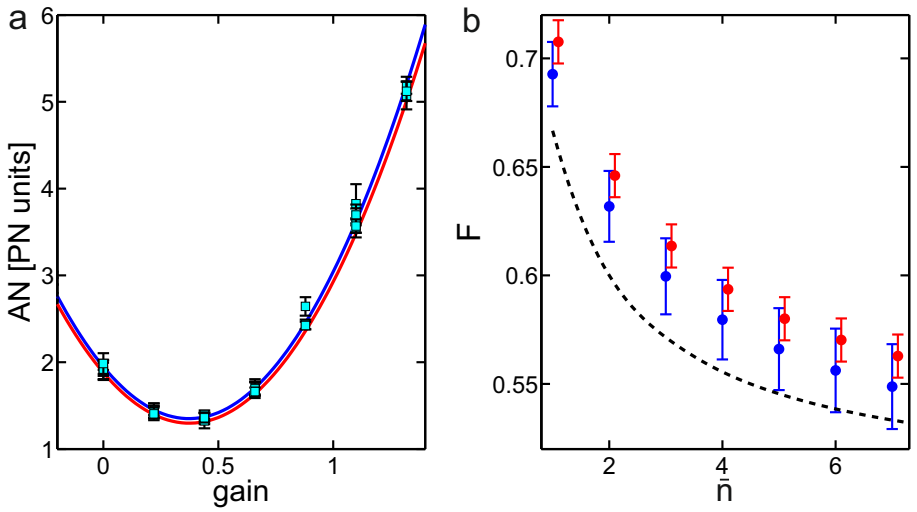

Fig. 6.4 (a) The variances of the teleported state $\mathrm{Var}(x^{\mathrm{tele}}, p^{\mathrm{tele}})$ as a function of gain. (b)Teleportation fidelity as a function of the mean photon number of the set of states. Teleportation with radio-frequency feedback (blue dots), feedforward teleportation (red dots), and classical benchmark (black dashed line). Error bars present one standard deviation.

result of measurement numerically. The worse performance of radio-frequency feedback scheme is due to introducing of additional technical errors.

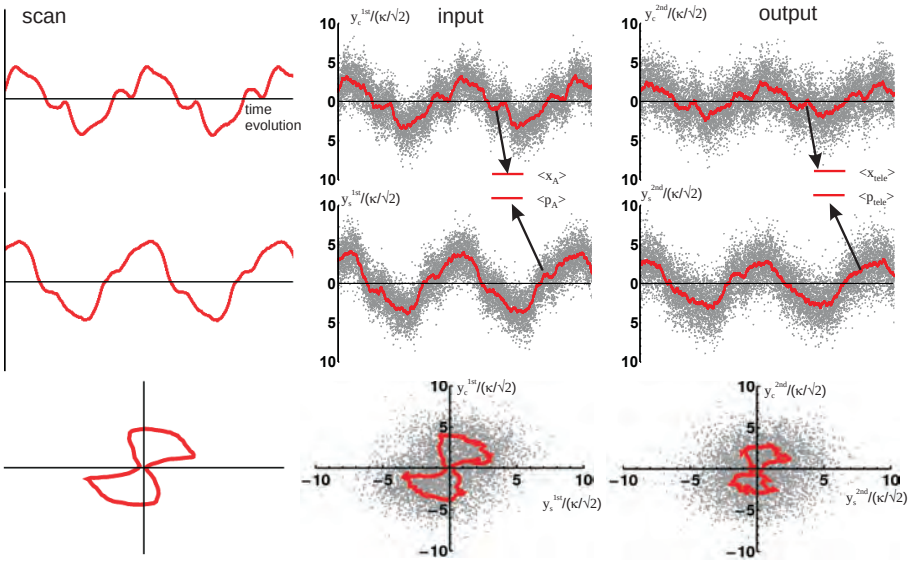

Fig. 6.5 Teleportation with a dynamically varied input state. The input displacements of $x_A \propto B^s_{rf}, p_A \propto B^c_{rf}$ are varied in time as shown in the left column ($B_{rf} \approx 1$pT). The center/right column presents the readout of the input/teleported dynamics of the atomic spin A/B. The upper/center row is the x/p variable and the lower row is a two-dimensional plot x/p. Every gray point is a teleportation run with the points taken at the rate of ~ 50Hz.

Stroboscopic teleportation of a sequence of spin states from A to B is shown in Figure 6.5 where the repeated teleportation cycles are performed while varying the amplitude and phase of the input state. The left column shows the time-varying radiofrequency field in the picoTesla range that is applied to prepare a new spin state A in each individual teleportation run, after initializing both ensembles to vacuum between the runs. The central column shows the read-out of the input-state evolution of ensemble A and the right column shows the read-out of the teleported-state evolution. The points represent results for individual teleportation runs.

6.4 Conclusion and outlook

We demonstrate a missing element of the quantum teleportation landscape, the deterministic continuous variable teleportation between distant material objects - room temperature atomic spin ensembles. Entanglement required for teleportation is distributed by light propagating from one ensemble to the other. Quantum states encoded in the collective spin state of one ensemble are teleported onto another ensemble spin using this entanglement and homodyne measurements on light. By implementing process tomography, we demonstrate that the experimental fidelity of the quantum teleportation is higher than that achievable by any classical process. Furthermore, we demonstrate the benefits of deterministic teleportation by teleporting a dynamically changing sequence of spin states from one distant object onto another.

The fidelity of the teleportation can be further improved by using time varying driving pulses and increasing the optical depth of the atomic ensemble, as shown in[85]. Nonclassical states can be efficiently teleported using continuous variable teleportation[81], and continuous variable teleportation of an atomic qubit encoded in a collective spin by a photon scattering can be performed using the present approach. The stroboscopic teleportation of the spin dynamics can be also extended towards a true continuous in time teleportation paving the way to teleportation of quantum dynamics and simulations of the interaction between two distant objects which do not interact directly. From the quantum sensing perspective teleportation of spin dynamics would allow to perform measurements at the location spatially separated from the environment where the actual dynamics takes place.

Chapter 7

Conclusions and outlook

7.1 Conclusions

The micro-fabricated room temperature Cs vapor cell provides the opportunity to realize the scalable quantum metrology and quantum information devices that can be readily integrated in larger quantum networks. For the cubic vapor cells with the size of 2.2cm since the density of atoms can not be increased much by heating due to the properties of the paraffin coating, and a higher optical power leaves us with technical difficulties in the detection as well as problems with growing classical noise, there are limitations on the experimentally achievable coupling strengths. Also its limited bandwidth, due to the required times for atoms to pass through the laser beam impedes us to run some quantum protocols like generation of single-photon on demand.

By utilizing the microcells coupled into an optical resonator these problems can be overcome. Because of small beam area, the required number of photon is also reduced which means that the weak light beam can satisfy the condition of atom-light interaction. Cavity enhanced optical depth by a factor of $2\mathfrak{F}/\pi$ can compensate the reduction resulted from the decrease of cell size. Additionally, a $300 \times 300\mu\text{m}^2$ cross section of our microcell sets the atomic transit time about $1 \sim 2\mu$sec, which can match the bandwidth of single excitation by using a filter cavity following atom-light interaction system[53]. In this thesis, the atomic ensemble of $10^7 \sim 10^8$ atoms is contained in a glass cell microchannel, $300 \times 300\mu\text{m}^2$ in cross section and 1cm in length. A hole $10 \sim 20\mu$m in diameter is laser-drilled at the top surface of the chip to create an entrance through which the channel is filled with Cs vapor. Windows with anti-reflection coating are attached at both ends of the microchannel to reduce the transmission losses. Currently, the intensity loss per window is about $3 \sim 4\%$, limited by the deterioration of the anti-reflection coating quality in the glass blowing phase. An alkene coating deposited on the inner cell surface can stand more than 10^4 collisions with

the Cs atoms before decoherence occurs, resulting in longitudinal spin lifetime $T_1 = 17$ms and transverse spin lifetime $T_2 = 10$ms in the absence of light fields.

The microcell is placed inside a standing wave optical cavity consisting of a high-reflection input coupler and the output coupler with transmission of 80%. 6.5% single-pass loss in the cell windows partially results in a finesse $\mathfrak{F} \approx 17$. As discussed in Chapter 4 the optimal squeezing can be achieved with an impedance matched cavity where the output coupler transmission $T_2 \approx l_{cav}$, where l_{cav} is the round-trip intensity loss. Thus, our experimental setting is close to this condition.

Based on this system we have experimentally developed the quantum backaction evading measurement of one quadrature of collective spin components by stroboscopically modulating the intensity of probe beam at twice Larmor frequency. Furthermore, a spin-squeezed state conditioned on the light-polarization measurement with 2.2 ± 0.3dB noise reduction below the spin projection noise limit for the measured quadrature has been demonstrated which is be useful for quantum metrology and sensing, as well as for generation of entanglement between disparate oscillators.

As an application of stroboscopic back-action-evading measurement, we demonstrated a quantum noise limited optical magnetometer at room temperature with an rf magnetic-field sensitivity of $158 \pm 1\text{fT}/\sqrt{\text{Hz}}$ and 2D spatial resolution of 300μm. Furthermore, by sandwiching the rf pulse between two backaction evading measurements, an magnetometer with 13% spin-squeezing below the projection noise limit was realized, where conditional spin squeezed state generated by the first optical pulse, and then the second optical pulse measures the displacement of the SSS caused by magnetic field.

Deterministic quantum teleportation of the collective spin state from one atomic ensemble to another was reported in Chapter 6 where the cubic vapor cells with the size of 2.2cm were employed. Then the stroboscopic teleportation of spin dynamics was demonstrated with the fidelity higher than the classical benchmark. This can be extended to teleportation of quantum dynamics and simulations of the interaction between two distant objects that have never interacted directly.

7.2 Outlook

High quality Microcells

As described in this thesis, atomic density, spin life time and intensity transmission are three key parameters of the room-temperature vapor cell. We have achieved the reasonable values at the present stage. However, if for microcells inside optical resonators we really

need to improve the fabrication to increase the intensity transmission and thus reduce the information loss of the system. In Chapter 5, the effect of optical cavity has been discussed where we derive the optimal variance spin squeezing as $\mathrm{Var}(X_A) \propto \frac{1}{\sqrt{\mathfrak{F}}}$ with the condition of $T_2^{opt} = l_{cav}$ and the round trip intra-cavity loss l_{cav} is mainly determined by the optical loss propagating trough the microcell. Additionally, for atoms inside an optical cavity, both the resonant single pass optical depth of the atomic ensemble d and the light-atoms coherent coupling strength κ are enhanced by a factor of $2\mathfrak{F}/\pi$. Although the good anti-reflection coated windows are employed, the current single-pass intensity loss of the microcell is about 6.5% coming from the deterioration of the anti-reflection coating quality in the glass blowing phase, therefore, we are employing the CO_2 laser bonding procedure to attach windows at the edges of the cell, and attach a round tube to the cell's top surface where the micro-hole is drilled.

Quantum sensor in the biological application

Our compact and simple optical magnetometer with high spatial resolution and sensitivity is a candidate to be used as a non-invasive biomagnetic sensor because it is room temperature where life lives. At present we are in the early stages of a collaboration with the biology group and Membrane Biophysics group in the University of Copenhagen to study the nerve signals from frogs and lobsters. In Figure 7.1 we show an simulation experiment that simulates a neuron pulse by sending a RF-pulse into the RF coil of one sinusoidal cycle with period of 0.3ms as shown on the right of top into the RF coil.The left top of Figure 7.1 shows the spin response signal.

High efficiency single photon generator for DLCZ protocol

To achieve long-distance, high-fidelity, qubit teleportation, an architectures using neutral atoms was proposed by Duan, Lukin, Cirac and Zoller (termed DLCZ hereafter)[5]. In DLCZ scheme, entanglement distribution is accomplished by weak coherent driving of a Raman transition in an atomic ensemble followed by path-erasing photodetection. Although the motion of the atoms destroys atomic superposition states in the thermal vapor cell, motional averaging discussed in Chapter 2 can be used to realize room temperature quantum memories and coherent single photon sources where atoms move in and out of the beam several times during the interaction while maintaining the spin coherence for much longer times. In [53], it is shown how both read and write efficiencies above 90% can be achieved for a real experimental system based on Cs-atoms inside a microcell similar to the one described in this thesis. Since the microcells have the potential to be integrated in semicon-

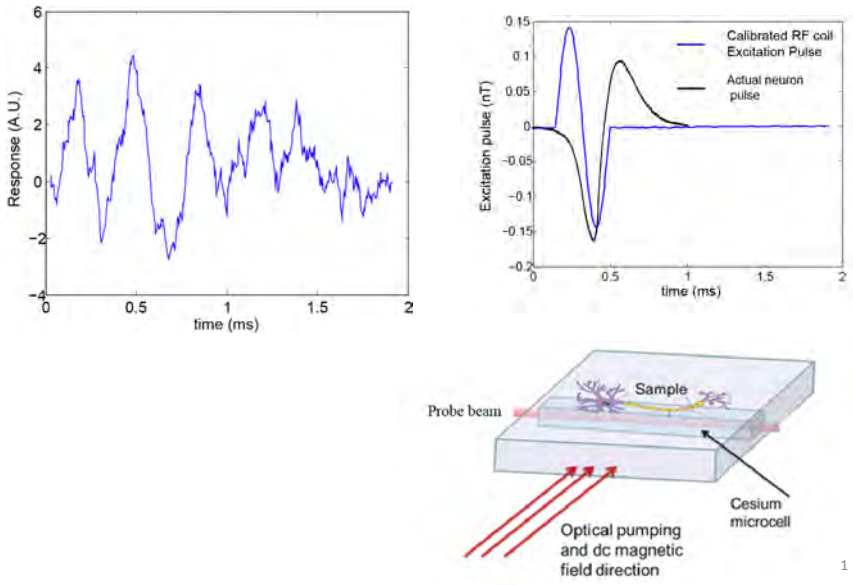

Fig. 7.1 Simulated biomagnetic experiment.

ductor chips, the fiber-coupled, integrated quantum repeater could be demonstrated in the future.

Nano-mechanical membrane-atomic ensemble interface

Since the existence of challenges for the optomechanical system to prepare, manipulate and measure quantum states with high precision, a quantum interface between atomic ensembles and optomechanical systems has been proposed in [86], where light plays the role of a quantum bus. Furthermore, the establishment of quantum entanglement between an atomic spin oscillator with a negative mass and a mechanical oscillator coupled to light via radiation pressure can enable the trajectory of the mechanical oscillator to be measured with the precision beyond the standard quantum limit. Soon, we will perform the first efforts to couple the atomic ensemble in the microcell to a optomechanical system (membrane-in-middle type) which is sitting in the separate room at QUANTOP, and hope to see EPR entanglement between the atoms and the mechanical oscillator as the next step.

Multipartite entangled states

Multipartite entangled states play a crucial role in quantum information processing. Recently, one special type of multipartite entangled states called graph state, has been proposed[87, 88] and gradually became a key component of quantum information systems because it allows large scale quantum information tasks to be implemented orderly according to the specific program. Cluster states as a well-known member of this family provide the universal source for one-way quantum computation model where the system is firstly initialized in a cluster state, independently of the quantum algorithm which is to be implemented and determined by different temporal and spatial sequences of series of the projective measurements[89]. Correspondingly, one-way quantum computation based on cluster states have been demonstrated experimentally both in DV[8] CV regime[7]. Additionally, graph states of optical field have been theoretically described in general[87, 88, 90], and generated in different structures experimentally[91, 92]. Since entanglement-assisted networks communication with higher channel capacity than classical limit can be realized by applying multipartite entangled states, graph states can also be used to set controlled quantum communication networks[93]. Due to specific quantum correlation of graph states, the channel capacities between two users can be controlled and the signal-to-noise ratios can surpass the shot noise limit of the classical optical communication. We can generate this kind of hybrid multipartite graph state based on off-resonant Faraday interaction between light and atoms[11, 94].

Appendix A

Details of the magnetic coil system

DC magnetic field

DC bias coil

The wire-coil system which creates the static field sits on an aluminum cylinder, which is located insider 3-layers of μ-metal magnetic shields, thus providing an environment isolated from external stray magnetic fields. The static bias magnetic field in the x-direction(quantization direction) is generated by sending a current through eight equally spaced coils with different numbers of windings similar to a solenoid. Although there exists the inhomogeneity in x-direction, due to 300μm dimension of the vapor cells this inhomogeneity has an insignificant effect on the measurements. However, the inhomogeneity in the propagation direction (z-direction) is important for the measurements. For large applied magnetic fields, this inhomogeneity, the coherence of spins leading to shorter spin life time. The B_x magnetic field distribution along z-direction is plotted in Figure A.1.

DC compensation coil in the probe propagation direction

The quadratic correction in the z-direction is accomplished via a double-saddle coil arrangement consisting of eight circular arcs[95], wound on the cylinder beneath the plastic rings. This geometry was initially designed to be used as a linear gradient coil with the current direction shown in the pink arrows; however, if changing the current direction as shown in the black arrows, this double-saddle structure can be used as a quadratic coil. In Figure A.3, the magnetic field distribution along z-direction is plotted. Currently, both 5-turn linear gradient and quadratic coils are located on the aluminum cylinder.

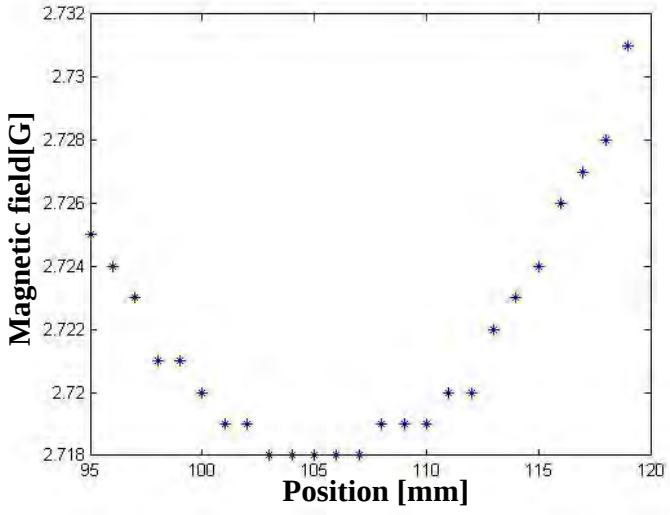

Fig. A.1 DC magnetic field distribution along z-direction with current $I = 200$mA and $R = 22.35$Ohm.

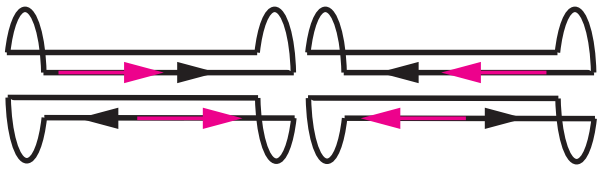

Fig. A.2 Double-saddle compensation coil schematic drawing. The pink arrows show the current direction for the linear gradient coil, and the black arrows show the current direction for the quadratic coil.

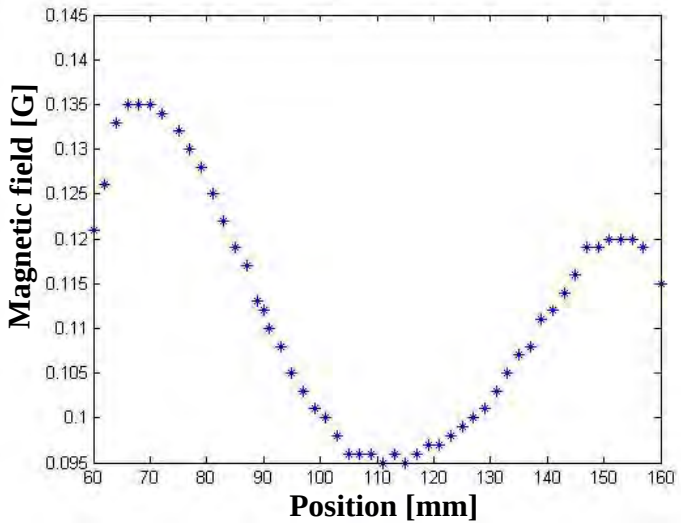

Fig. A.3 Magnetic field distribution of the B_x component in z-direction generated by double-saddle compensation coil with current $I = 200$mA.

Weak bias magnetic field in the transverse directions

As discussed in the main text, the propagation direction of the probe beam should be perpendicular to the direction of the DC bias magnetic field, which is parallel to the optical pumping direction. Since the probe light is circulating in an optical cavity, it is difficult to satisfy this geometry by aligning the cavity field, and aligning the magnetic field inside the shield by hand is not precisely. Therefore,of the Bx component in the y and z-direction are utilized as shown in Figure A.4 to create the homogeneous magnetic field in y and z-direction. In Figure A.4 the black and red symbols represent the current direction in the copper wires for B_y and B_z magnetic field creation respectively. The θ angle of the cosine windings can be calculated according to[96], and here we use 10.6°, 30° and 56.5° to generated the homogeneous weak bias magnetic field in a range larger than 2cm.

Calibration of the RF coil

In order to calibrated the RF coil, a pick-up coil with 30 turns copper wire is employed as shown in FigureA.5. The oscillating magnetic field creates a flux through the pick-up coil which generates an electromotive force When applying a sinusoidal magnetic field of frequency omega and amplitute B_{rf}. The current through the pick-up coil can be found from measuring the voltage amplitude U_ω across the measurement resistor R_m [34].

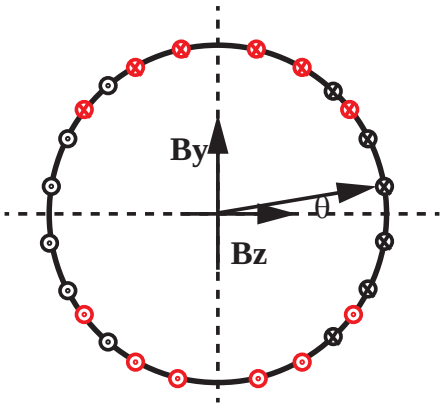

Fig. A.4 Cosineθ coil in y(red symbols) and z(black symbols)-direction schematic drawing. The black and red symbols represent the current direction in the copper wires for B_y and B_z magnetic field creation.

Fig. A.5 Photo of pick-up coil.

$$\left|B_{rf}\right| = \frac{\left|1 + Z_{coil}/R_m\right| \left|U_\omega\right|}{N_\omega A_{coil} \omega}, \tag{A.1}$$

The pick-up coil has the following parameters: number of windings $N_\omega = 30$, area of the coil $A_{coil} = \pi r^2 = \pi(3.75\text{mm})^2$, and the impedance $Z_{coil} \approx i\omega \cdot L$ at frequency ω with the inductance of $L = 55\mu\text{H}$, since the resistance of the coil $R = 3\Omega$ is much smaller than $\omega \cdot L$ at the frequency we usually operate (380kHz). We use lock-in amplifier to read of the response generated in the pick-up coil. Since the voltage is read out over the resistance $R_m = 50\Omega$. The measured amplitude of the voltage is $U_\omega = \sqrt{2}U_{rms}$ where U_{rms} is the rms voltage.

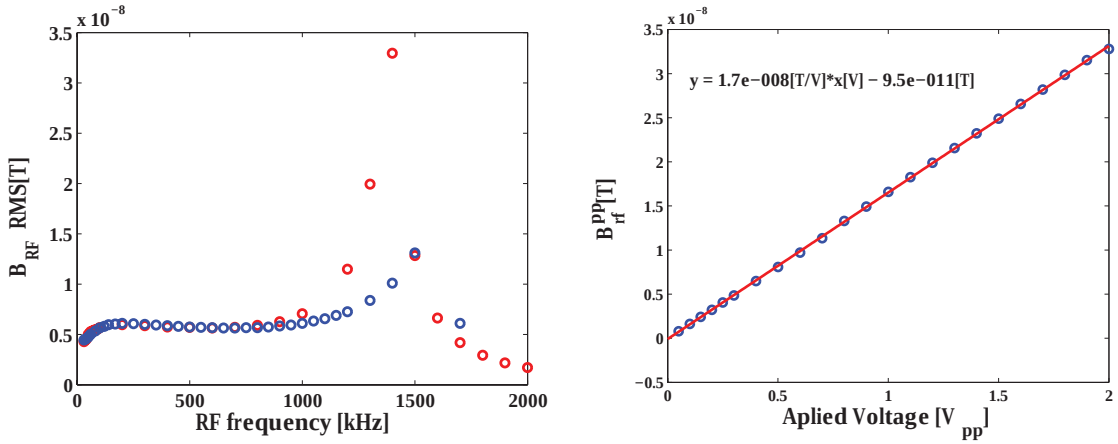

(a) (b)

Fig. A.6 (a)The generated magnetic field B_{rf}^{rms} for different frequencies. For all the frequency range the same voltage was applied in the RF coil. Two different colors represent the calibration from Bing and Giorgos,respectively. (b) The measured B_{rf}^{pp} for different applied voltage at 322kHz with external resistor $R = 20\Omega$. "pp" means peak-to-peak value.

Appendix B

Details of the microcell fabrication

1st-generation chip fabrication

These cell-chips with dimensions in the micrometer range were designed and fabricated by both QUANTOP at Niels Bohr Institute and Danchip at DTU. As is shown in Figure 3.5, the finished chip consists of 4 layers (for 5 layer-samples there is an additional glass layer on the top of the whole structure). The cell is the narrow channel ($200\mu m \times 200\mu m \times 10mm$) in the middle glass and suitable holes in the middle silicon and bottom glass for Cs access were created.. There is no special process for the top silicon layer.

In the middle glass layer, a groove with a $200\mu m \times 200\mu m$ cross section was developed by Micro saw. Before the final decision of the cutting method, we have compared the performance of Micro saw cutting followed by Chemical roughness reduction (treatment with HF:HCl mixture) with Micro saw cutting only. It was found that employing only the Micro saw cutting we can get the walls with roughness of 40nm as characterized by an optical profiler. In order to etch a small funnel on the second silicon layer, Photo-lithography and Etching were utilized successively to transfer the structures from mask to silicon wafer. Firstly, Nitride was deposited by low pressure chemical deposition (LPCVD) on the silicon wafer to develop a thin Nitride membrane that protects other part of the wafer to be etched in the KOH etching. And then, we did the wafer exposure under 7W of ultraviolet laser light for 5.6s which is followed by 60-second of development. We then make sure that there is no resist visible by inspecting with optical microscope; otherwise Plasma Asher should be used to clean it. Following exposure, the Nitride membrane covering the hole should be removed to make sure the etching on the silicon can be conducted successfully which can be done by using Reactive-ion etching (RIE) equipment. In addition the residual resist material should be striped by immersing the wafer into Acetone solution for several minutes. After this preparation work, we can do the real silicon etching by utilizing KOH etching which

belongs to the family of anisotropic Si-etchants based on aqueous alkaline solutions. During the etching process, we should check if the etch rate is appropriate. As mentioned above, the Nitride membrane can protect other part of the wafer from etching in the KOH solution, so this membrane covers the whole wafer except for the hole-structure and should be striped by RIE. Until now, the funnel is produced on the silicon wafer and three different hole sizes are obtained (19μm, 29μm, and 54μm).

A large hole is required on the bottom layer glass which is the entrance for the evacuating, coating, and filling of the cell. To avoid the damage on the glass wafer, the whole production of the large hole consists of two steps: laser marking and sand blowing. At the first stage, the laser burns the blue tape which sticks onto the wafer to protect it, and a little bit of the glass surface. Then, the Aluminum Oxide 110μm in diameter spheres at high pressure are used to do the abrasive action. Finally, we obtain the 3mm hole on this glass wafer.

With those separated wafers as the components of final chip, we can combine them together by implementing the bonding process with the equipment of EVG Nanoimprint Lithography (NIL). The first bonding is to combine the glass grove wafer with the silicon funnel wafer where a precise alignment is required. Here, anodic bonding is utilized, which means we should place the Si wafer closest to the chuck and the Pyrex wafer closest to the electrode. Secondly, we bond the two other wafers, that is the hole wafer and the untouched silicon wafer, resulting in a two-layer wafer. We complete a the chip production with cutting into small pieces of chips and polishing these chips.

Current generation chip fabrication

The bare chips with the channel are ordered from VitroCom and the bare windows are coated with anti-reflection coating in Denmark. The microholes were drilled by using a 50W, 1064nm picosecond-pulsed Nd:YAG laser (neodymium-doped yttrium aluminium garnet) at the Danchip facility.In order to encapsulate the microcell, anti-reflection coated windows are fused to the glass cylinder with the chip inside (with glass spacers placed around the chip) and also a glass stem with an opening is fused to the cylinder. The whole glass structure is annealed at above 550° to remove stresses that could lead to the optical birefringence as discussed before. Vacuum-tight test should then be done on the whole glass structure. We are running the laser bonding procedure with CO_2 laser now to replace the glass blowing and fusion phase.

The anti-relaxation coating procedure begins with the cleaning of micro-channel with a solution of hydrochloric acid, then rinsing with distilled water followed by the vacuum-

pumping. Heated coating material and Cesium are injected into the channel through the micro-hole, subsequently. To increase the atomic density and redistribute the coating material evenly, the microcell is cured for 3-4 hours at $60^{\circ}C$ and allowed to cool down slowly before being removed from the oven. At this time, the microcell fabrication is finally finished. The glass blowing and coating procedures are operated by Mikhail Balabas (of the S. I. Vavilov State Optical Institute, St. Petersburg, Russia).

Appendix C

Phase-Locking and Frequency-Locking system

PDH frequency stabilization

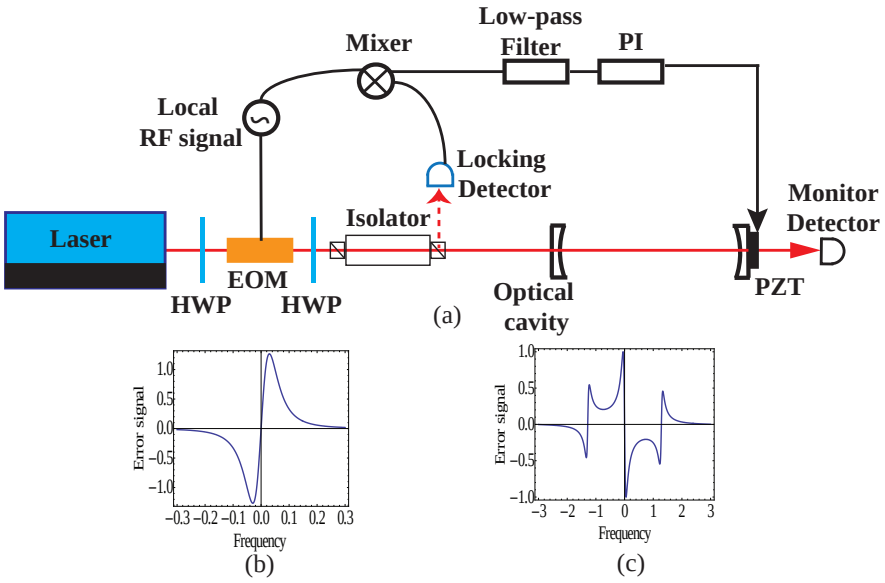

Fig. C.1 (a)The basic layout for locking a cavity to a laser. (b)The PDH error signal, $\varepsilon/2\sqrt{P_s P_c}$ vs ν/ν_{free} , when the modulation frequency is low. (c) The PDH error signal, $\varepsilon/2\sqrt{P_s P_c}$ vs ν/ν_{free} , when the modulation frequency is high.

The original scheme of PDH locking system is shown in Figure C.1. The Laser beam is frequency modulated by a Electro-optic modulator (EOM), driven by a local oscillator at frequency Ω_m and then injected in the optical cavity. The reflected beam from an optical

isolator is sent into a broadband photodetector. The output electronic signal is mixed with the local oscillator's signal via a mixer where the phase of this local oscillator can be tuned by internal or external delay line. Since the mixer is a device whose output is the product of its inputs, this output will contain signals at both dc (or very low frequency) and twice the modulation frequency. The low frequency signal carrying the information of the derivative of the reflected intensity can be picked up by a low-pass filter, and then goes through a proportional-integral controller (PI) and into the piezoelectric transducer (PZT), locking the cavity to the laser. Using the knowledge in Chapter 3, we can derive the reflection coefficient $F(\nu)$ as

$$\begin{aligned} F(\nu) &= E_{ref}/E_{in} = \frac{T_1\sqrt{R_1} - \sqrt{R_1}(1-g(\nu))}{1-g(\nu)}, \\ g(\nu) &= g_m e^{-i\delta\phi} = \sqrt{R_1 \cdot R_2(1-l_{cav})}Exp[-i2\pi(\nu_L - \nu_{cav})] \end{aligned} \tag{C.1}$$

As given in[65], if the modulation frequency is very low with respect to the bandwidth of cavity, the error signal after the low-pass filter can be written as

$$\varepsilon \approx 2\sqrt{P_s P_c}\frac{d\,|F(\nu)|^2}{d\nu}\Omega_m, \tag{C.2}$$

where $P_c = J_0^2(\beta)P_0$ and $P_s = J_1^2(\beta)P_0$ are the power in the carrier and in the first sideband respectively expressed in terms of the Bessel functions with modulation depth β and input power P_0. Otherwise, if modulation frequency is high with respect to the bandwidth of cavity, the error signal after the low-pass filter can be written as

$$\varepsilon \approx -2\sqrt{P_s P_c}Im[F(\nu)F^*(\nu+\Omega_m) - F^*(\nu)F(\nu-\Omega_m)] \tag{C.3}$$

The profiles of both case of high and low modulation frequency are plotted in Figure C.1 (b) and (c), respectively.

Cavity phase locking by PDH-like locking

Since in our experimental, the cavity bandwidth is about 40MHz, and typically if one wants to use the frequency modulation scheme the modulation frequency is several times the cavity bandwidth. It is hard to give such a high modulation frequency. Therefore, instead of frequency modulation on the light beam we send a 10kHz modulated voltage on the PZT attaching to the output mirror. And also we use a lock-in amplifier to replace the separated electronic components including local oscillator generator, mixer, low-pass filter and delay line. The observed error signal is similar to Figure C.1 (b). Additionally, PI controller based

on the Labview program is utilized to lock the cavity on resonance in the pulse scheme where the locking point is in the memory.

Bibliography

[1] C. H. Bennett,G. Brassard,C. Crépeau, R. Jozsa, A. Peres, and W. K. Wootters, Teleporting an unknown quantum state via dual classical and Einstein-Podolsky-Rosen channels,Phys. Rev. Lett. 70, 1895 (1993).

[2] Charles H. Bennett and Stephen J. Wiesner, Communication via one- and two-particle operators on Einstein-Podolsky-Rosen states,Phys. Rev. Lett. 69, 2881 (1992).

[3] Klaus Mattle, Harald Weinfurter, Paul G. Kwiat, and Anton Zeilinger, Dense Coding in Experimental Quantum Communication, Phys. Rev. Lett. 76, 4656 (1996).

[4] Xiaoying Li, Qing Pan, Jietai Jing, Jing Zhang, Changde Xie, and Kunchi Peng, Quantum Dense Coding Exploiting a Bright Einstein-Podolsky-Rosen Beam, Phys. Rev. Lett. 88, 047904 (2002).

[5] L.-M. Duan, M. D. Lukin, J. I. Cirac, and P. Zoller, Long-distance quantum communication with atomic ensembles and linear optics, Nature 414, 413 (2001).

[6] C. Monroe, D. M. Meekhof, B. E. King, W. M. Itano, and D. J. Wineland, Demonstration of a Fundamental Quantum Logic Gate, Phys. Rev. Lett. 75, 4714 (1995).

[7] Ryuji Ukai, Shota Yokoyama, Jun-ichi Yoshikawa, Peter van Loock, and Akira Furusawa, Demonstration of a Controlled-Phase Gate for Continuous-Variable One-Way Quantum Computation, Phys. Rev. Lett. 107, 250501 (2011).

[8] P. Walther, K. J. Resch, T. Rudolph, E. Schenck, H. Weinfurter, V. Vedral, M. Aspelmeyer, and A. Zeilinger, Experimental one-way quantum computing, Nature 434, 169 (2005).

[9] P. W. Shor, Algorithms for quantum computation: Discrete logarithms and factoring, Proc. 35nd Annual Symposium on Foundations of Computer Science (Shafi Goldwasser, ed.), IEEE Computer Society Press, 124 (1994).

[10] Kazuhito Honda, Daisuke Akamatsu, Manabu Arikawa, Yoshihiko Yokoi, Keiichirou Akiba, Satoshi Nagatsuka, Takahito Tanimura, Akira Furusawa, and Mikio Kozuma, Storage and Retrieval of a Squeezed Vacuum, Phys. Rev. Lett. 100, 093601 (2008).

[11] K. Jensen, W. Wasilewski, H. Krauter, T. Fernholz, B. M. Nielsen, M. Owari, M. B. Plenio, A. Serafini, M. M. Wolf and E. S. Polzik, Nat. Phys. 7, 13 (2011).

[12] H. Grote, K. Danzmann, K. L. Dooley, R. Schnabel, J. Slutsky, H. Vahlbruch, First Long-Term Application of Squeezed States of Light in a Gravitational-Wave Observatory, Phys. Rev. Lett. 110, 181101 (2013).

[13] Klemens Hammerer, Anders S. Sorensen, and Eugene S. Polzik, Quantum interface between light and atomic ensembles, Rev. Mod. Phys. 82, 1041 (2010).

[14] Masahiro Kitagawa and Masahito Ueda, Squeezed spin states, Phys. Rev. A 47, 5138 (1993).

[15] D. J. Wineland, J. J. Bollinger, W. M. Itano, and D. J. Heinzen, Squeezed atomic states and projection noise in spectroscopy, Phys. Rev. A 50, 67 (1994).

[16] D. J. Wineland, J. J. Bollinger, W. M. Itano, F. L. Moore, and D. J. Heinzen, Spin squeezing and reduced quantum noise in spectroscopy, Phys. Rev. A 46, R6797 (1992).

[17] Anders Sørensen and Klaus Mülmer, Spin-Spin Interaction and Spin Squeezing in an Optical Lattice, Phys. Rev. Lett. 83, 2274 (1999).

[18] T. Fernholz, H. Krauter, K. Jensen, J. F. Sherson, A. S. Sorensen, and E. S. Polzik, Spin Squeezing of Atomic Ensembles via Nuclear-Electronic Spin Entanglement, Phys. Rev. Lett. 101, 073601 (2008).

[19] Jürgen Appel, Eden Figueroa, Dmitry Korystov, M. Lobino, and A. I. Lvovsky, Quantum Memory for Squeezed Light, Phys. Rev. Lett. 100, 093602 (2008).

[20] M. Takeuchi, S. Ichihara, T. Takano, M. Kumakura, T. Yabuzaki, and Y. Takahashi, Spin Squeezing via One-Axis Twisting with Coherent Light, Phys. Rev. Lett. 94, 023003 (2005).

[21] A. Kuzmich, L. Mandel, and N. P. Bigelow, Generation of Spin Squeezing via Continuous Quantum Nondemolition Measurement, Phys. Rev. A 85, 1594 (2000).

[22] J. Appel, P. J. Windpassinger, D. Oblak, U. B. Hoff, N. Kjargaard and E. S. Polzik, Mesoscopic atomic entanglement for precision measurements beyond the standard quantum limit, Proc. Natl. Acad. Sci. USA. 106, 10960 (2009).

[23] Alberto Politi, Jonathan C. F. Matthews, Jeremy L. O'Brien, Shor's Quantum Factoring Algorithm on a Photonic Chip, Science 325, 1221 (1998).

[24] Peter Lodahl, Sahand Mahmoodian, and Soren Stobbe, Interfacing single photons and single quantum dots with photonic nanostructures, Accepted by Rev. Mod. Phys, arXiv:1312.1079 (2013).

[25] W. H. P. Pernice, C. Schuck, O. Minaeva, M. Li, G. N. Goltsman, A. V. Sergienko, and H. X. Tang, High-speed and high-efficiency travelling wave single-photon detectors embedded in nanophotonic circuits, Nat. Comm. 3, 1325 (2012)

[26] J. Kitching, S. Knappe, and L. Hollberg, Miniature vapor-cell atomic-frequency references, Appl. Phys. Lett. 81, 553 (2002).

[27] W. Hänsel, P. Hommelhoff, T. W. Hänsch, and J. Reichel, Bose-Einstein condensation on a microelectronic chip, Nature 413, 498 (2001)

[28] T. Holstein and H. Primakoff, Field Dependence of the Intrinsic Domain Magnetization of a Ferromagnet, Phys. Rev. 58, 1098 (1940).

[29] D. V. Vasilyev, K. Hammerer, N. Korolev and A. S. Sørensen, Quantum noise for Faraday light-matter interface, Journal of Physics: Atomic, Molecular and Optical Physics, 45, 124007 (2012).

[30] D. V. Kurpriyanow, O. S. Mishina, I. M. Skolov, B. Julsgaard and E. S. Polzik, Multimode entanglement of light and atomic ensembles via off-resonant coherent forward scattering, Phys. Rev. A 71, 032348 (2005).

[31] B. Julsgaard, Entanglement and Quantum Interaction with Macrosopic Gas Samples, PhD thesis, University of Arhus 2003.

[32] H. Krauter, D. Salart, C. A. Muschik, J. M. Petersen, Heng Shen, T. Fernholz and E. S. Polzik, Deterministic quantum teleportation between distant atomic objects, Nat. Phys. 9, 400 (2013).

[33] Jacob F. Sherson, Hanna Krauter, Rasmus K. Olsson, Brian Julsgaard, Klemens Hammerer, Ignacio Cirac and Eugene S. Polzik, Quantum teleportation between light and matter, Nature 443, 557 (2006).

[34] Kasper Jensen, Quantum Information Entanglement and Magnetometry with Macroscopic Gas Samples and Non-Classical Light, PhD thesis, University of Copenhagen 2011.

[35] H. Krauter, Generation and application of entanglement of room temperature ensembles of atoms, PhD thesis, University of Copenhagen 2011.

[36] A. Einstein, B. Podolsky, and N. Rosen, Can Quantum-Mechanical Description of Physical Reality Be Considered Complete? Phys. Rev. 47, 777 (1935)

[37] J. von Neumann, SMathematische Grundlagen der Quantenmechanik, Springer, Berlin 1932.

[38] N. Bohr, Quantum-Mechanical Description of Physical Reality be Considered Complete? Phys. Rev. 48, 696 (1935).

[39] E. Schrödinger, Die gegenwärtige situation der Quantenmechanik, Naturwissenschaften 23, 807 (1935).

[40] M. D. Barrett, J. Chiaverini, T. Schaetz, J. Britton, W. M. Itano, J. D. Jost, E. Knill, C. Langer, D. Leibfried, R. Ozeri, and D. J. Wineland, Deterministic quantum teleportation of atomic qubits, Nature 429, 737 (2004).

[41] W. Tittel, J. Brendel, H. Zbinden, and N. Gisin, Violation of Bell Inequalitities by Photons More Than 10 km Apart, Phys. Rev. Lett. 81, 3563 (1998).

[42] Lu-Ming Duan, G. Giedke, J. I. Cirac, and P. Zoller, Inseparability Criterion for Continuous Variable Systems, Phys. Rev. Lett. 84, 2722 (2000).

[43] R. Simon, Peres-Horodecki Separability Criterion for Continuous Variable Systems, Phys. Rev. Lett. 84, 2726 (2000).

[44] S. M. Tan, Confirming entanglement in continuous variable quantum teleportation, Phys. Rev. A 60, 2752 (1999).

[45] ed. D. Budker, D. F. Jackson Kimball, Optical Magenetometry, Cambridge University Press 2013.

[46] H. G. Robinson, E. S. Ensberg, and H. G. Dehmelt, Preservation of Spin State in Free Atom-Inert Surface Collisions, Bulletin of the American Physical Society 3, 9 (1958).

[47] M. T. Graf, D. F. Kimball, S. M. Rochester, K. Kerner, C. Wong, D. Budker, E. B. Alexandrov, M. V. Balabas, and V. V. Yashchuk, Relaxation of atomic polarization in paraffin-coated cesium vapor cells, Phys. Rev. A 72, 023401 (2005).

[48] M. V. Balabas, T. Karaulanov, M. P. Ledbetter, and D. Budker, Polarized Alkali-Metal Vapor with Minute-Long Transverse Spin-Relaxation Time, Phys. Rev. Lett. 105, 070801 (2010).

[49] S. J. Seltzera and M. V. Romalis, High-temperature alkali vapor cells with antirelaxation surface coatings, J. Appl. Phys. 106, 114905 (2009)

[50] J. C. Allred, R. N. Lyman, T. W. Kornack, and M. V. Romalis, High-Sensitivity Atomic Magnetometer Unaffected by Spin-Exchange Relaxation, Phys. Rev. Lett. 89, 130801 (2002).

[51] M. A. Bouchiat and J. Brossel, Relaxation of Optically Pumped Rb Atoms on Paraffin-Coated Walls, Phys Rev. 147, 41 (1966).

[52] D. A. Steck, Cesium D line data 2003.

[53] J. Borregarrd,et.al., Room temperature quantuam memory and scalable single photon sourece based on motional averaging, Unpublished.

[54] W. Happer, Optical pumping, Rev. Mod. Phys. 44, 169 (1972).

[55] W. Wasilewski, K. Jensen, H. Krauter, J. J. Renema, M. V. Balabas, and E. S. Polzik, Quantum Noise Limited and Entanglement-Assisted Magnetometry, Phys. Rev. Lett. 104, 133601 (2010).

[56] Jacob F. Sherson, Quantum Memory and Teleportation Using Macroscopic Gas Samples, PhD thesis, University of Arhus 2006.

[57] Walter Koechner, Solid-State laser Engineering, 3rd ed. Springer-Verlag 1992.

[58] Serge Haroche, Nobel Lecture: Controlling photons in a box and exploring the quantum to classical boundary, Rev. Mod. Phys. 85, 1083 (2013).

[59] Ling-An Wu, H. J. Kimble, J. L. Hall, and Huifa Wu, Generation of squeezed states by parametric down conversion, Phys. Rev. Lett. 75, 2520 (1986).

[60] Yu Wang, Heng Shen, Xiaoli Jin, Xiaolong Su, Changde Xie, and Kunchi Peng, Experimental generation of 6 dB continuous variable entanglement from a nondegenerate optical parametric amplifier, Optical Express 18, 6149 (2010).

[61] Ian D. Leroux, Monika H. Schleier-Smith, and Vladan Vuletić, Implementation of Cavity Squeezing of a Collective Atomic Spin, Phys. Rev. Lett. 104, 073602 (2010).

[62] Jing Zhang, Kunchi Peng, and Samuel L. Braunstein, Backaction-induced spin-squeezed states in a detuned quantum-nondemolition measurement, Phys. Rev. A 68, 035802 (2003).

[63] Bingkun Zhou.et.al., Princple of Laser, 4th ed. in Chinese, National defense industry press, Beijing, China 2000.

[64] Hans-A. Bachor, Timothy C. Ralph, A guide to experiments in quantum optics, 2nd, Revised and Enlarged Edition edition, Wiley-VCH 2004.

[65] Eric D. Black, An introduction to Pound-Drever-Hall laser frequency stabilization, Am. J. Phys. 69, 79 (2001).

[66] P. J. Windpassinger, M. Kubasik, M. Koschorreck, A. Boisen, N. Kjaergaard, E. S. Polzik, J. H. Mueller, CUltra low-noise differential ac-coupled photodetector for sensitive pulse detection applications, Measurement Science and Technology 20, 055301 (2009).

[67] A. A. Clerk, M. H. Devoret, S. M. Girvin, Florian Marquardt, and R. J. Schoelkopf, Introduction to quantum noise, measurement, and amplification, Rev. Mod. Phys. 82, 1155 (2010).

[68] V. B. Braginsky, Yu. I. Vorontsov, F. Ya. Khalili, Optimal quantum measurements in gravitational-wave detectors, JETP Lett. 27, 276 (1978).

[69] Kip S. Thorne, Ronald W. P. Drever, Carlton M. Caves, Mark Zimmermann, and Vernon D. Sandberg, Quantum Nondemolition Measurements of Harmonic Oscillators, Phys. Rev. Lett. 40, 667 (1978).

[70] G. Vasilakis, V. Shah, and M. V. Romalis, Stroboscopic Backaction Evasion in a Dense Alkali-Metal Vapor, Phys. Rev. Lett. 106, 143601 (2011).

[71] Dmitry Budker and Michael Romalis, Optical magnetometry, Nat. Phys. 3, 227 (2007).

[72] I. K. Kominis, T. W. Kornack, J. C. Allred, and M. V. Romalis, A subfemtotesla multichannel atomic magnetometer, Nature 422, 596 (2003).

[73] D. Sheng, S. Li, N. Dural, and M. V. Romalis, Subfemtotesla Scalar Atomic Magnetometry Using Multipass Cells, Phys. Rev. Lett. 110, 160802 (2013).

[74] R. J. Sewell, M. Koschorreck, M. Napolitano, B. Dubost, N. Behbood, and M. W. Mitchell, Magnetic Sensitivity Beyond the Projection Noise Limit by Spin Squeezing, Phys. Rev. Lett. 109, 253605 (2012).

[75] L. Vaidman, Teleportation of quantum states, Phys. Rev. A 49, 1473 (1994).

[76] Dik Bouwmeester, Jian-Wei Pan, Klaus Mattle, Manfred Eibl, Harald Weinfurter, and Anton Zeilinger, SExperimental quantum teleportation, Nature 390, 575 (1997).

[77] A. Furusawa, J. L. Sorensen, S. L. Braunstein, C. A. Fuchs, H. J. Kimble, and E. S. Polzik, Unconditional quantum teleportation, Science 282, 706 (1998).

[78] M. Riebe, H. Häffner, C. F. Roos, W. Hänsel, J. Benhelm, G. P. T. Lancaster, T. W. Körber, C. Becher, F. Schmidt-Kaler, D. F. V. James, and R. Blatt, Deterministic quantum teleportation with atoms, Nature 429, 734 (2004).

[79] S. Olmschenk, D. N. Matsukevich, P. Maunz, D. Hayes, L.-M. Duan, C. Monroe, Quantum Teleportation Between Distant Matter Qubits, Science 323, 486 (2009)

[80] J. Yin, J. Ren, H. Lu, Y. Cao, H. Yong, Y. Wu, C. Liu, S. Liao, F. Zhou, Y. Jiang, X. Cai, P. Xu, G. Pan, J. Jia, Y. Huang, H. Yin, J. Wang, Y. Chen, C. Peng, and Jian-Wei Pan, Quantum teleportation and entanglement distribution over 100-kilometre free-space channels, Nature 488, 185 (2012).

[81] Noriyuki Lee, Hugo Benichi, Yuishi Takeno, Shuntaro Takeda, James Webb, Elanor Huntington, Akira Furusawa, Teleportation Nonclassical Wave Packets of Light, Science 332, 330 (2011).

[82] D. Gottesman, A. Kitaev, and J. Preskill, Encoding a qubit in an oscillator, Phys. Rev. A 64, 012310 (2001).

[83] Samuel L. Braunstein and H. J. Kimble, Teleportation of Continuous Quantum Variables, Phys. Rev. Lett. 80, 869 (1998).

[84] K. Hammerer, M. M. Wolf, E. S. Polzik, Quantum benchmark for storage and transmission of coherent states, Phys. Rev. Lett. 94, 150503 (2005).

[85] Christine A. Muschik, Klemens Hammerer, Eugene S. Polzik, and Ignacio J. Cirac, Quantum Teleportation of Dynamics and Effective Interactions between Remote Systems, Phys. Rev. Lett. 111, 020501 (2013).

[86] K. Hammerer, M. Aspelmeyer, E. S. Polzik, and P. Zoller, Establishing Einstein-Poldosky-Rosen Channels between Nanomechanics and Atomic Ensembles, Phys. Rev. Lett. 102, 020501 (2009).

[87] M. Hein, J. Eisert, and H. J. Briegel, Multiparty entanglement in graph states, Phys. Rev. A 69, 062311 (2008).

[88] H. J. Briegel and R. Raussendorf, Persistent Entanglement in Arrays of Interacting Particles, Phys. Rev. Lett. 86, 910 (2001).

[89] H. J. Briegel, D. E. Browne, W. Dür, R. Raussendorf, and M. Van den Nest, Measurement-based quantum computation, Nat. Phys. 51, 19 (2009).

[90] Jing Zhang, Local complementation rule for continuous-variable four-mode unweighted graph states, Phys. Rev. A 78, 034301 (2008).

[91] Chao-Yang Lu, et.al, Experimental entanglement of six photons in graph states, Nature Physics 3, 91 (2007).

[92] Aihong Tan, et.al, Experimental generation of genuine four-partite entangled states with total three-party correlation for continuous variables, Phys. Rev. A 78, 013828 (2008).

[93] Heng Shen, et.al, Quantum communication network utilizing quadripartite entangled states of optical field, Phys. Rev. A 80, 042320 (2009).

[94] Heng Shen, Kenan Qu, Weigang Zhang, and Jing Jin, Controlled-X gate with cache function for one-way quantum computation, Phys. Rev. A 85, 032317 (2012).

[95] Gradient coil design: A review of methods, MRI 11, 903 (1993).

[96] Lizann Bolinger, Manfred G Prammer, John S Leigh Jr, A multiple-frequency coil with a highly uniform B_1 field, JMR 81, 162 (1989).